ISSN 2394 - 9554

International Journal of Research in Science and Technology

Volume 6, Issue 1: Januray - March 2019

Indian Academicians and Researchers Association
www.iaraedu.com

International Journal of Research in Science and Technology

Volume 6, Issue 1 : January - March 2019

International Journal of Research in Science and Technology

Volume 6, Issue 1 : January - March 2019

CONTENTS

Research Papers

International Journal of Research in Science and Technology
Volume 6, Issue 1 : January - March, 2019
ISSN 2394 - 9954

CDS FILMS FOR OPTOELECTRONIC APPLICATIONS DEPOSITED BY SPRAY PYROLYSIS TECHNIQUE

Shivaji Munde[1], Devidas Halge[2], Jagdish Dadge[3], Megha Mahabole[4], Rajendra Khairnar[5] and Kashinath Bogle[6]
[1,2,4,5,6]Thin Film and Devices Laboratory, School of Physical Sciences, Swami Ramanand Teerth Marathwada University, Nanded
[3]Department of Physics, College of Engineering, Pune

ABSTRACT
This work demonstrates an easy method for synthesis of uniform nano-crystalline CdS films deposited on glass substrate by spray pyrolysis technique. In order to detect incident light, variation in current signals were measured. For photo-sensitivity, the current response of incident light was measured when exposed to different wavelengths ranging from 450 to 700 nm. The synthesized film showed significant detection of low-power (~13 mW/cm^2) light. The present study show that synthesized CdS film may be useful in fabricating a low-power, highly photosensitive, CdS based device for optoelectronic applications.

Keywords: CdS films, photo-sensitivity, low power operation.

INTRODUCTION
Looking at current scenario, there is a growing need for systems to be applied in observation and monitoring for scientific, commercial and military area [1]. For monitoring purpose most of these system needs to know light condition in that area and to know that photo-detectors are used. These photo-detectors are expected to work at low as well as high intensity regime of incident light. Traditional photo-detectors are the photoresistors/light dependent resistors (LDR) made of a high resistance semiconductor, as shown in Figure 1. In the dark, a photoresistor can have a resistance as high as several megohms (MΩ), while in the light, a photoresistor can have a resistance as low as a few hundred ohms. If incident light on a photoresistor exceeds a certain frequency, photons absorbed by the semiconductor give bound electrons enough energy to jump into the conduction band. The resulting free electrons (and their hole partners) conduct electricity, thereby lowering resistance. The resistance range and sensitivity of a photoresistor can substantially differ among dissimilar devices. Moreover, unique photoresistors may react substantially differently to photons within certain wavelength bands.

Commercial photoresistors of today are almost exclusively based on Si, Ge, CdS, CdSe, CdTe, PbS, PbSe, PbTe [3]. Of these materials, CdS photoresistors are very popular because of the high sensitivity response in the visible range matching well with the human eye. In this particular respect, CdS photoconductors come very close to an ideal photoconductor and find a variety of applications in fields including detection of visible light, buffer layers for solar cells, light emitting diodes (LEDs) and etc. [4-6]. The film thickness, grain size and morphology play a fundamental role in the performance of devices based on CdS films [7-8]. The band gap of CdS is in the range of visible light and the photosensitivity in the visible range is very high for CdS films [1,9]. A high photosensitivity is required for photo-detector applications. CdS films in thin or thick forms have been deposited using various methods including electrochemical deposition, spray pyrolysis, successive ionic layer adsorption and reaction, sputtering and chemical bath deposition [10]. Among these methods spray pyrolysis is a cost effective method and has deposited nanostructured thin/thick films due to its various benefits, such as simplicity, low temperature and coating of large area substrate without the need of vacuum atmosphere.

To the best of our knowledge, lot of attempts have been reported about the use of CdS thin films or nanostructures for photo-detectors. Yanli Pei, et al. achieved very narrow (~ 3 ms) rise and decay time in case of CdS nanowires mixed with Ag nanowires [11]. Husham et al. reported the photodetector properties of CdS thin films with the photosensivity (Iph/Id) in the range of 1.39–10.52 and have also synthesized CdS thin films by microwave assisted- CBD method with the photosensivity of 54 [1,12]. Whereas, use of thick film technology is of relatively recent origin in the field of photoconducting devices. Thick films of photoconducting CdS possess almost all the advantages of commercially viable sintered photoconductors namely superior photosensitivity, high mechanical strength, uniformity and relative ease of impurity incorporation. In addition, there are certain other advantages like amenability to large area fabrication and ease of mass production which are inherent in the technology itself.

In this work, we report synthesis of nano-crystalline CdS thick film on glass substrate using spray pyrolysis technique. Fast response time, fast decay time, and high photo sensitivity were demonstrated in thick CdS films.

ISSN 2394 - 9954

EXPERIMENTAL

Nano-crystalline CdS thick films were fabricated using spray pyrolysis method on glass substrate at 250 ^{0}C. For synthesis cadmium chloride ($CdCl_2$) and thiourea ($CS(NH_2)_2$) are used as a source of cadmium and sulfur respectively. The synthesis processes described as follows:

0.1 M of cadmium chloride (LOBA chemie, 99%) and 0.1 M thiourea (Merck specialities private limited, 99%) were dissolved in a mixture of methanol and water (3:1). The solution was stirred for 15 minutes to get a homogeneous solution.

Thick films were fabricated on a substrate (soda lime glass slides) having dimensions of 7.5 x 2.5 x 0.1 cm. The substrate was first washed with soap solution then kept in aqua regia solution for 12 hrs. These substrates were again washed with distilled water and finally cleaned with ethanol. Before spray pyrolyzing the above made solution on glass substrate, the substrate was kept on heating plate and temperature of the substrate was increased to 250 ^{0}C. The solution containing cadmium and sulphur source was filled in 100 ml perfume spray bottle and kept ready for spraying. The solution was spray manually on hot glass substrate from a distance of 15 cm. CdS films were synthesized for 200 spray. A yellow colour CdS film was obtained after cooling down the substrate to room temperature.

Above glass slide was cut into 1 x 1 cm piece and used for characterization as well as photo-detection measurement. The crystal structure of the thin films was determined by X-ray diffraction (XRD), using CuKα radiation in Rigaku Miniflex x-ray diffractometer. Morphology and particle size were determined by field emission scanning electron microscopy (FE-SEM) The chemical composition was performed by energy disperse spectrometer (EDS, BRUKER). Optical band gap was determined by the optical Spectrometer (Shimazu 1800). Metal–semiconductor–metal (MSM) photo-detectors were fabricated by Ag as electrodes. The photo response properties of CdS thick films were measured using current–voltage (I–V) curves at dark and illumination conditions, by a Keithley 6514 electrometer and Scientech 4078P power supply. The photo-response was measured at visible range and the photon intensity was 80 mW/cm^2.

RESULTS AND DISCUSSION

1. Structural analysis

X-ray diffraction (XRD) is a non-destructive technique, which reveals distinctive diffraction pattern “fingerprint” of crystalline materials and used for analysis of crystallographic structure, crystallite size and stress-strain of materials. The XRD spectra of CdS film deposited on glass substrate is shown in Figure 1.

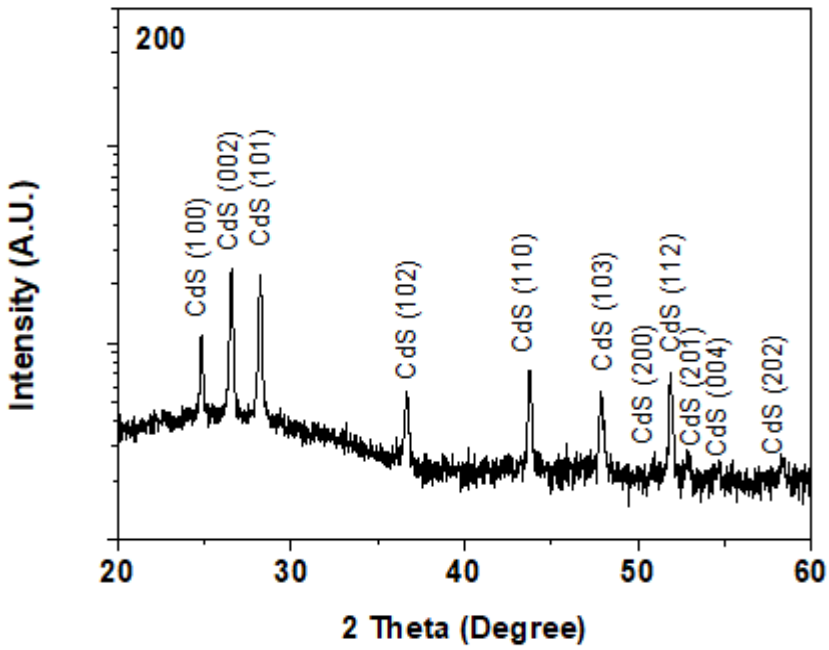

Figure-1: XRD patterns of 200 spray CdS film deposited on glass substrate via spray pyrolysis technique at 250 ^{0}C.

The XRD spectra for all films show existence of multiple reflection peaks for (100), (002), (101), (102), (110), (103), (200), (112), (201), (004) and (202) crystalline planes signifying pure hexagonal wurtzite CdS crystal structure with polycrystalline nature. These results match well with the JCPDS card no. 41-1049. The diffused background in XRD spectra may be due to amorphous glass substrate. We can see from the diffraction patterns that the peak intensity increases as the film thickness increases.

ISSN 2394 - 9954

The lattice parameters $a = 2*3^{1/2}d_{100}$ and $c = 2d_{002}$ were obtained from the positions of (100) and (002) peaks [13]. The estimated lattice constant is found to be lower compared with standard value, indicate increasing defect (vacancy) density along *a* and *c* crystal axis. The ratio of the lattice constants (*c/a*) is approximately 1.62, which is almost identical with the values reported for the powder samples [14], but less than the ideal value (1.633) of the close-packed hexagonal structures [14]. This indicates that the film deposited via spray pyrolysis is under tensile strain along the (002) plane. The *a* and *c* values of the strain-free samples are, respectively, 4.16 and 6.756 A^o [15]. In general the strain in material appears when there is a change in the stoichiometry or introduction of lattice imperfections/defects (vacancy or interstitial) in the material. The most probable defects in CdS are either sulfur vacancy or cadmium interstitial donor defects. The increase/decrease in strain indicates an increase/decrease in the concentration of lattice imperfections as the film thickness increases [13].

2. Morphological and compositional analysis

SEM displays the surface features and grain boundaries on CdS films. Figure 2 shows the SEM images of CdS film deposited on glass substrate at 250 ^{0}C. Irregular shaped grains with average size ~ 100 nm were observed with distinct grain boundaries (Figure 2(a)). EDS analysis was used for identifying the elemental composition of CdS film. Figure 2(b) illustrates the EDS spectrum containing prominent peaks for Cd and S with Cd/S ratio of ~ 1, which indicates good stoichiometry of CdS in the film. The evidence of Silicon in EDS (E = 1.8 keV) analysis is related to the detection of silicon in glass substrate.

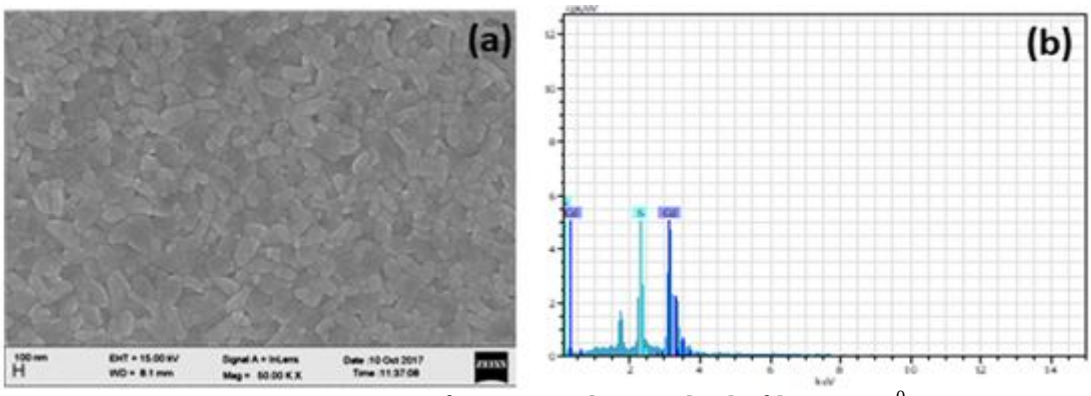

Figure-2: SEM image of 200 spray deposited CdS film at 250 ^{0}C.

This is explained based on the film growth mechanism in spray pyrolysis. At the initial stages of the film growth, droplets impact on the substrate surface, spread it into a disk shaped structure, which undergo thermal decomposition. Consequently, the film is composed of overlapping CdS disks of size > 100 nm, as seen in Figure 2(a) and Figure 3(a). For a constant rate of deposition, the deposition time is very short for thinner films when compared to the thicker films. As the deposition time increases, the small crystallites nucleate and grow on larger ones formed on a layer of smaller grains, as shown in Figure 3(b). During further increase in film thickness, a cloud of hot vapours formed between droplet and hot substrate, which evaporates the solvent in the droplet [16], which results in formation of small particles of CdS. These small particles get deposits on the surface of earlier CdS film. At higher film thickness, the time of deposition is large which allow coalescence of the small particles to form bigger grains in the film along with an improved crystallinity as observed from the XRD analysis. The average surface roughness of the films is observed to be 20 A^0 for the film deposited at 200 spray.

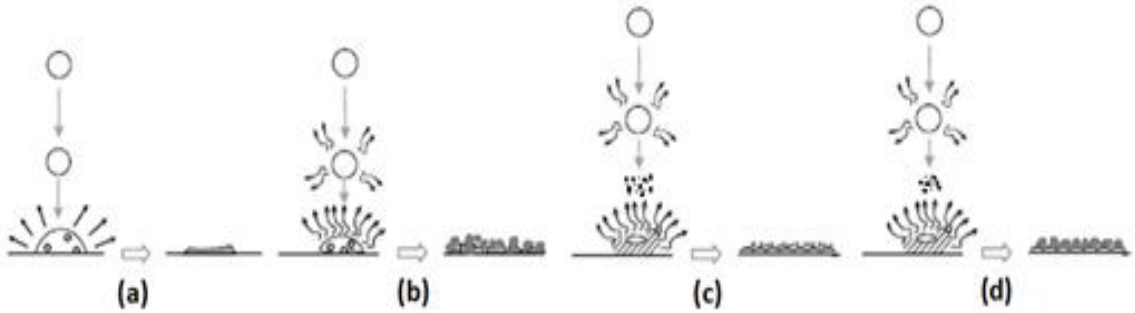

Figure-3: Schematic illustration of the film growth

3. Optical properties

UV–Vis spectroscopy was used to study optical properties of the CdS film. The film is found to be highly transparent in the visible region as seen in Figure 4.

ISSN 2394 - 9954

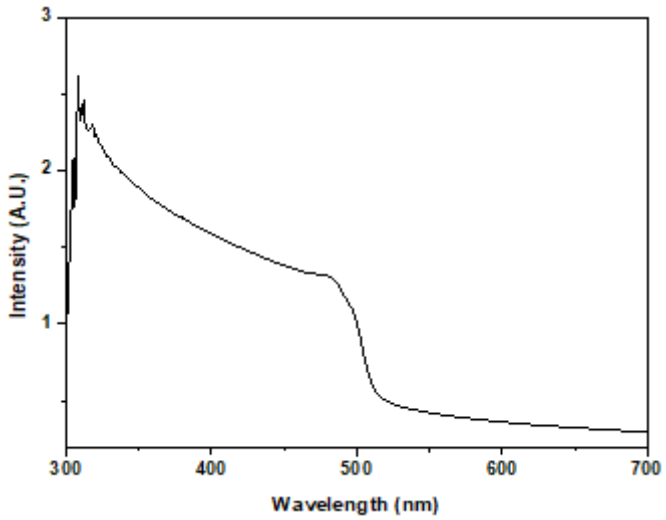

Figure-4: UV-Vis absorption spectra for CdS film

The absorption of light by the material is the property of that material and the absorbance at 520 nm is related to CdS material. Tauc equation was utilized for the determination of optical band gap as a function of film thickness. The optical band gap (Eg) value is ~ 2.4 eV.

4. Photo-detection measurement

To study the photo-detection property of nano-crystalline CdS film a setup is designed in laboratory consisting Keithley 6514 electrometer, Scientech 4078P power supply and 10 Watt LED (for red, green and blue light) source. Electrodes on the film were made using silver paste in "L" shape. Figure 5 illustrate the comparative I-V curves of the nano-crystalline CdS film measured under exposure of blue (450 nm), green (520 nm) and red (700 nm) light at an intensity of ~ 13 mW/cm^2. The photocurrent is found to be very low for red light, whereas, it increases to 8.6 and 24 µA for green and blue light (Figure 5). The photocurrent increases along with the decreasing wavelength of light. The estimated ratio of I_{on}/I_{off} is about 45 for blue light (450 nm, intensity of 13 mW/cm^2), 13 for green light (520 nm, intensity of 13 mW/cm^2) and 1.5 for red light (700 nm, intensity of 13 mW/cm^2), respectively.

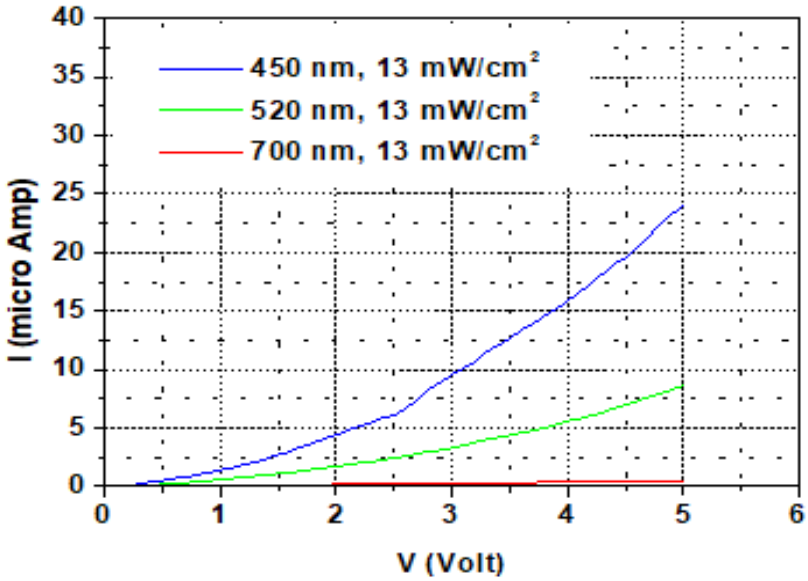

Figure-5: I-V curves for CdS films as a function of incident light wavelength 700 nm (red), 520 nm (green) and 450 nm (blue).

In CdS film, at higher (700 nm) wavelength lower photocurrent was observed, since the incident light has insufficient energy to excite electrons to the conduction band, which contributes to a lower photo current. Whereas, higher photo current was observed for green and blue light because of the energy imparted to the electron by the incident radiation is higher than the band gap [17]. Moreover, this attributes to the good quality nano-crystalline CdS thick films with lower density of trap states in the energy band gap between the fermi level and the conduction band edge. However, the presence of large percentage disorders in the film may leads to favour these films for development of high sensitivity of our photo-detector.

ISSN 2394 - 9954

CONCLUSION

In summary, nano-crystalline CdS films were deposited via spray pyrolysis technique at temperature 250 ^{0}C. The CdS thick film deposited on glass substrate show grain with lower residual strain indicating lower defect density in the film. The excellent photocurrent reproducibility and stability revealed that the synthesized nano-crystalline CdS thick film based photo-detector is a remarkable candidate for applications involving visible light detection. The present study introduced a simple and cost-effective technique for synthesize CdS films for a low-power, highly photosensitive, CdS based device for optoelectronic applications.

REFERENCES

1. N Hernandez-Como, S Moreno, I Mejia and M A Quevedo-Lopez, Semiconductor Science and Technology, 29 (2014) 085008
2. Akizukidenshi.com/download/ds/senba/GL55%20Series%20Photoresistor.pdf
3. D.P. Amalnerkar, Materials Chemistry and Physics 60 (1999) 1
4. M. Husham, Z. Hassan, M. Mahdi, A.M. Selman, N.M. Ahmed, Superlattices Microstruct., 67 (2014) 8
5. Y. Hashimoto, N. Kohara, T. Negami, N. Nishitani, T. Wada, Sol. Energy Mater. Sol. Cells 50 (1998) 71
6. J. Zhao, J.A. Bardecker, A.M. Munro, M.S. Liu, Y. Niu, I.-K. Ding, J. Luo, B. Chen, A.K.Y. Jen, D.S. Ginger, Nano Lett. 6 (2006) 463
7. J.S. Ma, C.Y. Yang, J.C. Sung, T. Minemoto, C.H. Lu, J. Mater. Sci.: Mater. Electron. 26 (2015) 6736
8. Z. Makhdoumi Kakhaki, A. Youzbashi, P. Sangpour, N. Naderi, A. Kazemzadeh, Micro Nano Lett. 11 (2016) 81
9. P.K. Nair, J. Campos, M.T.S. Nair, Semiconductor Science and Technology, 3(2) (1988) 134
10. Z. Makhdoumi-Kakhaki, A. Youzbashi, P. Sangpour, N. Naderi, A. Kazemzadeh, J Mater Sci: Mater Electron 28 (2017) 13727
11. Yanli Pei, Ruihan Pei, Xiaoci Liang, Yuhao Wang, Ling Liu, Haibiao Chen & Jun Liang, Nature Scientific Reports, Volume 6, id. 21551 (2016).
12. M. Husham, Z. Hassan, A.M. Selman, N.K. Allam, Sens. Actuators A Phys. 230 (2015) 9
13. J. P. Enrıquez, X. Mathew, Solar Energy Materials & Solar Cells 76 (2003) 313
14. A.E. Rakhshani, A.S. Al-Azab, J. Phys. Condens. Matter 12 (2000) 8745
15. S.M. Sze, Physics of Semiconductor Device, 2nd Edition, Wiley, New York, 1981, p. 848.
16. D. Perednis, L. J. Gauckler, Journal of Electroceramics, 14 (2005) 103–111
17. Y. Pei, R. Pei, X. Liang, Y. Wang, L. Liu, H. Chen, J. Liang, Scientific Reports, 2016, 6, 21551

International Journal of Research in Science and Technology
Volume 6, Issue 1 : January - March, 2019
ISSN 2394 - 9954

TOTAL IONIZATION CROSS SECTION OF INORGANIC ATOM (CA) BY ELECTRON IMPACT

Praveen Bhatt[1], Sushil Kumar[2] and Jai Shri Kumar[3]
Professor[1], Department of Applied Science and Humanities, Asia Pacific Institute of Information Technology, Panipat
Research Scholar[2], Department of Physics, Banasthali Vidyapith, Banasthali
Assistant Professor[3], Department of Physics, Govt. College Kharkhara, Rewari

ABSTRACT
We have made a study of the total ionization cross-sections of a inorganic atoms caused by electron impact for a single ionization. Total ionization cross-sections (TICS) have been calculated from threshold energy to 2100 eV. The theoretical technique, developed by Jain and Khare, has been used to calculate the TICS for organic compound.

Keywords: ionization, cross section

I. INTRODUCTION

Electron-molecule and electron-atom collisions either in the gas phase, on surfaces or in the condensed phase, kick off and compel almost all the relevant chemical processes associated with radiation chemistry, atmospheric chemistry, stability of nuclear waste repositories, plasma-enhanced chemical vapor deposition (CVD), plasma processing (Belic et al, 2010)[16] of materials for microelectronic devices and other applications, and in everyday illumination applications. Collisions of electrons with molecules and atoms generate the energetic species that drive chemical and physical changes of matter in environments that vary from plasmas to living tissue. The molecules used to scratch semiconductor materials do not respond with silicon surfaces unless they are subjected to electronic collisions in the low-temperature, high-density plasmas used in plasma etching and in CVD. A number of experimental and theoretical investiga¬tions of collision processes involving hydrogen molecules and molecular ions in electron impact have been and are still being performed widely because they are of the most essential significance in electron-molecule collisions. Indeed, understanding of electron-molecule collision pro¬cesses is indispensable in many applications such as chemistry, astrophysics, plasma chemistry (Fogle, 2010)[17] plasma fusion research,[1-5] and plasma material processing. Thus, there are a number of review articles on molecules and molecular ion collisions with electrons available presently. The cross sections for a variety of collision processes such as excitation, dissociation, ionization or photon emission have to be known with correct accuracies for such applications, modeling and diagnostics. Also diverse features, such as energy distributions and angular (spatial) distributions, of products, ions, atoms, molecules or photons, are key parameters necessary in understanding electron-molecule or electron-molecular-ion collisions and also in modeling of molecule-related phenomena such as plasma behavior. For example, the energy distributions of atomic hydrogen produced through dissociative processes are significant in deter-mining the mean free path for ionization in media such as plasmas. Ionization of atoms and molecules by electron impact is of primary importance in atmospheric science, plasma processes, and mass spectrometry.

Our objective is the calculations for differential cross sections as a function of secondary electron energy and angle at fixed impinging electron energy, corresponding to the formation of various cations in electron impact dissociative ionization of the atoms and atomic molecules, organic and inorganic compound have been carried out by employing a semi empirical formalism based on theoretical approach.

1.1 Electron Impact Ionization

Electron Impact is the original mass spectrometry ionization method and is still perhaps the most widely used of all ionization methods. In the Electron Ionization process, the sample of interest is vaporized into the mass spectrometer ion source, where it is impacted by the beam of electrons with sufficient energy to ionize the molecule.

The process may be summarized by the equation:

$$X(g) + e^- \rightarrow X^+(g) + 2e^-$$

The ion source is intended so that when the ions are formed they are pushed out of the source and into the mass analyzer.

The ion M^+ is known as the molecular ion. This species indicates the molecular weight, and thus provides very useful analytical information. The molecular ion will often undergo fragmentation in EI:

ISSN 2394 - 9954

$X_1^+ \rightarrow X_2^+ + X_n$

Where X_1 is the molecular ion.

X_2 is the fragment ion.

X_n is the neutral fragment.

The fragmentation process is dependent upon many qualities; including primary structure, electron energy and ion source temperature. In the top circumstances, fragmentation is advantageous, because one gathers structural information about the molecule under analysis in addition to the molecular weight information. However, in some cases, the entire molecular ions fragment and no molecular information is gathered.

Electron impact ionization is used in mass spectroscopy to ionize and fragment the sample molecules before mass analysis. The process is a relatively insensitive form of ionization producing a wide range of molecular fragments. The electron impact source consists of a heated filament that produces electrons which are accelerated to another electrode called the ion trap. Sample vapor diffuses into the electron beam and become ionized and fragmented the size depending on the electron energy which is controlled by the accelerating potential on the ion trap electrode. Low energy electrons produce molecular ions and larger fragments[7-9], whereas high energy electrons produce many smaller fragments and possibly no molecular ions. After the ions are formed, they are motivated by a potential applied to an ion-repeller electrode, away from the ion source into the accelerating section of the mass spectrometer, where mass analysis takes place.

Electron impact ionization is engaged to produce positive and negative ions in many areas of physics and chemistry. Applications range from analytical mass spectrometry, where electron bombardment is used in high and low pressure ion sources to produce positive and negative ions for partition and analysis by a mass spectrometer or mass filter, plasma studies, fusion modeling, radiation physics and gas discharges to more abstract applications such as astrophysical applications and modeling of planetary atmospheres. As the list of molecules that have been detected in interstellar space continues to grow, the significance of understanding the relations between these molecules and elemental charged particles, such as electrons, increases. Besides to these applications, concerns have freshly been raised about the potential damage that low energy electrons can cause on DNA. (Mark Bart, 2003). This has provoked several groups to investigate electron impact ionization of biological molecules: uracil, thymine and cytosine, using low energy electrons, thus opening up new research areas of electron impact in biophysics

According to the widely subscribed mechanism of the gas-phase breakdown, the primary electrons are created in the gas phase by the impact of naturally occurring ionizing-radiation, such as cosmic rays, and cause the subsequent ionization and bombardment of ions on the cathode surface, which causes the emission of the secondary electrons and ionization of gas. This mechanism is based on Townsend's theory with the assumption of the gas-phase ionization, which we do not agree to consider as a fact.

The recent discovery of the cathode glow in the deposition plasma of organic vapour, which showed that the dissociation of molecules occurs prior to the ionization, defies the above-mentioned classical mechanism.

II. THEORETICAL METHODOLOGY

Even on the theoretical side several more methods are available to compute the cross sections over a wide range of atoms and molecules. For example, there is no explanation for dissociate, total, single and double ionization cross section. This formula is also applicable to calculate partial, photo, integral ionization cross sections of atoms and molecules.

The formula is useful for finding the rate coefficient of any atoms and molecules. Semi-empirical formalism developed by Jain and Khare [10-13]. This formula is also applicable to calculate partial, photo, integral ionization cross sections of atoms and molecules. The formula is useful for finding the rate coefficient of any atoms and molecules. This is a theoretical approach. In brief, the single differential cross sections in the complete solid angle ($\Omega = 4\Pi = \int 2\pi \sin\theta d\theta$) as a function of secondary electron energy ε corresponding to the production of i^{th} type of ion in the ionization of a molecule by incident electron of energy E is given by equation 1:

$$Q_i(E,W,\theta) = \frac{a_0^2 R^2}{E}\left[\int_{k\to 0}^{E-I_i}\left\{\begin{array}{l}\dfrac{E-W}{E-I_i}\dfrac{1}{W}df_i(W,K,\theta)\times\ln\left[1+C_i(E-I_i)\right]+\\ \dfrac{E-I_i}{E\left(\varepsilon_0^3+\varepsilon^3\right)}\times S_i\left(\varepsilon-\dfrac{\varepsilon^2}{E-\varepsilon}+\dfrac{\varepsilon^2}{(E-\varepsilon)^2}\right)\end{array}\right\}\right]2\pi\sin\theta d\theta \quad .....(1)$$

ISSN 2394 - 9954

Where, $W (=\varepsilon + I_i)$ is defined as energy loss suffered by the incident electron.

Ii = the ionization threshold for the production of i^{th} type of ion,

a_0 = the Bohr radius,

ε_0 = energy parameter,

C_i = collision parameter,

S_i = number of ionizable electrons,

R = Rydberg constant and

θ = the scattering angle respectively.

In the present formulation, the dipole oscillator strengths df_i/dw are the key parameters. The oscillator strength is directly proportional to the photo ionization cross section [10-15]. Summation of PDDCS (Partial double differential cross section) over the system gives the total (DDCS) (Double differential cross section)

$$Q_i^t(E,W,\theta) = \sum_i Q_i(E,W,\theta).$$

Here it is interesting to note that $Q_i(E,W,\theta)$ is isotropic and hence the material property of molecule, i.e., the oscillator strength must be isotropic in nature. Here $df_i(W,K,\theta),$ the differential generalized oscillator strength (DGOS) in the optical limit $(K \to 0)$ has been used. From Lassettre's Theorem [8-9] the DGOS in the Bethe regime is reduced to the cosine distribution form of the linear optical oscillator strengths $df_i(W,0))/dW,$ i.e.

$$df_i(W,K,\theta) \to (1/4\pi)[1+\beta P_2(\cos\theta)] \times df_i(W,0)/dW,$$

Where β is the asymmetric parameter and $P_2(\cos\theta) = \frac{1}{2}(3\cos^2\theta - 1)$ is the second order Legendre polynomial. In the present treatment, β is chosen as the probability of ionizing electrons in the ionization processes however, it depends on the ejected electron energy. The oscillator strengths are directly proportional to the photo ionization cross sections.

Further integration of Equation (1) with respect to the scattering angle θ (from 0 to 2π) gives the PSDCS (Partial single differential cross section)

$$Q_i(E,W) = \int Q_i(E,W,\theta)d\Omega,$$

where differential solid angle dΩ is $2\pi\sin\theta d\theta$

Similarly, SDCS (Single differential cross section) are given as

$$Q_i^T(E,W) = \sum_i Q_i(E,W).$$

Further integration of PSDCS with respect to W from I to W_{max} (= .E) results in PICS (Partial integral cross section), i.e.

$$Q_i(E) = \int Q_i(E,W)dW .$$

The present formulation requires the major input data of the Photo ionization cross-sections in terms of the optical oscillator strengths.

III. RESULTS AND DISCUSSION

In this paper the results of the absolute partial ionization cross section measurements for the inorganic atoms are calculated from threshold to 2100 eV by the use of modified Jain-Khare approach. Table 1

The Total ionization cross sections along with the total ionization cross section are also summarized in Table 1.

Table-1

Total ionization cross-section values for organic compound.

Electron Energy (eV)	Total ionization-cross section of Ca (10^{-21} cm^2) Fragmented ions

ISSN 2394 - 9954

Energy (eV)	TIC	Energy (eV)	TIC
11	1.12966	200	4.361069
20	3.60562	300	4.035917
30	4.476	350	3.88031
40	4.72468	400	3.72569
60	4.839064	450	3.574782
80	4.823761	500	3.430103
100	4.809639	650	3.04367
150	4.567427	700	2.931065
Energy (eV)	TIC		
1000	2.395485		
1100	2.258477		
1200	2.136894		
1300	2.028353		
1400	1.930922		
1500	1.842899		
1700	1.690331		
1900	1.562421		
2000	1.505867		

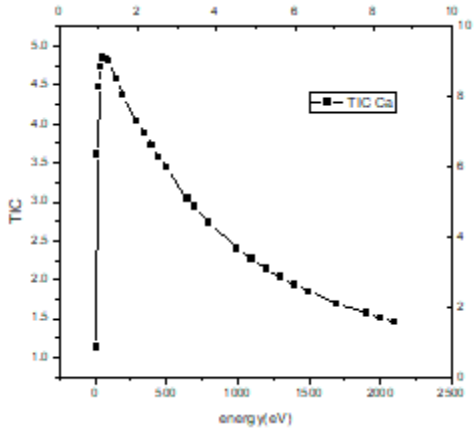

IV. CONCLUSION

The accuracy of the present formula is linked with the accuracy of oscillator strength. Theoretically, the accuracy of the present calculation can be increased if we have the more accurate experimental data for the photo-ionization cross-section for the production of various ions.

REFERENCES

1. A.W.Luft, Appl. Phys.Commun.8 (1988) 1.
2. D.A Gougherty and A.Gallagher, J.Appl .Phys. 67 (1990)139.
3. A.M.Wrobel, J. Macromol. Sci.Chem. A. 201. (1983) 583.
4. I.Tajama and M.Yamamoto, J.Polym. Sci:Part A Polym. Chem. 25(1987)1737.
5. P.Favia, Plasma Sources Sci. Technol., 1(1992)59.
6. R. Basner, R.foest, M.Schmidt, F. Sigeneger,P.Kurunczi,K.Becker,H.Deutsch, Int. J.Mass Spectrometry and Ion Processes 153(1996)65-78.
7. S.McGinnis,Chem.Phys.Lett.232(1996)99.
8. T.W. Shyn, W.E. Sharp, Phys. Rev. A 20(1979) 2332.
9. E N Lassettre, A Skerbele and A D Michael, J.Chem. Phys. (1967) 46, 4536.
10. S.P. Khare, Planet. Space Sci. 17 (1969) 1257.
11. S.P. Khare, W.J. Meath, J. Phys. B 20 (1987) 2101.
12. P. Bhatt, S.Pal, J. Electron Spectro. Related Phenomenon 129(2003)35-41.

ISSN 2394 - 9954

13. P. Bhatt, S.Pal, J. of Mass Spectrometry 229(3)(2003)151-156.
14. Satyendra Pal, J. Phys.: Conf. Ser. (2009)163,012030.
15. Satyendra Pal, J.Phys. Scr. (2011) 19.
16. Belic D S, Lecointre J, Defrance P (2010). J.Phys. B: At.Mol.Opt.Phys 43 ,18.
17. Mark Bart (2003 Ph.D thesis of University of Canterbury,Christchurch,New Zealand.

International Journal of Research in Science and Technology
Volume 6, Issue 1 : January - March, 2019
ISSN 2394 - 9954

SCATTERING CROSS SECTION OF INORGANIC ATOM BY ELECTRON IMPACT ETCHING

Praveen Bhatt[1], Priyanka Duhan[2] and Jaswant Singh[3]
Professor[1] and Assistant Professor[2], Department of Applied Science and Humanities, Asia Pacific Institute of Information Technology, Panipat
Research Scholar[3], Department of Physics, Banasthali Vidyapith, Banasthali

ABSTRACT
Total ionization cross-sections of an inorganic atom scandium caused by electron impact for a single ionization. Total ionization cross-sections (TICS) have been calculated from threshold ionization energy to 2150 eV. The modified model, developed by Jain and Khare, has been used to calculate the TICS for inorganic compound (scandium).

Keywords: ionization, cross section

I. INTRODUCTION

An accurate hypothetical treatment of the low energy electron impact ionization problem is unfeasible at present due to the complexity of representing the asymptotic form of the wavefunction when two slow electrons are in the continuum. It is however possible to think about ionization by a very fast incident electron (k20 > 1), in which the ejected electron has a low energy. It is now possible, however to use the Born approximation (or Coulomb-Born approximation) with a well correlated multi configuration initial states wavefunction and R-matrix final state wavefunction. A detailed theoretical description of this has been offered by Robb et al (1975) [1].

Even though the physical processes of interest in astrophysics and plasma chemistry/physics involve mainly low energy incident electrons (k20 = 1), exact Born calculations can be helpful in two respects. First, they can be used to normalize experimental data and second, they can offer estimates for many applications where, at the moment, no other reasonable estimates exist.

Protons in the beam may be scattered from the edges of collimator apertures and also from collisions with the target gas. If the scattered protons hit metal surfaces such as the grid or the beam suppressor, secondary elec¬trons are formed[1-5]. It is hard to estimate the scatter¬ing from the collimator, but it can be minimized. This is accomplished by making the edges of the aperture as sharp as possible, thus limiting the area from which scattering into the measuring region can take place, and by having a shield past the collimator just large enough to permit the main beam pass but little enough to prevent most scattered particles. The scattering from target only for extremely low proton energies and for heavy targets, and even then, excluding for unusual geometries, must not generate many secondary electrons[6-9].

Our objective is the calculations for differential cross sections as a function of secondary electron energy and angle at fixed impinging electron energy, corresponding to the formation of various cations in electron impact dissociative ionization of the atoms and atomic molecules, organic and inorganic compound have been carried out by employing a semi empirical formalism based on theoretical approach.

Electron Impact Ionization

The main atomic processes that give rise to the line spectra of astronomical objects are of two sorts, radiative or collisionnal. In the first type the atom or ion interacts with a photon while the second type involves collisions between an atom (ion) and an electron. The most important processes are:

Photo-excitation and radiative decay:

$X_i + h\nu \rightleftharpoons X_f$

Photo-ionization:

$X_i + h\nu \rightarrow A_f + e^-$

Recombination:

$X_i + e^- \rightarrow X_f + h\nu$

Electron impact excitation:

$X_i + e^- \rightleftharpoons X_f(N) + e^-$

ISSN 2394 - 9954

Where X corresponds to the target ion, X indicates that the ion has $+1$ electrons.

The subscripts i and f are for initial and final states.

In order to explain such processes and derive atomic data of use for applications, we have to signify a system made of a nucleus of nuclear charge Z and 'many' electrons. The full description can be achieved by solving the time independent Schrodinger equation,

$$H\Psi = E\Psi$$

Where H is the Hamiltonian, Ψ is the eigenfunction linked to the eigen energy E.

Here the atomic unit system in which e = m = ħ = 1.

In order to be complete the Hamiltonian should account for all the interactions among the different particles present in the system. This includes the kinetic energy of the electrons, their potential energy generated by the nucleus, the repulsive interaction between electrons, the spin-orbit for each electron, the spin-spin, spin-other orbit and orbit-orbit interactions between electrons. In the case of a light element of low charge, we can use the non-relativistic Hamiltonian.

II. THEORETICAL METHODOLOGY

Even on the theoretical side several more methods are available to compute the cross sections over a wide range of atoms and molecules. For example, there is no explanation for Irect dissociate, total, single and double ionization cross section. This formula is also applicable to calculate partial, photo, integral ionization cross sections of atoms and molecules.

The formula is useful for finding the rate coefficient of any atoms and molecules.semi-empirical formalism developed by Jain and Khare [10-13].This formula is also applicable to calculate partial, photo, integral ionization cross sections of atoms and molecules. The formula is useful for finding the rate coefficient of any atoms and molecules. This is a theoretical approach.In brief, the single differential cross sections in the complete solid angle ($\Omega = 4\Pi = \int 2\pi \sin\theta d\theta$) as a function of secondary electron energy ε corresponding to the production of ith type of ion in the ionization of a molecule by incident electron of energy E is given by equation 1:

$$Q_i(E,W,\theta) = \frac{a_0^2 R^2}{E}\left[\int_{k\to 0}^{E-I_i}\left\{\begin{array}{l}\frac{E-W}{E-I_i}\frac{1}{W}df_i(W,K,\theta)\times\ln\left[1+C_i(E-I_i)\right]+\\ \frac{E-I_i}{E\left(\varepsilon_0^3+\varepsilon^3\right)}\times S_i\left(\varepsilon-\frac{\varepsilon^2}{E-\varepsilon}+\frac{\varepsilon^2}{(E-\varepsilon)^2}\right)\end{array}\right\}\right] 2\pi\sin\theta d\theta \quad .....(1)$$

Where, $W\ (=\varepsilon + I_i)$ is defined as energy loss suffered by the incident electron.

I_i = the ionization threshold for the production of i^{th} type of ion,

a_0 = the Bohr radius,

ε_0 = energy parameter,

C_i = collision parameter,

S_i = number of ionizable electrons,

R = Rydberg constant and

θ = the scattering angle respectively.

In the present formulation, the dipole oscillator strengths df_i/dw are the key parameters. The oscillator strength is directly proportional to the photo ionization cross section [10-15]. Summation of PDDCS (Partial double differential cross section) over the system gives the total (DDCS) (Double differential cross section)

$$Q_i^t(E,W,\theta) = \sum_i Q_i(E,W,\theta).$$

Here it is interesting to note that $Q_i(E,W,\theta)$ is isotropic and hence the material property of molecule, i.e., the oscillator strength must be isotropic in nature. Here $df_i(W,K,\theta)$, the differential generalized oscillator strength (DGOS) in the optical limit $(K\to 0)$ has been used. From Lassettre's Theorem [8-9] the DGOS in the Bethe regime is reduced to the cosine distribution form of the linear optical oscillator strengths $df_i(W,0))/dW$, i.e.

ISSN 2394 - 9954

$df_i(W,K,\theta) \rightarrow (1/4\pi)[1+\beta P_2(\cos\theta)] \times df_i(W,0)/dW,$

Where β is the asymmetric parameter and $P_2(\cos\theta) = \frac{1}{2}(3\cos^2\theta - 1)$ is the second order Legendre polynomial. In the present treatment, β is chosen as the probability of ionizing electrons in the ionization processes however, it depends on the ejected electron energy. The oscillator strengths are directly proportional to the photo ionization cross sections.

Further integration of Equation (1) with respect to the scattering angle θ (from 0 to 2π) gives the PSDCS (Partial single differential cross section)

$Q_i(E,W) = \int Q_i(E,W,\theta)d\Omega,$

Where differential solid angle dΩ is $2\pi\sin\theta d\theta$

Similarly, SDCS (Single differential cross section) are given as

$Q_i^T(E,W) = \sum_i Q_i(E,W)$.

Further integration of PSDCS with respect to W from I to W_{max} (= E) results in PICS (Partial integral cross section), i.e.

$Q_i(E) = \int Q_i(E,W)dW$.

The present formulation requires the major input data of the photo ionization cross-sections in terms of the optical oscillator strengths.

III. RESULTS AND DISCUSSION

In this paper the results of the absolute partial ionization cross section measurements for the organic compound are calculated from threshold to 350 eV by the use of modified Jain-Khare approach. Table 1

The Total ionization cross sections along with the total ionization cross section are also summarized in Table 1.

Table-1

Total ionization cross-section values for inorganic atom Scandium.

Electron Energy (eV) Total ionization-cross section (10^{-19} cm^2) Fragmented ions of scandium

Energy (eV)	TIC
11	0.945833
20	3.359094
30	4.708091
40	5.250914
50	5.498426
60	5.731677
70	5.756662
80	5.713267
90	5.63688
Energy (eV)	TIC
100	5.644043
150	5.302907
200	4.943341
300	4.383427
400	3.938518

ISSN 2394 - 9954

500	3.566515
600	3.254682
700	2.992361
800	2.769815
1000	2.414292
1100	2.270404
1200	2.143688
1300	2.031238
1400	1.930669
1500	1.840348
1700	1.684551
1800	1.616773
1900	1.554641
2000	1.497408
2100	1.444664
2150	1.419794

Figure no.-01

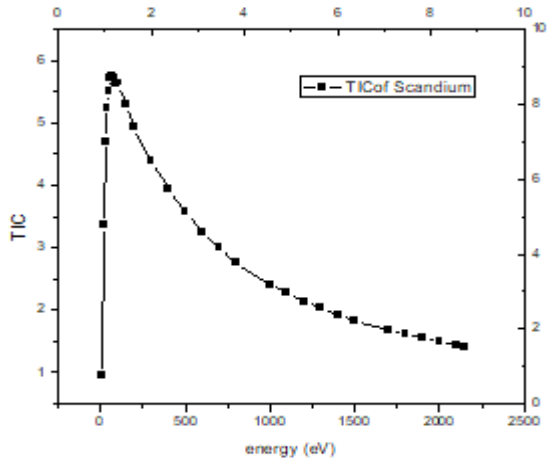

REFERENCES

1. Robb W D, Rountree S P and Burnett T (1975). Phys. Rev. A 11(4)1193-1199.
2. Rudd M E, Toburen L H and Stolterfoht N (1979) At. Data Nuc. Data Tables, 23(5) 405-442.
3. Schwarz H (1991) Chem. Unserer Zeit, 25, 268-278.
4. Stolterfoht N (1971) Helium." Z. Physik 248, 81 (1971).
5. P.Favia, Plasma Sources Sci. Technol., 1(1992)59.
6. Vinodkumar M, Limbachiya C, Korot K and Joshipura K N (2008) Eur. Phys. J. D, 48, 333–342.
7. Younger S M and Mark T D (1985)."Electron impact ionization."ed. TD Mark and GH Dunn (Berlin: Springer) Ch.2.
8. T.W. Shyn, W.E. Sharp, Phys. Rev. A 20(1979) 2332.
9. E N Lassettre, A Skerbele and A D Michael, J. Chem. Phys. (1967) 46, 4536.
10. S.P. Khare, Planet. Space Sci. 17 (1969) 1257.
11. S.P. Khare, W.J. Meath, J. Phys. B 20 (1987) 2101.
12. P. Bhatt, S.Pal, J. Electron Spectro. Related Phenomenon 129(2003)35-41.
13. P. Bhatt, S.Pal, J. of Mass Spectrometry 229 (3)(2003)151-156.
14. Satyendra Pal, J. Phys.: Conf. Ser. (2009)163, 012030.
15. Satyendra Pal, J.Phys. Scr. (2011) 19.

International Journal of Research in Science and Technology
Volume 6, Issue 1 : January - March, 2019
ISSN 2394 - 9954

INVESTIGATION OF MASS ATTENUATION COEFFICIENT AND TOTAL ATOMIC CROSS SECTION OF GeO2 IN THE ENERGY RANGE 122-1330KeV

Pradip S. Dahinde[1], R. R. Bhosale[2], Pravina P. Pawar[3]
Research Student[1,2] and Professor[3], Department of Physics, Dr. Babasaheb Ambedkar Marathwada University, Aurangabad

ABSTRACT
In the present investigation, we have determined here the mass attenuation coefficients (μ_m) of germanium oxide for 122 -1330 keV. Photons are measured using the radioactive sources Co^{57}, Ba^{133}, Cs^{137}, Na^{22}, Mn^{54} and Co^{60}. In the current work to detect gamma rays NaI(Tl) scintillation detection system was used. The investigated attenuation coefficient values were then used to determine the important parameters i.e. total atomic cross sections (σ_t) for germanium oxide. Graphically it is observed that the variations of μ_m, σ_t with energy The values of μ_m, σ_t, are higher at lower energies and they decrease sharply as energy increases. The XCOM data is used to calculate Theoretical values. We were observed that the Theoretical and experimental values are found to be in a good agreement (error < 3-4%).

Keywords: attenuation coefficient; total atomic cross sections

INTRODUCTION
The mass attenuation coefficient values of partial photon interaction processes such as photoelectric effect, Compton scattering, pair production and all these are available in the form of software package XCOM from Berger and Hubbell (1987) by substituting the chemical composition of compound or mixture the mass attenuation coefficient of the In recent years the study of photon atom interaction with different materials has becomes more importance because of extensive use of radioactive sources in different field like industrial, chemical and other field. The proper characterization is must require for scientific study of different interaction of radiation with matter and also the penetration ability and diffusion of gamma radiation in external medium is required. The nature of the material is also important factor because from many studies it is observed that the Mass attenuation coefficient (μ_m) usually depends upon the energy of radiations and nature of the target material.

The Oxide covers a wide range of applications almost in every field. The study on the interaction of gamma rays with oxide materials are of great interest from theoretical and experimental point of view. It is found that the values of mass attenuation coefficients, total atomic cross section of metal oxides in the energy range of 122-1330 keV are studied. These studied values are compared with theoretical values calculated using XCOM program (Berger M.J. and Hubbell J.H., 1987,1999).are found to be good match between each other. Mass attenuation coefficient (μ_m) is a most important and measure factor of the average number of interactions between incident photons and substance that occur in a given mass per unit area thickness of the material under investigation (Hubbell, 1999). Because of their diverse applications in industrial, chemical, biological, medical, shielding, agricultural applications also in food technology, biosensor, photovoltaic cell and solar cells ultra sound are more recent applications. The useful parameters, like total atomic are critical parameters in applied field as well as fundamental science is obtained by using mass attenuation coefficient. The Shielding materials will be generated in the different energy range. Hubble (1982) are published tables of mass attenuation coefficients and the mass energy absorption coefficients for 40 elements and 45 mixtures and compounds for 1 keV to 20 MeV . Hubbell and Seltzer (1995) replaced these tables in form of tabulation for all elements having $1 \leq Z \leq 92$ and for 48 additional substances for dissymmetric interest. XCOM program converted to windows version is now called as Win XCOM Gerward et al.(2001,2004).

Oxides and biological material plays an important role. The knowledge of Interaction of photons with different substances (i.e. alloy, plastic, soil, role in radiation biology, nuclear technology, and space research as radioactive sources such as Co^{57} (122 keV), Ba^{133} (356 keV), Na^{22} (511 and 1275 keV), Cs^{137} (662 keV), Mn^{54} (840 keV) and Co^{60} (1170 and 1330 keV) are more significant in biological studies, radiation sterilization, industry (Hall, 1978). Photons in the high energy range are vital for radiography and medical imaging, the giga-electron-volt energy range are important in astrophysics and cosmology (Manohara et al. 2008).There have been several experimental and theoretical investigations for the determination of mass attenuation coefficient (μ_m) of different materials can be used to determine other related parameters like, total atomic cross (σ_t) (El-Kateb and Abdual-Hamid, 1991; Gowda et al., 2005; Manjunathaguru and Umesh, 2006; Pawar P.P. and Bichile sections (σ_t), molar extinction coefficients (ε), electronic cross sections (σ_e), effective atomic numbers G.K., 2013; Sandhu et al., 2002).

ISSN 2394 - 9954

Many researcher are interested and attracted towards the study of mass attenuation and different values of complex molecules in the energy range 5-1500 keV as the photons in this energy range are widely used in medical and biological applications (Hubbell, 1999) via different methods (Murut Kurudirek, 2013, 2014a, 2014b, 2014c, 2015; Midgley, 2004, 2005; Manohara and Hanagodimath, 2007; Demir et al., 2012; Murat Kurudirek and Tayfur Onaran, 2015; Danial Salehi et al., 2015).

2. CALCULATION METHODS

2.1 Mass attenuation coefficient

The inverse exponential power law that in the present work we study some theoretical parameters of some oxide that have been used to determine the mass attenuation coefficient μ_m. And other related parameters which are based on it. A parallel beam of the measured intensity I of the transmitted mono-energetic X-ray or γ-photons passing through matter is related to the incident intensity I_0 is is usually referred to as Beer-Lambert law is given by the relation.

$$I = I_0 e^{-\mu_m X} \tag{1}$$

Where, I_0 and I are incident and transmitted photon intensities respectively,

X is mass per unit area (g/cm^2), μ_m is mass attenuation coefficient (cm^2/g) given by the following equation for a compound or mixture of elements (Jackson D. F. and Hawkes D.J., 1981; Hubbell and Seltzer, 1995). By using the Eq. (1) we obtain the following equations for linear attenuation coefficient;

$$\mu = 1/t \ln (Io/I) \tag{2}$$

The mass attenuation coefficient of the sample is measured by using the following equation:

$$(\mu / \rho)_i = \sum_i W_i (\mu / \rho)_i \tag{3}$$

Where W_i is the weight fraction and $(\mu/\rho)_i$ is the mass attenuation coefficient of the i^{th} constituent element. Weight fraction is given by

$$W_i = n_i A_i / \sum_j n_i A_j \tag{4}$$

Where A_j is the atomic weight of i^{th} element and n_i is the number of formula units.

2.2 Total atomic cross section

Total attenuation cross section (σ_t) is a fundamental parameter to describe the photon interaction with matter. The value of mass attenuation coefficient (μ_m) is used to determine Total atomic cross section (σ_t) by using the following relation (Hubbell, 2006; Erzeneoğlu et al.,2006).

$$\sigma_t = \frac{A}{N_A X} \ln(I_o / I) \tag{5}$$

Where, A is molecular weight and N_A is Avogadro's number ($6.02486 \times 10^{\wedge 23}$).

3. EXPERIMENTAL DETAILS

In the presented studies we measured incident and transmitted photon energies by using a narrow-beam good geometry set up. Fig. 1 shows the schematic view of experimental set up. The six radioactive sources, Co^{57} (122 keV), Ba^{133} (356 keV), Na^{22} (511 and 1275 keV), Cs^{137} (662 keV), Mn^{54} (840 keV) and Co^{60} (1170 and 1330 keV) used in this investigation were obtained from Bhabha Atomic Research Centre, Mumbai, India. Gamma rays emitted by these radioactive sources were collimated and detected by a NaI(Tl) scintillation detector. The Signals from the detector (2"×2") NaI (Tl) crystal having energy resolution of 8.2% at 0.662 MeV gamma rays from the decay of Cs^{137} after suitable amplification were recorded in an EG&G ORTEC 13-bit plug-in-card coupled with a PC/AT. Stability and reproducibility of the arrangement were checked before and after each set of runs. In order to minimize the effects of small-angle scattering and multiple scattering events on the measured intensity, the transmitted intensity was measured by setting the channels at the full-width half-maximum position of the photo-peak.

Pellet shaped uniform thickness of chosen oxides such as Germanium oxide (GeO2) under investigation were confined in a cylindrical plastic container with diameter similar to that of the sample pellet. The diameters of the sample pellets were determined using a traveling microscope. The attenuation of photons in the empty

ISSN 2394 - 9954

containers was negligible. Each sample pellet was weighted in a sensitive digital balance with an accuracy of 0.001 mg several times to obtain the average value of the mass. The mass per unit area was determined in each case using the diameter of the pellet and mean value of the mass of the pellet. The sample thickness was selected in order to satisfy the following ideal condition as far as possible (Creagh D.C., 1987):

$$2 \leq \ln(\frac{I_o}{I}) \leq 4.$$

The Mass attenuation coefficients (μ/ρ) of Germanium oxides were determined from the measured values of incident photon intensity I_0 (without sample) and transmitted photon intensity I (with sample) Eq. (2). The experiments were conducted in an air-conditioned room to avoid possible shifts of the photo-peaks. Room temperature of 24 ± 1°C was maintained throughout the experimental period. Other sources of error, excluding multiple scattering and counting statistics, are small-angle scattering, sample impurity, nonuniformity of the sample, photo built-up effects, dead time of the counting instrument, and pulse pile effect which were evaluated and reduced.

The maximum angle of scattering was maintained <30 min by properly adjusting the distance between the detector and source (30cm $\leq$ d $\leq$ 50 cm), as the contribution of coherent and incoherent scattering at such angles in the measured cross sections at intermediate energies is negligible (Hubbell, 1999). Hence, no small-angle scattering corrections were applied to the measured data. All the oxides samples used in this study were of high quality sigma Aldrich and of high purity (99.9 %) without high-Z impurities. Hence, sample impurity corrections were not applied to the measured data.

In the presented investigation, uncertainty in the mass per unit area and the error due to nonuniformity of the sample are <0.05% for all energies of interest. Optimum values of count rate and counting time were chosen to reduce the effects of photon built-up and pulse piles. The photon built-up effect, which is a consequence of the multiple scattering inside the sample, depends on the atomic number and sample thickness, as well as the incident photon energy. A built-in provision for dead time correction was present in the MCA used during this investigation.

4. RESULTS AND DISCUSSION

In the current work, the values of the variation between experimental and theoretical values of μ_m (cm^2/g) for germanium oxide (GeO_2) studied at 122, 360, 511, 662, 840, 1170, 1275- and 1330-keV photon energies are shown in Table 1, and those for all oxide samples are plotted in Figure 2. It can be observed from the figure and table that μ_m decreases with increasing photon energy. It is observed that he experimental values of μ_m agree with the theoretical values calculated using the XCOM program.

The total uncertainties in experimental values of the μ_m depend on the uncertainties of I_0 (without attenuation), I (after attenuation) measurements of mass thickness values, and counting statistics. The estimated total uncertainty in the measured experimental values of μ_m was found to be in the range of 2-3%. The another important parameter, the measured total atomic cross section (σ_t) of GeO2.oxides are studied and displayed in Tables 2 the typical plots show the variation of σ_t versus E shown in Figure. It is observed that the behavior of σ_t with photon energies is almost similar to that of μ_m.

5. CONCLUSION

The present experimental study was carried out to obtain information on mass attenuation coefficient, μ_m and related parameters σ_t for Germanium oxide samples. It has been found that μ_m is an extremely useful and sensitive physical quantity for the determination of these parameters for the chosen oxide samples. The total atomic cross sections of GeO_2 with low and medium-Z elements are determined in the chosen energy range (122-1330 keV) which is emitted by the radioisotopes ^{60}Co, $^{57}C_o$, ^{133}Ba, ^{54}Mn, ^{22}Na, and ^{137}Cs. For the interaction of photons with matter the values of that μ_m depend on the physical and chemical environments of the samples. These values were found to decrease with increasing photon energies. From the study it is observed that the parameters σ_t changed similar to that of μ_m and it is clear that ε depends totally on the number and nature of atoms. In the present work, it has been observed that the data on mass attenuation coefficient (μ_m) and other parameters are very useful in industrial, biological, medical, shielding and other technological applications, solar cell and recently in sensors field. The measured data were compared against Win-XCOM-based data the agreement within 4%.

ISSN 2394 - 9954

6. ACKNOWLEDGMENT
The authors thank Prof. G. K. Bichile for his discussion on this study. And Dept. of physics,Dr. Babasaheb Ambedkar marathvada university ,Aurangabad.

REFERENCES

- Berger M J, Hubbell J H, 1987/1999. "XCOM: Photon Cross Section Database," Wb Version 1.2, available at http:// Physics.nist.gov/XCOM. National Institute of standards and Technology, Gaithersburg, MD 20899, USA (1999). Originally published as NBSIR 87-3597 "XCOM: Photon Cross Sections on a Personal Computer" (1987).
- Creagh, D.C., 1987, The resolution of discrepancies in tables of photon attenuation coefficients Nucl Instrum Methods A255, 1-16.
- Danial Salehi, Dariush Sardari and M.S. Jozani, 2015 Investigation of some radiation shieldingparameters in soft tissue Journal of Radiation Research and Applied Sciences 8:439-445.
- Demir D., Tursucu A. and Oznuluer T., 2012 Studies on mass attenuation coefficient, effective atomic number and electron density of some vitamins Radit. Environ Biophys 51:469-475.
- El-Kateb A. H., Abdul-hamid A. S., 1991 Photon attenuation coefficients study of some materials containing hydrogen, carbon and oxygen Appl.Radiat.Isot.42:303-307.
- Gowda S. Krishnaveni S. and Gowda R. 2005. Studies on effective atomic numbers and electrondensities in amino acids and sugars in the energy range 30-1333keV Nucl. Instrum. MethodsPhys.Res.B 239, 361-369.
- Gerward,L,Guilbert,N,JenserK.B.Leving,H.,2004.WinXCOM-a program for calculating x- ray attenuation coefficient.Radiat.phys.Chem.71,653-654.
- Hall E J, 1978 Radiation and life Pregamon Press, New York p.55.
- Hine, G. J., 1952. The effective atomic number of materials for various gamma ray processes. Phys. Rev. 85, 725-728.
- Hubbell J H, 1999 Review of photon interaction cross section data in the medical and biological context Phys. Med. Biol. 44 R1-22.
- Hubbell, J. H. and Seltzer SM., 1995 NIST (IR) Report No. 5632.
- Jackson, D.F., Hawkes, D.J. 1981, X-ray attenuation coefficients of elements and mixtures Phys. Rep.70, 169-233.
- Manohara S. R., Hanagodimath S. M., 2007 Studies on effective atomic numbers and electron densities of essential amino acids in the energy range1keV-100 GeV.Nucl.Instrum. Methods Phys.Res.B,258, 321-328.
- Manohara S. R., Hanagodimath S. M. and L. Gerward, 2008 Studies on effective atomic number, electron density and kerma for some fatty acids and carbohydrates. Phys.Med.Biol.53, N377-N386.
- Manjunathaguru V. and Umesh T. K., 2006 Effective atomic numbers and electron densities of some biologically important compounds containing H,C,N and O in the energy range 145-1330 keV J. Phys. B: At.Mol.Opt. Phys.39, 3969-3981.
- Midgley S. M., 2004. A parameterization scheme for the x-ray linear attenuation coefficient and energy absorption coefficient. Phys. Med. Biol.49, 307-325.
- Midgley S. M., 2005. Materials analysis using x-ray linear attenuation coefficient measurements at four photon energies Phys. Med. Biol.50, 4139-4157.
- Murat Kurudirek, 2013. Water equivalence study of some phantoms based on effective photon energy, effective atomic numbers and electron densities for clinical MV X-ray and Co-60 γ-ray beams. Nuclear Instruments and Methods in Physics Research A 701, 268-272.
- Murat Kurudirek, 2014a. Effective atomic numbers, water and tissue equivalence properties of human tissues, tissue equivalents and dosimetric materials for total electron interaction in the energy region 10keV-1GeV. Applied radiation and Isotopes 94, 1-7.
- Murat Kurudirek, 2014b. Effective atomic numbers and electron densities of some human tissues and dosimetric materials for mean energies of various radiation sources relevant to radiotherapy and medical applications. Radiation Physics and Chemistry 102, 139-146.

- Murat Kurudirek, 2014c. Effective atomic numbers of different types of materials for proton interaction in the energy region 1 keV-10GeV. Nuclear Instruments and Methods in Physics Research B 336, 130-134.
- Murat Kurudirek, 2015. Studies on heavy charged particle interaction, water equivalence and Monte Carlo simulation in some gel dosimeters, water, human tissues and water phantoms. Nuclear Instruments and Methods in Physics Research A 795, 239-252.
- Murat Kurudirek and Tayfur Onaran, 2015 Calculation of effective atomic number and electron density of essential biomolecules for electron, proton, alpha particle and multi-energetic photon interactions Radiation Physics and Chemistry 112:125–138.
- Pawar, P.P., Bichile, G.K., 2013. Studies on mass attenuation coefficient, effective atomic number and electron density of some amino acids in the energy range 0.122-1.330 MeV. Radiat. Phys. Chem.92, 22-27.
- Pravina P Pawar and Govind K Bichile journal of chem..and Pharma.Research 2012, 4(1) :59-66Sandhu G K., Kulwant Singh, Lark B. S. and Gerward, 2002 Molar extinction coefficients of some fatty acids Radiat.Phys.Chem.65, 211-215.

FIGURE CAPTIONS

Fig. 1 Narrow-beam good geometry set-up.

Fig. 2 Plot of μ_m versus photon energy for Germanium (GeO_2) oxide.

Fig. 4 Plots of σ_t versus photon energy for Germanium (GeO_2) oxide.

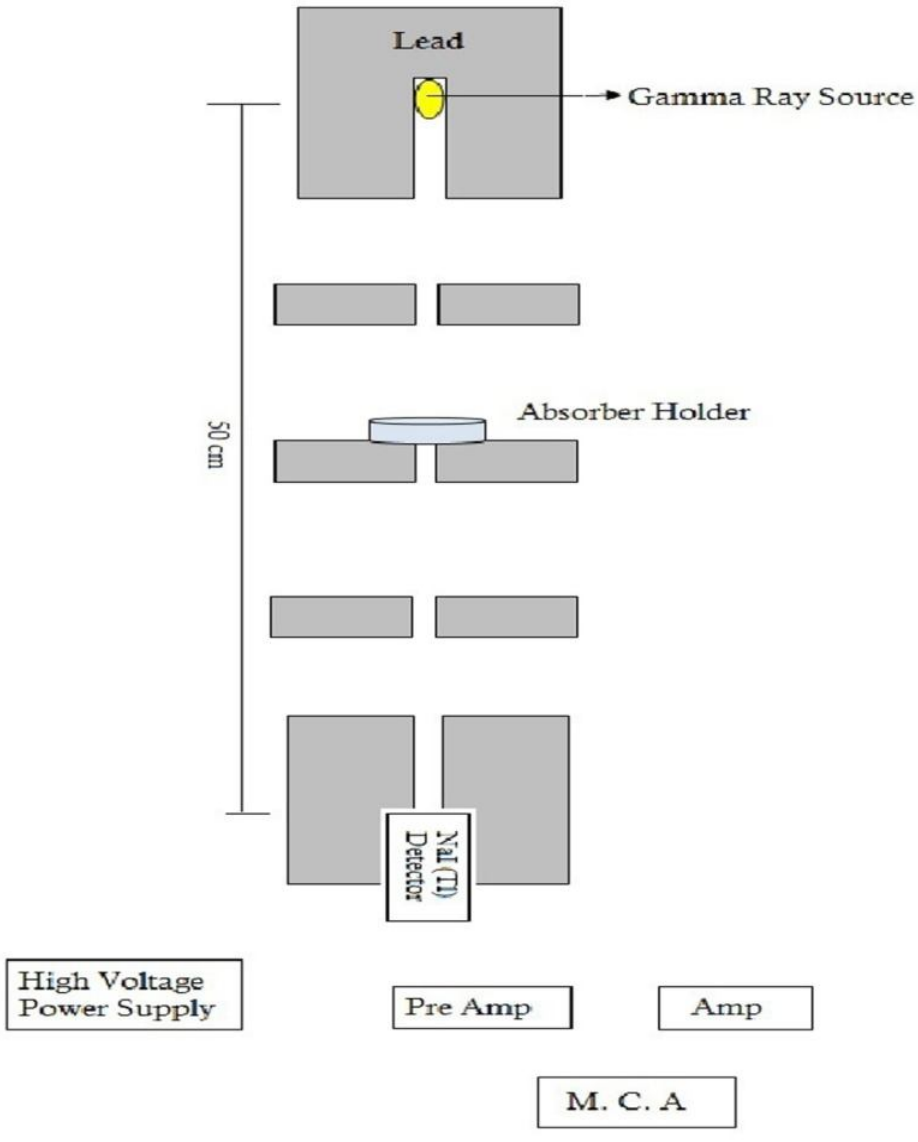

Fig-1: Narrow beam good geometry set up.

ISSN 2394 - 9954

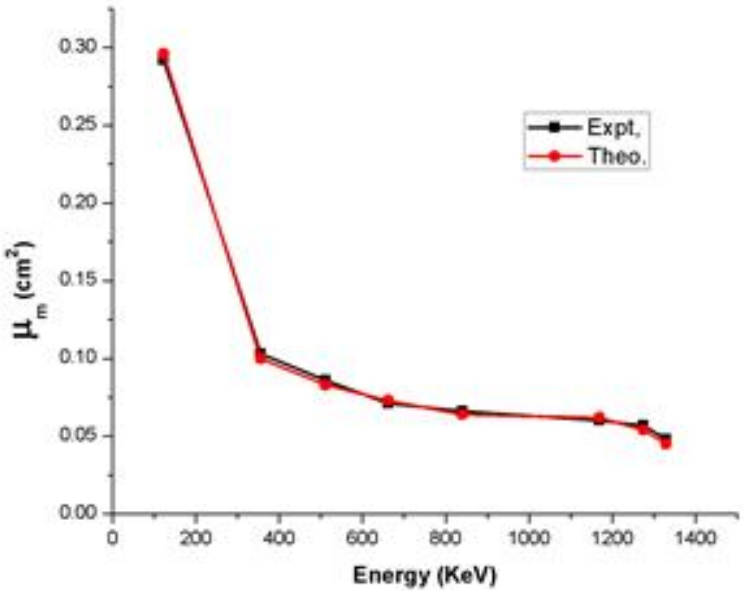

Fig-2: Typical plot of μ_m versus energy for oxides.

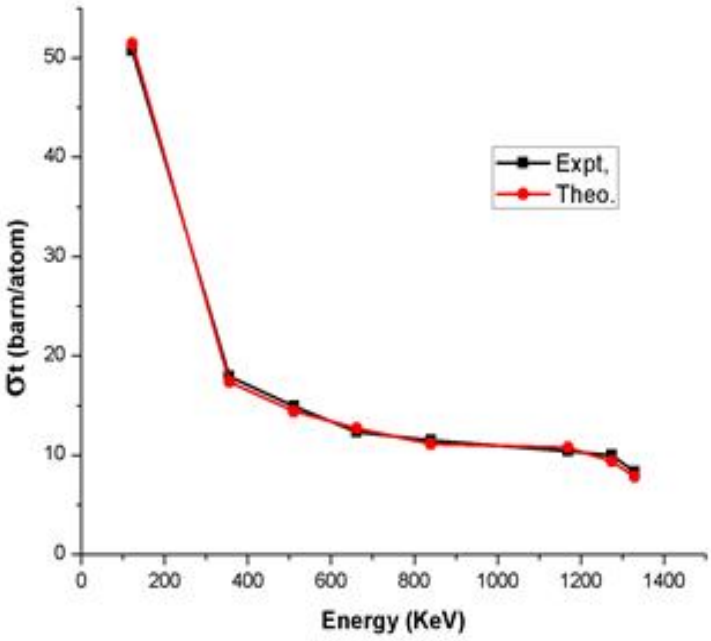

Fig-4: Typical plot of σ_t versus energy for GeO_2.

Table-1: Mass attenuation coefficient of (μ_m) and (σ_t) of Germanium oxide.

Energy	μ_m		σ_t	
Kev	**Expt.**	**Theo.**	**Expt.**	**Theo.**
122	0.292	0.296	50.72	51.42
356	0.103	0.101	17.89	17.37
511	0.086	0.083	14.93	14.41
662	0.071	0.073	12.33	12.68
840	0.066	0.064	11.46	11.11
1170	0.061	0.062	10.42	10.77
1275	0.057	0.054	09.96	09.38
1330	0.048	0.045	08.33	07.81

International Journal of Research in Science and Technology
Volume 6, Issue 1 : January - March, 2019
ISSN 2394 - 9954

OPTICAL STUDY OF CHEMICALLY DEPOSITED CDS THIN FILMS FOR OPTOELECTRONIC APPLICATIONS

V. B. Sanap[1], A. D. Suryawanshi[2] and B. H. Pawar[3]
Assistant Professor[1], Department of Physics, Yeshwantrao Chavan College, Aurangabad
Assistant Professor[2], Department of Physics, B. J. College, Pune
Ex. Head & Professor[3], P. G. Department of Physics, S. G. B. Amravati University, Amravati

ABSTRACT
Thin films of cadmium sulfide with varying thicknesses have been deposited on glass substrate from aqueous solutions of cadmium sulfate and thiourea, using ammonia solution and TEA as complexing agent. The films have average thickness between 132nm to 272nm which are uniform and adherent. The structural and morphological properties have been studied by X-ray diffractometer (XRD) and scanning electron micrograph (SEM). All the films have cubic structure. The optical constants such as absorption co-efficient (α), refractive index (n), extinction co-efficient (k), real and imaginary dielectric constants and optical conductivity (σ) were computed using the absorbance and transmission measurement from Perklin-Elmer UV-VIS lambda-35 spectrophotometer at normal incidence of light in the wavelength range 200-1000nm. The films have high absorbance of greater than 85% in the UV region were as the average transmission in VIS-NIR region is greater than 75%. The average refractive index is between 1.8 and 2.5 while the average extinction co-efficient is between 0.047 and 0.089. The band gap obtained is in the range of 2.34 eV to 2.51 eV.

Keywords: Chemical bath deposition, optical study, protective coating, thin films.

1. INTRODUCTION
Materials like sulfides, selenides and tellurides are of great importance due to wide range of technological applications for successful fabrications of low cost, high efficiency thin film solar cells[1-3], photodetectors, laser diodes[4] etc. Cadmium sulfide (CdS) thin films are one of the most promising materials for heterojunction thin film solar cells. Wide bandgap CdS (Eg = 2.42eV) has been used extensively as a window layer with Cu_2S/CdTe/$CuInSe_2$ with efficiency 14-16%. Keeping these aspects in view, more attention is being given in producing good quality CdS thin films for comprehensive optical studies and their various applications [5].

Spray pyrolysis, sputtering, electro deposition, vacuum evaporation, chemical vapour deposition and chemical bath deposition (CBD) are widely used techniques for deposition of thin films. Particularly CBD is attractive as a low cost and simple compared with other new and sophisticated methods. Also it is a controllable chemical reaction at close to room temperature. Another advantage of the CBD method with respect to the other techniques is that films can be deposited on different kinds, shapes and sizes of substrates [6-8,9].

In this work, good quality CdS thin films were prepared and their structural, morphological and optical characterization was reported, which is very important in many scientific, technological and industrial applications in the field of optoelectronic devices, especially solar cells.

2. EXPERIMENTAL DETAILS
All chemicals used in the experiments were of the highest purity grade available. Solution of 0.001M cadmium sulfate and an equal volume of 0.01M thiourea were prepared in double distilled water. pH was adjusted by adding ammonia solution slowly in the prepared solution. The solution was stirred and transferred to another container containing substrate. The resulting solution was kept at 70±2ºC for different deposition time. The substrate used is glass slide. Cleaning of substrate is important in deposition of thin films, cleaning steps and growth procedure is reported elsewhere [5,10-11]. The crystallographic structure of films was analyzed with a diffractometer (EXPERT-PRO) by using Cu-Kα lines (λ= 1.542Å).The average grain size in the deposited films was obtained from a Debye-Scherrer's formula. Surface morphology was examined by JEOL model JSM-6400 scanning electron microscope (SEM). Optical properties were measured at room temperature by using Perklin-Elmer UV-VIS lambda-35 spectrometer in the wavelength range 200-1000nm.

ISSN 2394 - 9954

3. RESULTS AND DISCUSSION

1. Influence of deposition time on Film thickness

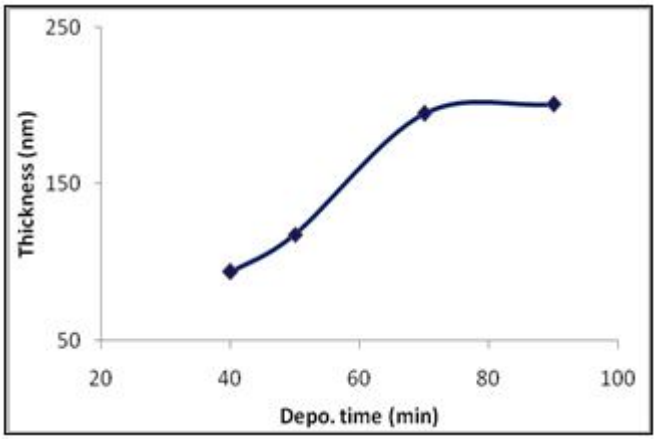

Fig-1: Variation in film thickness with deposition time for CdS film

Fig.1 shows the variation in film thickness with deposition time for the as-deposited CdS thin film. The plot shows that the thickness of film increases with deposition time. Here, the deposition process clearly shows two different growth phases: quasi linear phase and saturation phase. At the initial stage of deposition process the thickness increases; it may be due to the high concentration of Cd^{2+} and S^{2-} ions available in the solution. As the time goes, more and more CdS is formed on the substrate and the solution becomes deficient in ions, giving lower rate of deposition and film attains terminal thickness. These results are in good agreement with the results observed by many researchers [12-14].

The deposition time is optimized by measuring the thickness of the deposited film for each 10 minutes during the process. It is observed that the film thickness increases up to the time 60-70 minutes; called the quasi linear phase, then the thickness remains nearly constant, known as saturation phase. The average growth rate obtained is 3.24nm/min.

2. Structural and Morphological Properties

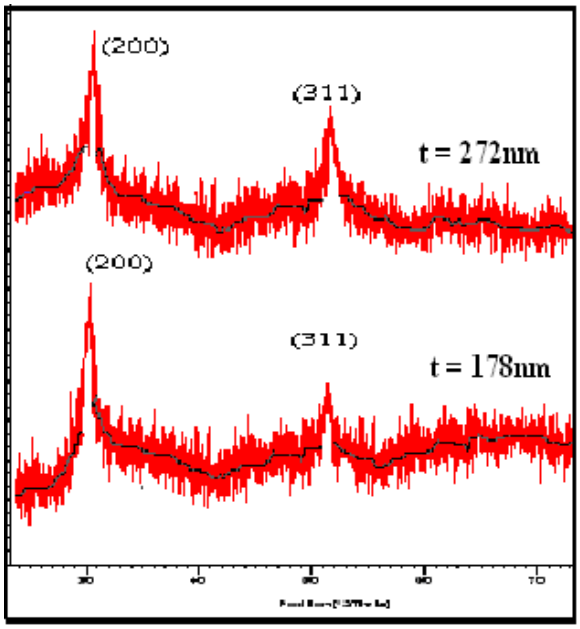

Fig-2: XRD pattern of CdS films for thicknesses 178nm and 272nm.

Fig. 2 shows the XRD pattern of CdS films for different film thicknesses. The CdS film shows two dominant crystalline peaks (200) and (311). A comparison of the peak position (2θ values) of the JCPDS XRD spectra data for CdS suggests that the as-deposited CdS films have the cubic structure with the X-ray diffraction peaks corresponding to (200) and (311) peaks.

The average grain size (g) has been obtained from the XRD patterns using Debye-Scherrer's formula [15-16],

$$g = K\lambda / \beta \cos\theta \quad \ldots (1)$$

ISSN 2394 - 9954

Where,

K = constant taken to be 0.94; λ = wavelength of x-ray used (1.542Å)

β = FWHM of the peak and θ = Bragg's angle

The grain size obtained from SEM matches with the grain size obtained by XRD.

3. Optical and solid state Properties

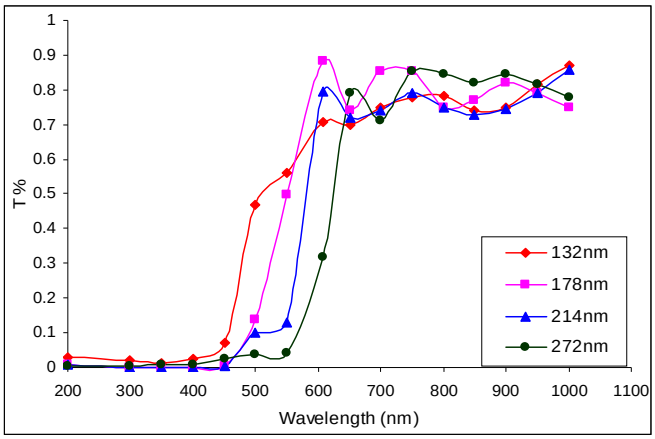

Fig-3: Optical transmission spectra of CdS thin films for varying thicknesses

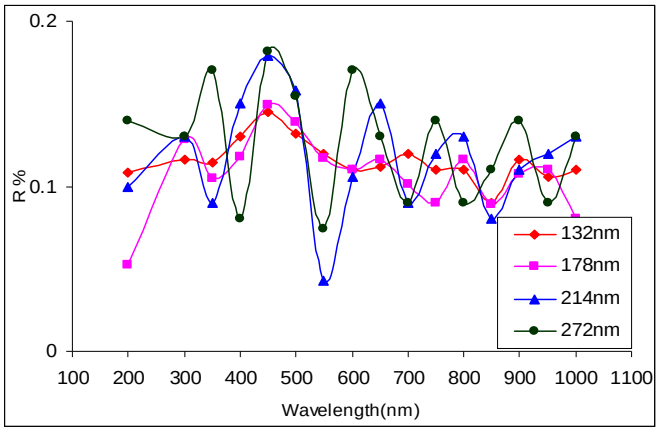

Fig-4: Optical reflection spectra of CdS thin films for varying thicknesses

Fig. 3 shows the optical transmission spectra of CdS thin films for different thicknesses. All the films show more than 75% transmittance towards VIS-NIR region, and poor transmittance (<10%) in UV region. However all the films show high reflectance (~14%) in the VIS-NIR region as shown in Fig. 4. The sharp rise in transmittance near 500nm is an identification of good crystallinity of the films. The poor transmittance in UV region made the films suitable for protective coatings from UV radiations. The film is sensitive in the range 400nm-700nm and peaked near 500nm (photopic vision). This made a good material for solar cell fabrication.

Also it is observed that with the increase in film thickness the transmittance edge shifts towards the longer wavelengths. Similar behaviors in the optical spectra of CdS films prepared by other technique have been reported elsewhere [17-18].

From the transmission data, the absorption co-efficient α was calculated using Lamberts law [16],

$$\ln (I_0/I_t) = 2.303 \log 1/T = \alpha d \quad \ldots(2)$$

Where, I_0 and I_t are the intensity of incident and transmitted light respectively. T the optical transmission and d the film thickness. The absorption co-efficient α was found to follow the relation [17],

$$\alpha h\nu = A (h\nu - Eg)^{1/2} \quad \ldots(3)$$

The band gap Eg was determined from each film by plotting $(\alpha h\nu)^2$ versus $h\nu$ and then extrapolating the straight line portion to the energy axis at $\alpha = 0$. The band gap energy Eg obtained for each thickness is different. For higher film thickness the band gap is 2.34eV and for lower it is 2.51eV. The band gap of other films is intermediate (Fig. 5).

ISSN 2394 - 9954

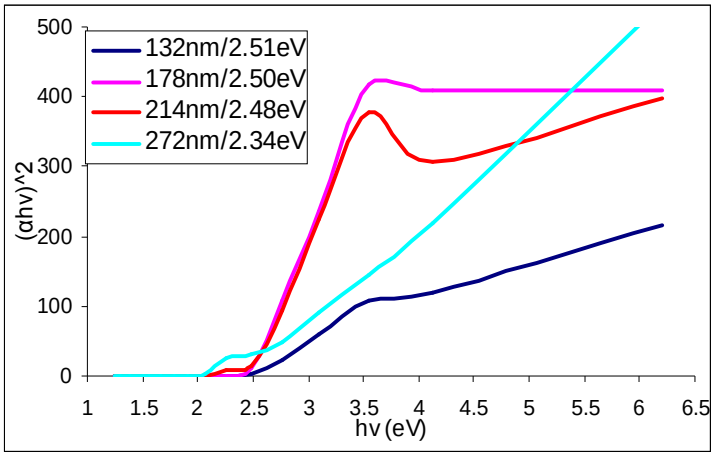

Fig-5: Plot of $(\alpha h\nu)^2$ vs hν for all CdS thin films.

Table 1 shows the variation in optical properties with the film thickness and Table 2 shows the variation in solid state properties with the film thickness prepared at 70±2°C respectively.

Table-1: Optical properties and thickness of CdS thin films prepared at 70±2°C

Sample	Film thickness t (nm)	Maximum n	Maximum k	Maximum σ x10^{13} S^{-1}
X1	132	2.23	0.25	22.23
X4	178	2.26	0.34	35.71
X5	214	2.47	0.24	32.20
X8	272	2.49	0.16	16.10

Table-2: Solid state properties and thickness of CdS thin films prepared at 70±2°C

Sample	Film thickness t (nm)	Maximum ε_r	Maximum ε_i	Energy bandgap Eg (eV)
X1	132	4.93	1.04	2.51
X4	178	5.02	1.39	2.50
X5	214	6.05	1.09	2.48
X8	272	6.18	0.67	2.34

4. CONCLUSIONS

Good quality, nanocrystalline CdS thin films with varying thicknesses and energy band gaps between 2.34 and 2.51eV have been grown successfully by CBD technique. The films have been characterized using optical measurements as T-R-A spectra, optical band gap energy as well as thickness, structure, surface morphology. The high absorbance in UV region of the films made them good materials for large area selective coatings for photo thermal conversion of solar energy and as a solar absorber for solar cells. Due to poor transmission in the same region, the films could be effective as coatings for protection from UV radiations.

ACKNOWLEDGEMENTS

The authors are grateful to Head, DME, VNIT Nagpur for providing XRD and SEM facilities. We would also like to acknowledge Head, Biotech department, Y. C. College, Sillod for UV-VIS-Near IR facilities.

REFERENCES

[1] Arturo Morales-Acevedo (2000) *Solar Energy*, 80, 675.

[2] Paulson P D & Dutta V. (2000) *Thin Solid Films*, 370, 299.

[3] Emziane M, Durose K, Romeo N, Bosio A & Halliday D P. (2005) *Thin Solid Films*,480, 377.

[4] Panda S K, Chakrabarti S, Satpati B, Satyam P V & Choudhuri S.(2004) *J Phys D Appl Phys*, 37, 628.

[5] Sanap V B, Pawar B H. (2009) *Chalcogenide Letters*, 6(8), 415-419.

[6] Pawar S H, Bhosale C H. (1986) *Bull. Matter Sci.*, 8-3, 419-422.

[7] Salazar Y A et al. (2006) *Brazilian Journal of Physics*, 36-3B.

[8] Vazquez Luna J G et al. (1999) *Cryst Res Technol*, 34-8, 949-958.

ISSN 2394 - 9954

[9] Ugwu E I & Onah D V. (2007) *The Pacific J of Sci & Tech,* 8-1, 155-161.

[10] Nair P K, M.T.S. Nair et al. (1989) *J. Phys D,* 22, 829.

[11] Kitaev G, Mokrushin S, Uritskaya A. (1965) *Kolloidn Z*, 27, 51.

[12] T.L. Chu, S.S. Chu, et.al.(1982) *J. Electrochem. Soc.* 139, 2443.

[13] Kessler J, Velthaus KO, et.al. (1992) *Proceedings of the 6th International Photovoltaic Science and Engineering Conference,* 1005.

[14] J.M Nakanishi T, Ito K. (1994) *Sol. Energy Mater. Sol.Cells*, 35, 171.

[15] Adachi A, Kudo A and Sakata T. (1995) *Bull Chem Soc Jpn,* 68, 3283.

[16] Sahay P P, Nath R K and Tiwari S. (2007) *Cryst Res Technol***,** 42 3, 275-280.

[17] Grecu R, Popovici E J, Ladar M et al. (2004) *Journal of Optoelectronics & Advanced Materials,* 6 1, 127-132.

[18] Ezema F I & Osuji R U. (2006) *Journal of Applied Sciences,* 6 8, 1827-1832.

International Journal of Research in Science and Technology
Volume 6, Issue 1 : January - March, 2019
ISSN 2394 - 9954

ENHANCEMENT IN OPTICAL PROPERTIES OF NICKEL THIOUREA NITRATE DOPING IN POTASSIUM DIHYDROGEN PHOSPHATE (KDP)

Y. B. Rasal[1], R. N. Shaikh[2], M. D. Shirsat[3] and S. S. Hussaini[4]
Assistant Professor[1], Smt. S. K. Gandhi Arts, Amolak Science, P. H. Gandhi, Commerce College Kada, Tal. Ashti, Dist. Beed
Assistant Professor[2,4], Crystal Growth Laboratory, Department of Physics, Milliya Arts, Science and Management Science College, Beed
Professor[3], RUSA Centre for Advanced Sensor Technology, Dr. Babasaheb Ambedkar Marathwada University, Aurangabad

ABSTRACT
In present investigation pure and Bis Thiourea Nickel Nitrate doped KDP crystals were grown by slow solution evaporation method at room temperature. The incorporation of Bis Thiourea Nickel Nitrate in KDP has been qualitatively analyzed by Fourier transform infrared analysis. The second harmonic generation (SHG) efficiency of doped KDP crystal was tested by Kurtz-Perry powder technique and was found to be 1.65 times that of KDP material. The optical transparency of the grown crystal was examined in the range of 200-900 nm using UV-visible studies. The transmittance data was used to determine the optical conductivity, refractive index and extinction coefficient of grown crystal for possible nonlinear optical (NLO) applications.

Keywords: 1 Slow evaporation method, 2 Nonlinear optical, 3 Optical studies, SHG efficiency.

1. INTRODUCTION
The Nonlinear optical (NLO) crystals have wide applications in the field of optical storage communications and optical computing system. Also, NLO materials exhibits excellent electro optical and non-linear optical properties, is used in several applications as the frequency conversion and electro-optical modulation [1-2]. The Potassium dihydrogen phosphate (KDP) is reference system for nonlinear optic device applications. The attempts have been made to uplift the properties of KDP crystal either by doping various impurities or by growing crystal using specific crystal growth technique [3-4]. Thiourea molecules play an important role in the growth of nonlinear optical crystals. The thiourea molecule is an interesting inorganic matrix modifier due to its large dipole moment and ability to form extensive network hydrogen bonds. The metal complexes have high optical nonlinearity excellent transmittance in UV Visible region, good thermal and mechanical stability, so attracted by many researchers [5-6].

In literature, there is least work on thiourea metal complex mixed KDP crystals, P. Kumaresan et al have reported the effect of copper thiourea complex on KDP in view of structural, optical and thermal behavior [7], hence in the present investigation; the attention is focused on the influence of thiourea metal complex, Thiourea Nickel Nitrate (TNN) on optical, spectral properties of KDP for its improved NLO applications.

2. EXPERIMENTAL PROCEDURE
Thiourea and Nickel Nitrate were dissolved in the deionized water in the molar ratio 2:1and solution is well stirred. After six hours the prepared mixture was filtered by no.1 whatman filter paper and kept for evaporation [8]. The purity of BTNN salt was achieved by successive recrystallization method. The high purity KDP salt was dissolved in double distilled deionized water until the supersaturation was achieved. The measured quantity of 0.1 mole% BTNN was slowly added to the supersaturated solution of KDP. The solution was allowed to agitate for 6 hrs on magnetic stirrer to acquire the homogeneous doping. This doped solution was filtered and kept for slow evaporation at room temperature. The well phased, good quality transparent seeds were harvested within 12-14 days. The photograph of 0.1 mole% BTNN doped KDP crystal of dimension 15×6×3 mm^3 is shown in Fig. 1.

Fig-1: 0.1BTNN doped KDP crystal

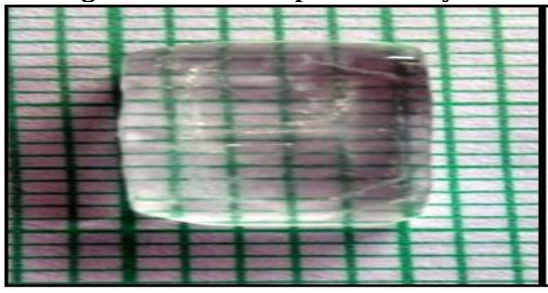

Fig-2: FT-IR spectrum of doped KDP crystal

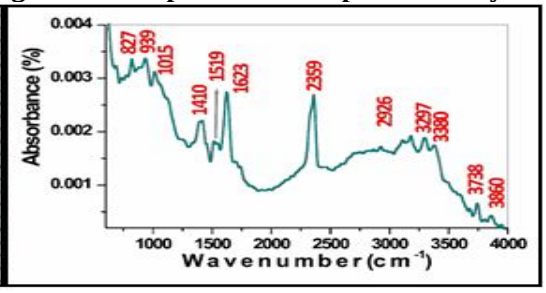

ISSN 2394 - 9954

3. RESULT AND DISCUSSION

3.1 FT-IR analysis

The FT-IR spectra of 0.1BTNN doped KDP solid crystal was recorded using Bruker a-ATR instrument in the range 500-4000 cm^{-1} to confirm the incorporation of BTNN. The recorded absorbance FT-IR spectrum of grown crystal is depicted in Fig. 2. The absorption bands between 2750-3860 cm^{-1} represents the Symmetric and asymmetric stretching of NH_2 molecule. Free O-H stretching hydrogen bonded of KDP was observed at peak 3738 cm^{-1}. The band observed at 3380cm^{-1} represents N-H Hydrogen bonded stretching. The peak 2359 cm^{-1} was assigned to P-O-H bending of KDP. The absorption band at 1623$cm^{-1}$was observed due to O=P–OH stretching of KDP. The peak at 1519 cm^{-1} in the spectra is assigned to C-N stretching. Absorption band at 1410 cm^{-1} is in the spectra due to N-H Stretching. The P-O-H stretching of KDP in the spectra was observed due to 939 cm^{-1}. The absorption at 1015 cm^{-1} can be assigned to C-N stretching. The peak at 827 cm^{-1} in the spectra is attributed to C=S stretching [8-9].

Fig-3: Plot of SHG output intensity vs. λ **Fig-4: Transmittance vs. wavelength**

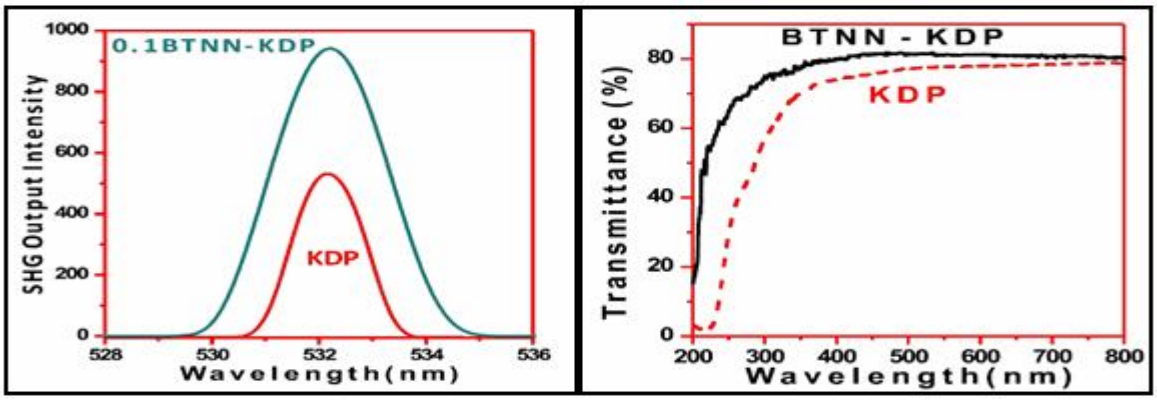

3.2 Kurtz-Perry powder test

The effective frequency doubling behavior of the 0.1BTNN doped KDP crystal was determined by Kurtz-Perry powder SHG test [10]. The incident Q-switched Nd:YAG laser used of wavelength 1064 nm with repetition rate 10 Hz and pulse duration 6 ns delivering the input energy of 5.4□J/pulse. The KDP and doped KDP crystals were finely grounded to micro granules of uniform size and the individual sample was multishot by a polarized gaussian beam of Nd:YAG laser. The output signals were collimated through the array of photomultiplier tube to record the output SHG intensity of the sample. The emission of sharp green light from the crystalline powder confirmed the second order NLO behavior of doped crystal and the output SHG intensities are plotted in Fig.3. The enhanced SHG efficiency of doped crystal is found to be 1.65 times that of KDP material.

Fig-5: Optical conductivity vs. Photon energy Fig-6 (a) Refractive Index vs. wavelength (b) Extinction Coefficient vs. wavelength

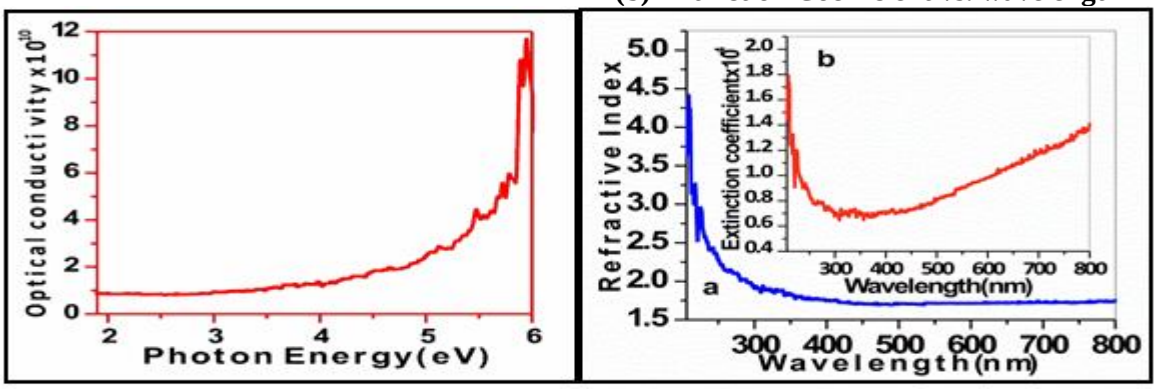

3.3 UV-Visible Studies

The pure and BTNN doped KDP single crystals of 1 mm thickness were subjected to UV-visible study using the Shimadzu UV-2450 spectrophotometer to assess the optical transparency within the range of 200 to 900 nm. The recorded transmittance spectrum (Fig. 4) reveals that transmittance of BTNN doped KDP crystal is up to 81% in entire visible region. It is observed that the transmittance of BTNN doped KDP crystal sharply falls near 200 nm which is expressed due to strong n to π* transition associated with nitro chromophore of BTNN [11]. The optical conductivity is a measure of frequency response of the material when irradiated with light. The optical conductivity is calculated by using formula $\sigma = \alpha n C/4\pi$.The plot between optical conductivity against

ISSN 2394 - 9954

photon energy was depicted in Fig. 5. The refractive index is determined by using formula n = [1/T + (1/T - 1)], where T is Transmittance. The extinction coefficient was calculated by using the equation, $K = \lambda\alpha/2\pi$. The variation of extinction coefficient (K) helps to evaluate the loss of electromagnetic energy in visible region. The plots refractive index and extinction coefficient vs. wavelength is as shown in Fig. 6(a) and (b) respectively. The improved optical transparency, high optical conductivity of the grown crystal causes to enhance the SHG efficiency which is found to be 1.65 times KDP [12]. This suggest that 0.1 BTNN doped KDP crystal suggests its prominence for NLO applications [13].

CONCLUSIONS

The 0.1BTNN doped KDP crystal was grown successfully by slow evaporation solution technique at room temperature. The FTIR analysis established the incorporation of Bis thiourea nickel nitrate in KDP crystal. The NLO studies confirmed the superior non-linear behavior of doped crystal than KDP crystal. The SHG efficiency of doped crystal is higher by 1.65 times that of KDP crystal. The UV-Visible study reveals that optical parameters of the grown crystal are improved in the entire visible region suggest its suitability in NLO applications.

REFERENCES

1. R N Shaikh, Mohd Anis, A B Gambhire, M D Shirsat and S S Hussaini (2014),"Growth, optical and dielectric studies of glycine doped ammonium dihydrogen phosphate NLO crystal: potential material for optoelectronics applications", Mater. Res. Exp.Vol. 1, 015016.
2. Mohd Anis, R.N. Shaikh, M.D. Shirsat, S.S. Hussaini (2014),"Investigation of optical and electrical properties of L-Cystein doped zinc thiourea chloride (ZTC) crystal for nonlinear optical (NLO) applications", Optics Laser Technol. Vol. 60, 124-129.
3. S. Balamurugan, G. Bhagavannarayana, P. Ramasamy (2008),"Growth of unidirectional potassium dihydrogen orthophosphate single crystal by SR method and its characterization", Mater. Lett. 62, 3963-3965.
4. S. S. Hussaini, N. R. Dhumane, G. Rabbani, P. Karmuse, V. G. Dongre, M. D. Shirsat, Growth and high frequency dielectric study of pure and thiourea doped KDP crystals, Cryst. Res.Technol. Vol.42 (2007) 1110-1116.
5. V. Ganesh, Ch. Snehalatha Reddy, Mohd. Shakir, M. A.Wahab, G. Bhagavannarayana, K. Kishan Rao (2011),"Comparative study on Bis thiourea cadmium acetate crystals using HRXRD, etching, microhardness, UV-visible and dielectric characterizations", Physica B Vol. 406 259-264.
6. J. Thomas Joseph Prakash, L. Ruby Nirmala (2010),"Synthesis, Spectral and Thermal Properties of Bis Thiourea Zinc Acetate (BTZA) Single Crystals", Intern. J. Computer Applical. Vol.6, 0975- 8887.
7. P. Kumaresan, S. Moorthy Babu, P. M. Anbarasan, Effect of copper thiourea complex on the performance of KDP single crystals", J. Optoelect. Adv. Mater. Vol. 9 (2007) 2787-2791.
8. V. Revathi & V. Rajendran (2013),"Growth and characterization of semi-organic nickel bis thiourea nitrate single crystal", Scholars Research Library, Der Pharma Chemica Vol. 5 105-111.
9. Norman B. Colthup, L.H. Daly, S.E. Wiberley (1990), "Infrared Spectroscopy", American Cyanamid Company San Diego, California. Toronto: Academic Press, Print Book ISBN: 9780121825546, eBook ISBN: 9780080917405.
10. S.K. Kurtz, T.T. Perry (1968), "A Powder technique for the evaluation of Nonlinear Optical Materials" J. Appl. Phys. Vol. 39, 3798-3813.
11. M. Anis, G. G. Muley, G. Rabbani, M. D. Shirsat and S. S. Hussaini (2015),"Optical, photoconductivity, dielectric and thermal studies of L-arginine doped zinc thiourea chloride crystal for photonics applications", Mater. Technol. Vol. 30, 129-133.
12. Y. B. Rasal, M. Anis, M. D. Shirsat & S. S. Hussaini (2015),"Growth, structural, UV–visible, SHG, mechanical and dielectric studies of bis-thiourea zinc chloride doped KDP crystal for NLO device applications", Mater. Rese. Innov. Vol. 21, 45-49.
13. Mohd Anis, M.D.Shirsat, Gajanan Muley, S.S.Hussaini (2014),"Influence of formic acid on electrical, linear and nonlinear optical properties of potassium dihydrogen phosphate (KDP) crystals", Physica B Vol. 449 61-66.

International Journal of Research in Science and Technology
Volume 6, Issue 1 : January - March, 2019
ISSN 2394 - 9954

MAGNETIC AND ELECTRICAL PROPERTIES OF BARIUM HEXAFERRITE NANOPARTICLES SYNTHESIZED BY SOL GEL AUTO COMBUSTION METHOD

Ravindra C. Alange
Department of Physics and Electronics, Shri Madhavrao Patil Arts Commerce & Science College, Murum

ABSTRACT
Barium hexaferrite ($BaFe_{12}O_{19}$) nanoparticles were prepared by sol-gel auto combustion method.Analytical grade chemicals were used for the synthesis of $BaFe_{12}O_{19}$ hexaferrite nanoparticles. The magnetic and electrical properties were investigated. The magnetic behaviour of the samples was studied using vibrating sample magnetometer technique. The magnetic properties such as saturation magnetization, remanence, and coercive field of samples were calculated based on magnetization curves. The M-H curves recorded at room temperature exhibits a typical hysteresis loop indicating the ferromagnetic nature of the prepared samples. The DC electrical resistivity studies of the prepared samples were carried out in the temperature range of 300–873 K using a standard two-probe method. The DC resistivity decreases with increase in temperature, which indicates the semiconducting nature

Keyword: Nanoparticles, VSM, ferrite.

1. INTRODUCTION

Permanent magnetic materials have acquired great scientific, as well as industrial and technological interest due to their crucial role in the fabrication of essential components for a multitude of devices and machine in active use nowadays [1]. The search for new magnetic materials for high performance magnet applications has led to an exponential growth in both the scientific research in this field, and the investment in the development of such materials. The discovery of M-type hexagonal ferrites ($MFe_{12}O_{19}$, where M = Ba, Sr, Pb) in early 1950s can be considered one of the most important discoveries in the field of materials development, functionalization, and commercialization during the past few decades [2]. Among the several types of ferrites, $BaFe_{12}O_{19}$ is a hard ferrite with a hexagonal magneto-plumbite structure belonging to space group P63/mmc. It is important material due to its high Saturation Magnetization (M_S), High Coercivity (H_C) and High magnetic anisotropy [3]. -type Strontium and Barium hexaferrite continuing its dominance in permanent magnet market due to its high saturation magnetization (Ms), moderate Coercivity (Hc) and high magneto crystalline anisotropic field [4]. The characteristic magnetic properties of M-type ferrite lie in its hexagonal crystal structure, where 24 Fe^{3+} ions are distributed among five different crystallographic sites. There are some methods, offering to produce nanocrystalline materials barium hexaferrite like mechanical alloying [5], sol-gel [6], and hydrothermal method [7], solution combustion. Among them sol gel auto combustion method was used to prepared Barium hexaferrite nanoparticles. The aim of the present paper is to synthesis and understands structural and electrical properties.

2. EXPERIMENTAL DETAILS

2.1 Synthesis and Characterization

Analytical grade chemicals like barium nitrate $Ba(NO_3)_2$, Ferric nitrate $Fe(NO_3)_3.9H_2O$ and citric acid ($C_6H_8O_7.H_2O$) as a fuel were used as starting materials. The metal nitrate to citric acid ratio was taken as 1:3. The pH value was adjusted to 7 by adding the ammonia solution drop by drop. Then the solution was heated on hot plate at 200^o C with constant stirring until gel was formed. Instantaneously gel ignites with the formation of large amount of gas, resulting in to light weight voluminous powder. The resulting precursor powder was calcined at 950^0C for 8 hrs to obtain pure $BaFe_{12}O_{19}$ hexaferrite powder. The prepared nanoparticles were used for further characterization. The magnetic measurements were recorded at room temperature using vibrating sample magnetometer. In order to measure DC electrical resistivity was measured by two probe technique as a function of temperature.

3. RESULTS AND DISCUSSION

3.1. Magnetic properties

The magnetization (M) versus applied magnetic field (H) that is M-H plots of the samples is shown in Fig. 1. The plot indicates the normal hysteresis loop and was used to evaluate the values of saturation magnetization (Ms), remenance magnetization (Mr) and Coercivity (Hc). All the obtained magnetic parameter from M-H loop is in reported range [8] . The magnetization behavior is similar to that of hard magnetic materials. The saturation magnetization at 9 kOe field is 1.6 emu/gm and coercivity is found to be 3 kOe.

ISSN 2394 - 9954

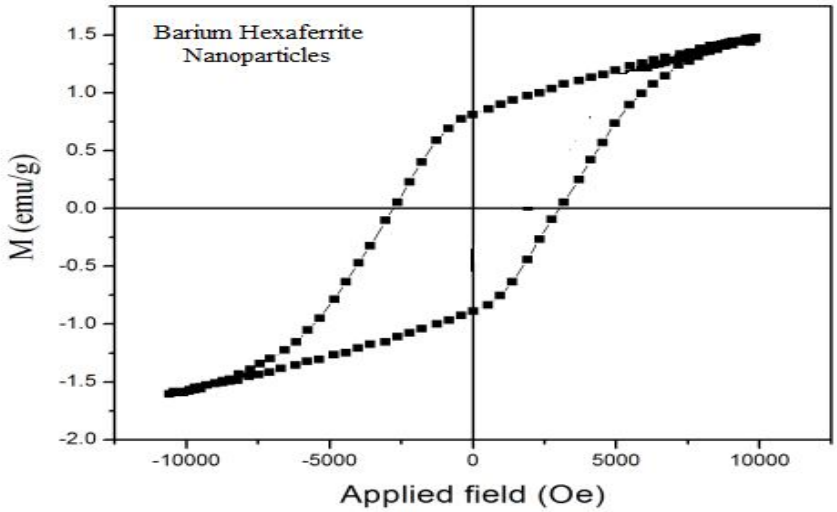

Fig-1: M-H loop of Barium ferrite nanoparticles

3.2 DC resistivity Measurement

The DC electrical resistivity measurements was measured using two probe method within the temperature range of 300–923 K. Fig.2 shows the It is clear from Fig. 2 that the resistivity plot exhibit semiconducting behaviour and obeys Arrhenius relation [9].

$$\rho = \rho_0 \exp(\frac{E_a}{k_B T})$$

where, ρ_0 is the pre-exponential factor, E_a is the activation energy, k_b is the Boltzmann constant and T is the temperature. From the analysis of Dc resistivity plot, it is observed that a resistivity plot is divided into two regions high temperature (paramagnetic region) and low temperature (ferromagnetic region) [9].

It was found that the activation energy in paramagnetic region is greater than that of ferromagnetic region. It was found that the DC electrical resistivity decreases as temperature increases, which indicates the semiconducting nature. The conduction mechanism operating at these two levels can be explained on the basis of electron hopping between Fe^{2+} and Fe^{3+} at octahedral sites [10].

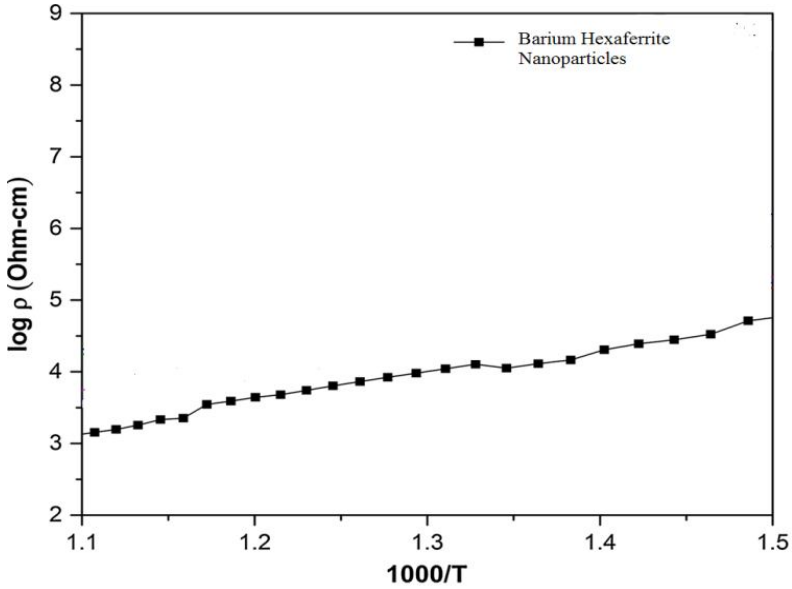

Fig-2: Variation of DC electrical resistivity with reciprocal of temperature og Barium hexaferrite nanoparticles

4. CONCLUSIONS

The nanocrystalline $BaFe_{12}O_{19}$ hexaferrite was successfully synthesized by sol-gel auto combustion synthesis technique. The M-H curves recorded at room temperature exhibits a typical hysteresis loop indicating the ferromagnetic nature of the prepared samples. All the magnetic parameters viz. saturation magnetization (Ms), remanence magnetization (Mr) and coercivity (Hc) are in reported range. DC electrical resistivity decreases with increase in temperature obeying Arrhenius relation.

ISSN 2394 - 9954

REFERENCES

[1]. M. Meshram, N.K. Agrawal, B. Sinha, J. Magn. Magn. Mater. 271, 207–214 (2004)

[2]. P. Tenaud, A. Morel, F. Kools, J. Le Breton, L. Lechevallier, J. Alloy. Compd. 370, 331–334 (2004)

[3]. T. Nakamura, E. Hankui, , J. Magn. Magn. Mater. 257, 158–164 (2003)

[4]. O. Kubo, T. Ido, H. Yokoyama, ,Magn. IEEE Trans 18, 1122–1124 (1982)

[5]. S. Ram, D. Bahadur, D. Chakravorty, J. Magn. Magn. Mater. 67, 378–386 (1987)

[6]. J. Uher, W.J. Hoefer, , Microw. Theory Tech. IEEE Trans. 39, 643–653 (1991)

[7]. R. Tiwary, S. Narayan, O. Pandey, , J. Min. Metall.Sect. B. 44, 91–100 (2008)

[8]. T.-S. Chin, , J. Magn. Magn. Mater. 209, 75–79 (2000)

[9]. M.J. Iqbal, M.N. Ashiq, , Chem. Eng. J. 136, 383–389 (2008)

[10] M.J. Iqbal, M.N. Ashiq, J.M. Munoz, Magnetic, Scripta Mater. 57,1093–1096 (2007)

International Journal of Research in Science and Technology
Volume 6, Issue 1 : January - March, 2019
ISSN 2394 - 9954

SYNTHESIS OF Mg SUBSTUTE NiCuZn FERRITE

B. D. Ingale
Azad College, Ausa, Latur

ABSTRACT
The ferrite composition [Ni $_{0.25-x\ Mg\ x}$ $Cu_{.2}$ $Zn_{0.55}$] Fe_2O_4 with values x= 0.00, 0.05, 0.1, 0.15, 0.2, 0.25 were synthesized by auto combustion method. XRD analysis of prepared ferrite powder shows the cubic spinal structure. The resultant powder were calcined at 650 $^0{}_C$ / 2hr and the pressed ferrite were sintered at 950 ^{0}c / 4hr. The initial permeability were measured with frequency range 100Hz to 5MHz. High permeability in the composition x=0.15 was due to better densification and lower magnitostriction constant. There is no noticible change in the lattice parameter.

INTRODUCTION
Present day information technology plays important role in human life. The electromagnetic components are more demanded having very small size, low prize and high efficiency. The ferrites are used in various field like surface mounting technology component which is widely used in electronic things such as digital camera, Cellular phone and computer. NiCuZn ferrite is material for M.L.C.I. due to its better magnetic properties at perticuler higher frequency The Mg -Cu-Zn ferrite is magnetic material for wide applications for environmental stability. The initial permeability is high at low magnitostriction constant The magnitostriction constant of Mg- Cu-Zn is lower than Ni-Cu-Zn [1-6]. Here expectation is that by adding the Mg, the Mg-Cu-Zn ferrite is to be prepared.

3. EXPERIMENTAL.
The analytical grade magnesium nitrate [Mg $[N0_3]_2.6H_2O$], zinc nitrate [Zn $[NO_3]_2.6H_2O$], copper nitrate [Cu $[NO_3]_2.6H_2O$], iron nitrate [Fe $[NO_3]_2.9H_2O$] and citric acid [$C_6H_8O_7H_2O$] were used to prepare [Ni $_{0.25-x}$ Mg $_{0.20}$ Cu $_{0.20}$ Zn $_{0.55}$] Fe_2O_4 with x=0.0, 0.05, 0.1 0.15, 0.2, 0.25 by autocombusion method. The metallic nitrates and citric acid were dissolved in de-ionized water and mixed in 1:3 m ratio of nitrate to citric acid. The solution was heated to transfer it in to gel. Then the dried gel burnt in self propagating combustion manner until all gel was completely burns out to form fully loose powder. The burnt precursor powder was calcined at 650 ^{0}C / 2hr. The calcined powder was granulated by using PVA as binder. It is uniaxially pressed at 1.5 to 2 ton / cm^2 to form pellet and toroidal specimen. These specimens were sintered at 950 ^{0}C / 4hr. In air atmosphere the sintered ferrites were characterized with respect to phase identification, crystallite size, and lattice parameter determined using X-ray diffraction with CuKα radiation [λ =1.5406Å]. Bulk density was measured by using formula, dx = ZM/Na^3. For obtaining the value of permeability, the inductance was measured with L-C-Q-R meter

Table-1: Various parameters for [N i $_{0.25-x}$ Mg $_x$ Cu $_{0.20}$ Zn $_{0.55}$] Fe_2O_4 ferrite.

Sr. No.	Content x Mg	Bulk density gm/cm^3	Permeability (μ)
01	0.00	5.17	429
02	0.05	5.55	290
03	0.1	6.12	372
04	0.15	6.99	1177
05	0.2	6.48	305
06	0.25	6.66	118

RESULT AND DISCUSSION
In the present work bulk density increases with Mg addition. The lower bulk density of Ni-Cu-Zn at x=0 is due to the absences of Mg in the composition.

The permeability is large at x=0.15 composition of Mg-Cu-Zn ferrite. It is primarily attributed to increase in bulk density. It is seen that the ferrites with large bulk density, posses' higher permeability. The high initial permeability was observed at composition x = 0.15 [7]

The permeability can be calculated by using inductance and following formula.

μi = L / 0.0046 N^2.h .log 10 [d2/d1] where, L-Inductance in micro hennery. d1-inner diameter, d2-outer diameter of toroid, h-height in inches.

ISSN 2394 - 9954

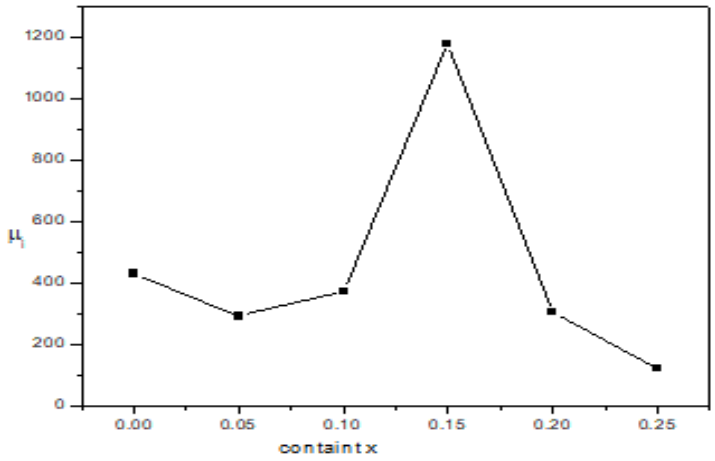

Fig-2: Permeability v/s Mg content. Of Ni $_{0.25-x}$ Mg $_{x}$ Cu $_{0.20}$ Zn $_{0.55}$] Fe_2O_4 ferrite

However the initial permeability of composition, x=0 is lower than the composition x=0.15.this may be attributed due to lower grain size and absence of Mg in composition.

In [Ni $_{0.25-x}$ Mg $_{x}$.Cu $_{0.2}$.Zn $_{0.55}$] Fe_2o_4 the permeability is stable in frequency range

100Hz to1Mhz.its dispersion occur above 1 MHz.

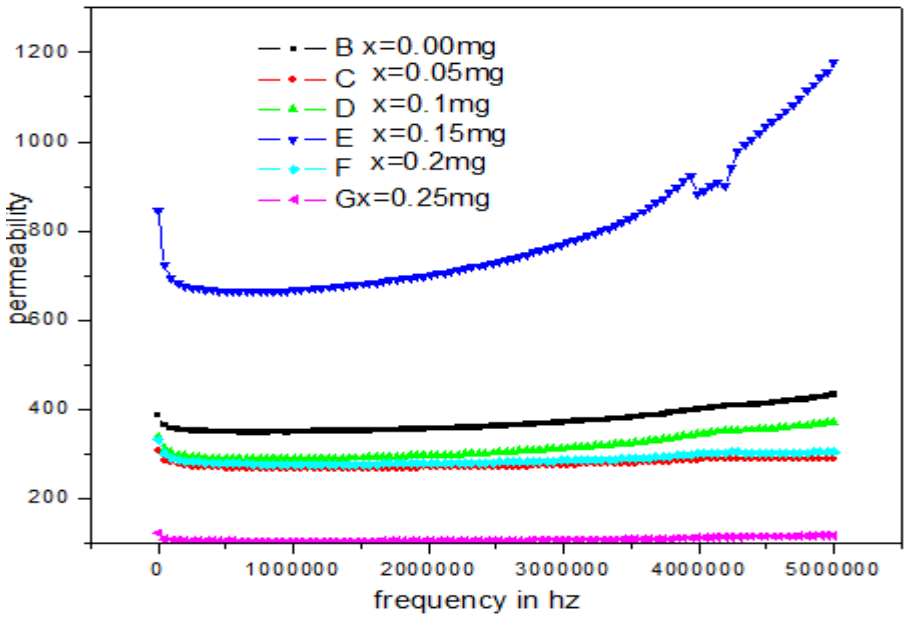

Fig-3: Plot of frequency dependency of permeability of Ni $_{0.25-x}$ Mg $_{x}$ Cu $_{0.20}$ Zn $_{0.55}$] Fe_2O_4 ferrite.

4. CONCLUSIONS

The experimental results given above indicate that the Mg addition in Ni-Cu-Zn ferrite has significant role in improvement of magnetic properties. . With increasing Mg content, the initial permeability increases up to x=0.15 The bulk density are increased with Mg addition. The obtained results provide important information for improving significant properties of Ni-Cu-Zn ferrite.

REFRANCES

1. T. Nakamura, J. Magn.Magn.Mater.168 [1997] 285.
2. M.Fujimoto, J. Am Ceram.Soc. 77[11] 2873.
3. T. Ayoma. K. Hirota, O. yamguchi, J Am ceram.Soc.79 (10)(1996) 2792.
4. G.F. Dione R. G.west J.App.phys.81 (8) (1997) 4794.
5. S. F.wang. Y. R. Wang; Thomas C. K.yang; P. J.wang. C.A. Lu; J.Magn. Mater 217(2000).
6. Magn.Mater.251 [2002] 316-322Xi-Wei Qi, Ji Zhou, Zhenxing Yue, Zhi-Lun GUI. Long-Tu Li, J. Magn.
7. G. Ranga Mohan; D.Ravinder, A.V.Raman Reddy, B. S.Boyanov, mater.Lett. 40 (1999) 39

International Journal of Research in Science and Technology
Volume 6, Issue 1 : January - March, 2019
ISSN 2394 - 9954

SYNTHESIS AND CHARACTERIZATION OF NICKEL FERRITE MAGNETIC NANOPARTICLE BY SOL GEL AUTO-COMBUSTION METHOD

P. P. Bhosale [1], M. S. Kale[2], S. D. Nimbalkar [3] and Madhav N. Rode[4]
[1,2]Department of Physics, New Arts, Commerce, Science College, Ahmednagar
[3]Department of Electronics RNC Arts, JDB Commerce & NSC Science College, Nashik Road
[4]Department of Physics, Parli Vaidyanath College, Parli vaijnath

ABSTRACT
Nickel ferrite nanoparticles are synthesized by using sol gel auto combustion method. The sol gel method is excellent, inexpensive and low temperature synthesis technique for formation of nickel ferrite nanoparticles. Ammonia plays an important role for adjusting pH neautral. Temperature provided lies in between 80^0C-90^0C.The prepared nickel ferrite nanoparticles are characterized by X-ray diffraction technique (XRD), vibrating sample magnetometer (VSM) and Fourier transform infrared spectroscopy (FTIR). By using XRD technique synthesized nickel ferrite nanoparticles having spinal structure and crystallite size is 44nm for more intense peak. VSM technique used for finding saturation magnetization, coercivity, retaintivity with the help of hysteresis graph having values 32.856emu/g, 200.59G, 8.5136emu/g. Fourier transform infrared spectrometer confirms the streching frequencies of corresponding bonds.

Keywords: Ferrite XRD, VSM, FTIR.

1. INTRODUCTION

Last few years researches has interest to form magnetic nanoparticles because of its applications in high density recording, colour imaging, ferrofluids, high frequency devices, magnetic refrigerators(1). Ferrites are a ceramic compound consists of a mixture of iron oxide and one or more other metals which shows ferromagnetic properties. To synthesized nanosized ferrites have attracted attention because of its applications. Ferrite has general formula Mfe2o4 where M represents metallic cations like Fe, Mn, Ni, Co, Zn, Cu, Al or a mixture of these(2). Ferrites are synthesized by using different techniques like hydrothermal method(3-4), citrate precursor(5), freeze drying(6),sol-gel method(4), Spray drying(7).

The sol-gel technique is excellent, inexpensive and low temperature to form powder (solid) nanoparticles. The inverse spinal nickel ferrites shows interesting magnetic properties in nanocrystalline form compaired with those of the micrometer size grains (8). The crystal structure is FCC with unit cell contains 32 O2-, 8Ni 2+ and 16Fe3+ ions.

In present work, sol-gel auto-combustion method is used for synthesis of NiFe2O4 nanoparticles by using metal nitrates, citric acids and ammonia. The prepared samples are characterized by different techniques likes XRD, VSM, FTIR.

2. MATERIALS AND METHODS

2.1. Materials

All the reagents are of analytical grade and are used as received without further purification. Nickel nitrate [$Ni(NO_3)_2.6H_2O$], magnesium nitrate [$Mg(NO_3)_2{\cdot}6H_2O$**],**ferric nitrate [$Fe(NO_3)_3{\cdot}9H_2O$], Citric acid and Ammonia.

2.2. Methods

The 1M ferric nitrate, 1M nickel nitrate and 1M citric acids are prepared in separate beakers. The molar ratio of nitrate to citric acid is 1:1. Firstly added two nitrates and stirred for 5 minutes get homogeneous solution. After that add citric acid and again stirred. By using ammonia pH should be adjusted. Then prepared solution is heated so that is converted into sol. Continuous heating and stirring it transform into a xerogel. When ignited points observed the dried gel burnt by self combustion manner to form powder. The experimental details give with the help of flow chart in fig. 1.

ISSN 2394 - 9954

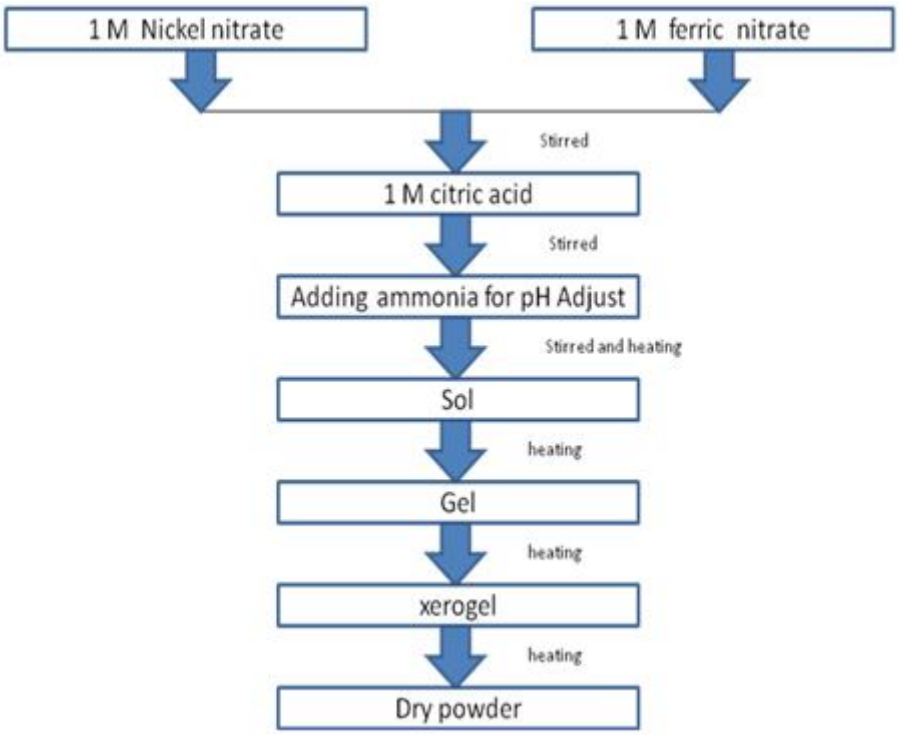

Fig-1: Flow chart of Synthesis of Nickel ferrite nanoparticles

3. RESULTS AND DISCUSSION

3.1. XRD

Nickel ferrite nanoparticles synthesized by sol-gel auto combustion method is characterized by X-ray diffraction pattern is as shown in fig.1. The mean crystallite size of the sample were estimated from most intense peak using sherrer's formula

$D=0.9\lambda/(\beta\cos\theta)$

Where λ is wavelength of X-ray.

From XRD graph analysis, calculate crystallite size full width half maxima and hkl plane. These XRD data agrees well with the standard JCPDS values with ref.code [01-074-2081].

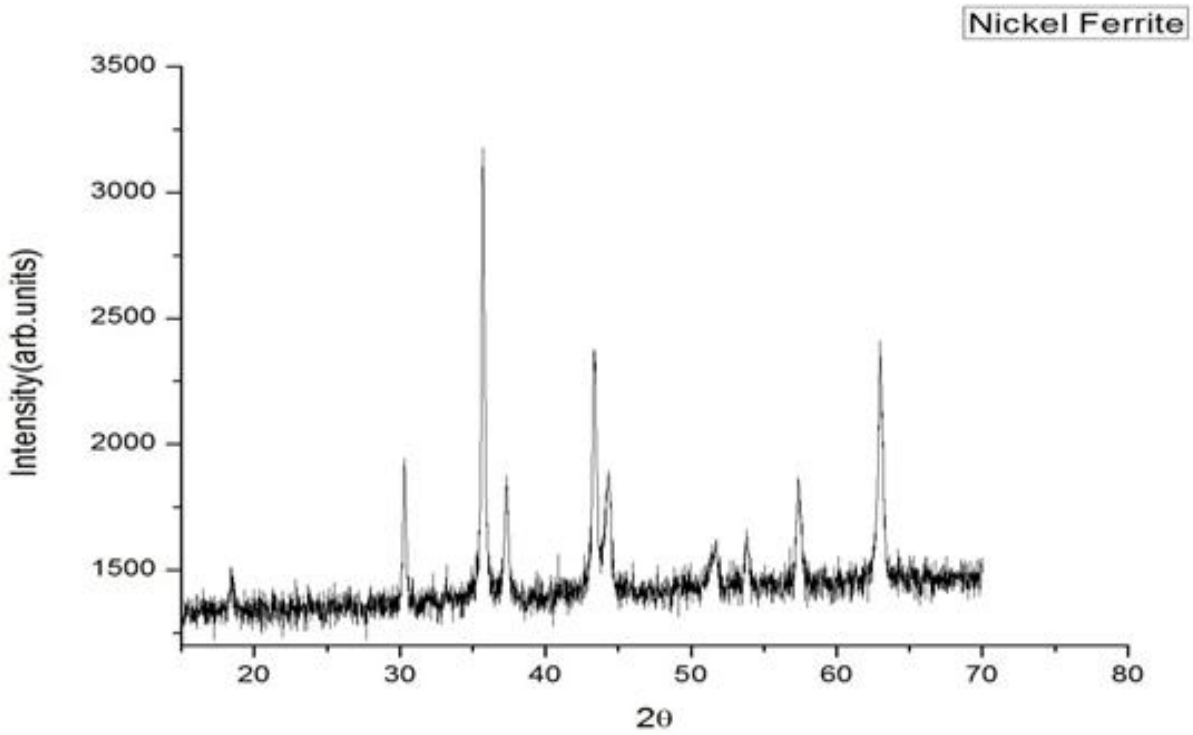

Fig-2: XRD pattern of Nickel ferrite nanoparticles by sol-gel auto combustion method.

ISSN 2394 - 9954

2θ	FWHM	d-Spacing[A°]	hkl	Crystallite size(nm)
30.3080	0.1574	2.9490	220	54.64
35.7079	0.1968	2.5145	311	**44.31**
37.2923	0.2362	2.4112	222	37.09
43.3657	0.2362	2.0866	400	37.82
53.8783	0.4723	1.7016	422	19.72
57.3828	0.3149	1.6058	511	30.05
62.9778	0.3360	1.4747	440	28.97

Table-1: XRD analysis

3.2. VSM

Magnetic measurements were carried out using a vibrating sample magnetometer. Fig. 2 shows the hysteresis loops of nickel ferrite nanoparticles. The saturation magnetization (Ms), remanent magnetization (Mr) and coercivity (Hc) are summarized in table 2.

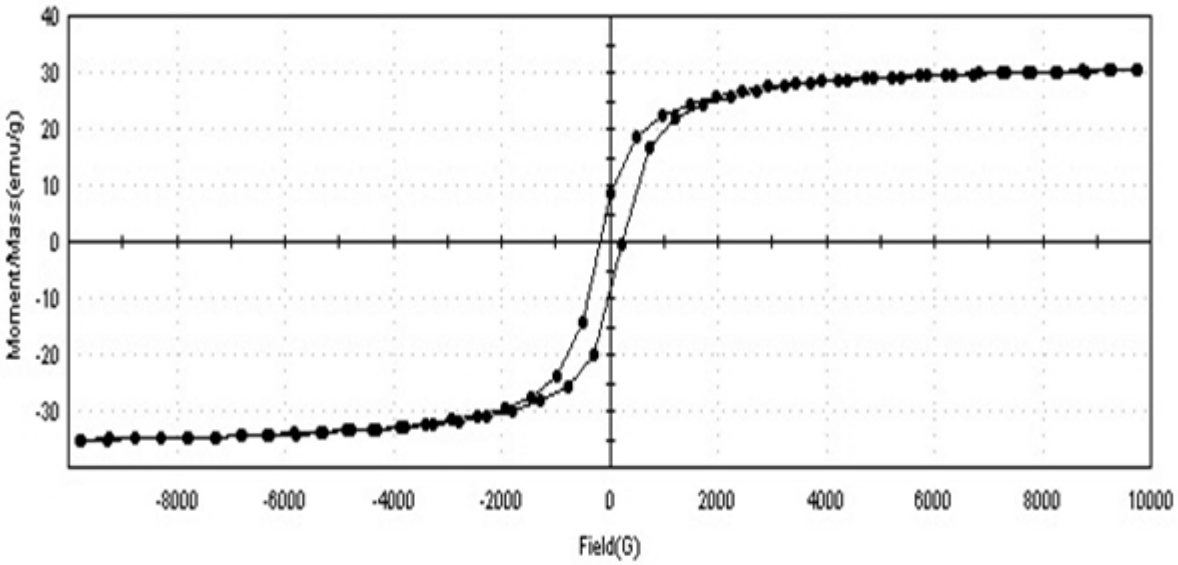

Fig-3: Hysteresis graph of Nickel ferrite magnetic nanoparticles.

Sample	Ms(emu/g)	Mr(emu/g)	Hc(G)
Nickel Ferrite	32.856	8.5136	200.59

Table-2: Values of Saturation magnetization, retentivity, coercivity.

3.3. FTIR

FTIR means Fourier transform infrared spectrometer. FTIR spectral analysis helps to confirm the formation of spinal structure of nickel ferrite nanoparticles. The wave number range from 600-3800 cm^{-1}. The one is observed in 650cm^{-1} is caused by the stretching vibrations of the tetrahedral metal oxygen bond. The bond near 1400cm-1 is due to antisymmetric NO starching vibrations arising from the nitrate group. This band is very weak in sol-gel derived sample which indicates the purity of nickel ferrite nanoparticles synthesized by sol gel method.

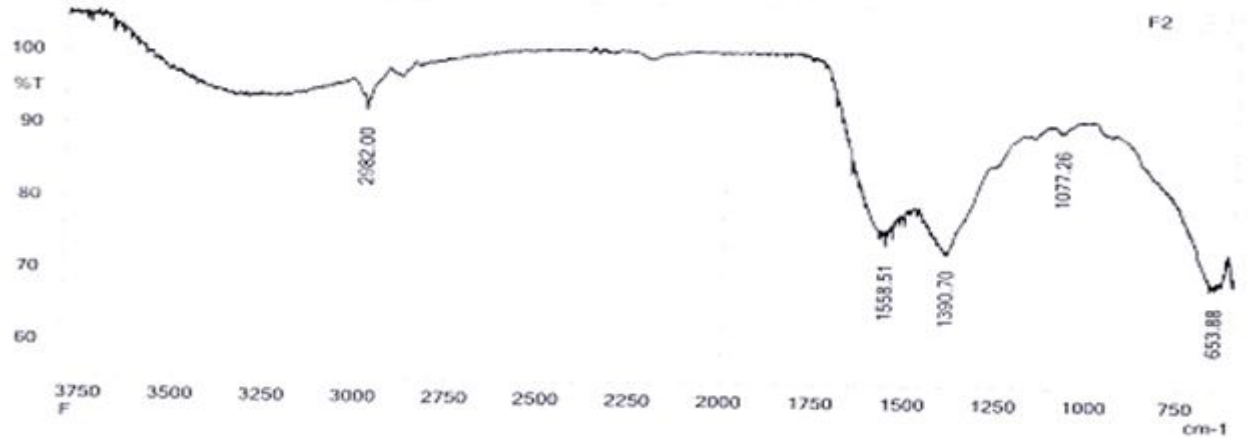

ISSN 2394 - 9954

4. CONCLUSION

Sol –gel auto combustion method is used for synthesis of nickel ferrite nanoparticles. This method produce single phase cubic nickel ferrite nanoparticles. Nickel ferrite nanoparticles having crystallite size varies from 19-55nm and having ferromagnetic nature. The nickel ferrite nanoparticles also exhibits hysteresis having saturation magnetization 32.856(emu/g), retentivity 8.5136(emu/g) and coercivity 200.59(G). FTIR confirms the stretching vibrations of metal oxygen bond and NO stretching vibrations.

REFERENCES

1. "Finite size effects on the structural and magnetic properties of sol–gel synthesized NiFe2O4 powders", Mathew George, Asha Mary John, Swapna S. Nair, P.A. Joy, M.R. Anantharaman , journal of magnetism and magnetic materials 302(2006) 190-195.
2. "Effect of preparation conditions on Nickel Zinc Ferrite nanoparticles: A comparison between sol–gel auto combustion and co-precipitation methods", Manju Kurian, Divya S. Nair.
3. X. Yi, Q. Yitai, L. Jing, C. Zuyao, Y. Li, Mater. Sci. Eng. B34 (1995), p. L1.
4. S. Komarneni, E. Fregeau, E. Breval, R. Roy, J. Am. Ceram. Soc. Commun. 71 (1988).
5. S. Prasad, N. S. Gajbhiye, J. Alloys Comp. 265 (1998), p. 87-92
6. X. Yi, Q. Yitai, L. Jing, C. Zuyao, Y. Li, Mater. Sci. Eng. B34 (1995), p. L1.
7. C. H. Marcilly, P. Country, B. Delmon, J. Am Ceram. Soc. 53 (1970), p. 56.
8. "Nickel ferrite: combustion synthesis, characterization and magnetic properties", A. C. F. M. Costa, L. Gama, C. O. Paiva-Santos, M. R. Morelli and R. H. G. A. Kiminami
9. "Influence of preparation method on structural and magnetic properties of nickel ferrite nanoparticles", Binup Jacob, Ashok kumar, R P Pant.

International Journal of Research in Science and Technology
Volume 6, Issue 1 : January - March, 2019
ISSN 2394 - 9954

A BRIEF REVIEW OF STUDIES OF SUBSTITUTED ABO_3 TYPE COMPOUNDS

R. J. Topare
Yogeshwari Mahavidyalaya, Ambajogai

ABSTRACT
The effect of substitution in the various ABO_3 type compounds by various researchers have been discussed. The substitution at both sites is studied by these researchers and they have got interesting results. These results are briefly illustrated in this article.

Keywords: BT & BIT compounds, BFO and PLZMST ceramics.

INTRODUCTION

Out of the various ABO_3 type materials, $BaTiO_3$ is the most widely used ferroelectric material. Over the years$BaTiO_3$ has been used in a wide variety of applications in various forms of crystal, bulk ceramics, multilayers and thin films. The ability to be used in so many different applications is a consequence of the complex coupling and the various interactions associated with ferroelectric phenomenon. The environment friendly lead free perovskite structured $BaTiO_3$based materials are one among low dielectric loss materialswhich have wide range of applications in the field of wireless communication and microwave devices [1-3].

Bismuth Sodium Titanate abbreviated as BNT is one of the important ferroelectrics with perovskite structure [4]. Moreover it is an A site substituted distorted perovskitecompound which is a rarer than the B site one. Although most investigations have been concentrated on the modification of BNT for applications such as piezoelectric and pyroelectric devices,this material is supposed to be the good candidate for high temperature relaxor.

This paper takes a review of the properties of these materials after substitution of different elements at different sites.

BT AND BIT COMPOUNDS

In recent years, modified Bismuth Titanate (BIT) structured materials have extensively been studied as a suitable candidate for non-volatile ferroelectric random access memory capacitors, lead free piezoelectric applications, electro-optic switching behaviour, optical displays because of its high Curie temperature and many more applications [5-8]. The $BaTiO_3$ (BT) is an insulator at room temperature major changes in its behaviour can be obtained by substitution studies it is an established fact adding fraction of a percent of acceptor impurities greatly increases the resistance near T_C[9] . A positive temperature coefficient of resistance (PTCR) is usually observed in BT ceramics doped with donor impurities such as covalent ions at A andB sites of perovskite compound.Maria Teresa Buscaglia et al [10] have reported atomistic stimulation of incorporation of the first series of transition metals and lanthanide series ions in BT compound.Due to transition element ions such as Mn, Fe, Cr etc, the PTCR effect is also observed insamples doped with donor impurities [11]. The need to compensate the excess charge state is accomplished by an increase in grain size and transfer of impurities from the inter-into integral space [12]. Doping with low concentration of donor impurities, leads to semiconducting ceramics, and showing PTCR behaviour.

Shivanand Madolappa et al [13]have studied the doping of Gadolinium(Gd) and Chromium (Cr) doping in BT compounds. They have prepared BT compounds by substituting Gd and Cr at the A site with solid state reaction technique. They have found that the structure is cubic, the lattice parameters and cell volume decreases with increase in the concentration of Cr. the dielectric study shows the nonlinear dielectric property change with different concentration of Cr. DC resistivity shows the lower PTCR behaviour. Thermoelectric measurement proved electrons has majority charge carriers and sample as an n-type semiconductor.The calculated tolerance factor values of the samples are given in table 1. The electrical data of the doped samples is given in table 2.

Nagbasavanna Sharanappa et al [14] studied Lanthanum (La) doped BIT ceramics by preparing the nano powder ceramics using solid state reaction method. They found that the crystal structure is not affected by lanthanum doping in BIT compounds. The Curie temperature was decreased with increase of La content, except x=0.30, which shows lattice distortion caused due to the difference of ionic radii of Bi and La. Thermal measurements show crystallization temperature of pure and La doped be BIT. Percentage weight loss is also negligible and synthesized samples are stable at higher temperatures. Anomalous dielectric behaviour as a function of temperature at various La compositions was illustrated by the synthesized samples. Change in DC conductivity of the samples show evidence of PTCR.

ISSN 2394 - 9954

Raghavendra Sagar et al [15] studied the dielectric and impedance studies of Ce doped $Ba(Zr_{0.52}Ti_{0.48})O_3$compound. Ce was doped at Ba site with X=0.1 and 0.2. The frequency dependent tan δstudy shows the nonlinear dielectric properties change with different concentration of Ce. Relative permittivity shows the moderate values in all studied temperature range. Impedance measurement proves excellent electrical behaviour of the samples.

PLZMST CERAMICS

Bismuth (Bi) and lanthanum (La) doped lead manganeseantimoinezirconate titanate (PZMST) ceramic powderhave been synthesized by high temperature solid state reaction method by Hayet Menasra et al [16]. They found that all the compounds where crystallized in pure pervoskite phase with the predominant tetragonal phase. The grain sizewas obtained in the order of 2.28 micrometre and uniform grain distribution wish is in accordance with the density. The increase in core temperature and dielectric constant can be attributed to the emerging lead vacancies creation by donor cations (Bi), and acceptor to reduce the oxygen vacancies mobility to balance charge in the modified PLZMST.Figure 1 shows the XRD patterns of PLBZMST ceramics.

BFO CERAMICS

Erbium (Er) and lanthanum (La) substituted $BiFeO_3$(BFO) ceramics have been prepared through solid state conventional route by Pragya Pandit et al [17]. They have reported decrease in T_C value with subsequent Er doping which indicates lowering of Curie temperature.It was observed that the magnetic properties of pure BFO have been improved by Er doping and weak ferromagnetism was observed with subsequent Er doping. Dielectric permittivity was constant at all frequencies and low dielectric loss was observed for all compositions. Proper ferroelectric hysteresis loop is obtained for BFO. The decrease in ferroelectric polarization was observed for Er doped samples due to the decrease in the stereochemical activity of the A-site ions. It implied thatEr doped samples exhibited improved magnetic and reasonable ferroelectric properties for low levels of doping.

ACKNOWLEDGEMENTS

The author would like to thank Yogeshwari education society for the encouragement in the research.

REFERENCES

[1] P.Petkov et al *J.Optoelectron and Adv.Mater*. 5(2),521-524 (2003)

[2] S.Sreekantan et al *J.Phy.Sci*. 20 (2) 13-22, (2009)

[3] H.Sreemoolandhana et al *J.Solid State Chem.* 177, 3995-4000 (2004)

[4] Smolenski et al (1961)

[5] Z.Z.Lazarevic et al *Sci.Sint.* 39,267-272 (2007)

[6] N.Pavlovic et al *Proc. And Appl. Ceram.*,3,88-95 (2009)

[7] T.Jardiel et al *J.Cera.Soc.Jap*.116,511-518 (2008)

[8] J.H.Park et al *J.Phys.D.Appl.Phys*.40,579-583 (2007)

[9] T.Miki et al *J.Appl.Phys.*,83,1592-1603 (1998)

[10] M.T. Buscaglia et al *J.Am.Ceram.Soc.* 84(2),376-384,(2001)

[11] S.Jida et al *J.Appl.Phys*.80,5234-5240 (1998)

[12] M.D.Glinchuk et al *Phys.Status.Solidi A*,22,341-346 (1990)

[13] Shivanand Madolappa et al *Ferroelectrics*,413,37-45 (2011)

[14] Nagbasavana Sharanappa et al *Ferroelectrics letters*, 39, 81-87 (2012)

[15] Raghavendra Sagar et al *Integrated ferooelectrics*, 130, 21-26 (2011)

[16] Hayet Menasra et al *Materials Sci and Appl.* 4, 293-298 (2013)

[17] Pragya Pandit et al *Bull.Mater.Sci*,34(4) 899-905 (2011)

ISSN 2394 - 9954

Table 1
Crystallographic data of Gd^{3+} and Cr^{3+} co-doped $BaTiO_3$ ceramics

Sample composition	Sample code	Tolerance factor (t)	Lattice parameter (a) Å	Cell volume $(Å)^3$	X-ray density (gm/cc)	Particle size (nm)
$Ba_{0.989}Gd_{0.001}Cr_{0.01}TiO_3$	SM11	0.93	4.0073	64.35	6.00	18.26
$Ba_{0.979}Gd_{0.001}Cr_{0.02}TiO_3$	SM12	0.93	4.0051	64.27	5.98	18.40
$Ba_{0.969}Gd_{0.001}Cr_{0.03}TiO_3$	SM13	0.93	4.0042	64.20	5.96	16.37
$Ba_{0.959}Gd_{0.001}Cr_{0.04}TiO_3$	SM14	0.92	4.0014	64.07	5.94	17.37
$Ba_{0.949}Gd_{0.001}Cr_{0.05}TiO_3$	SM15	0.92	4.0009	64.04	5.93	10.79

Table 2
Electrical data of Gd^{3+} and Cr^{3+}co-doped $BaTiO_3$ ceramics

Sample code	Curie Temperature T_c (K)	ε_{max}	ρ_{RT} (Ωm) × 10^7	ρ_{max} (Ωm) × 10^7	T_{max} (K)	ρ_{max}/ρ_{RT}
SM11	376	730.46	2.0	15.5	360	7.75
SM12	412	2020.86	2.75	4.24	360	1.54
SM13	408	1102.06	1.20	1.47	360	7.35
SM14	418	656.12	5.0	26	350	5.20
SM15	360	120	7.1	11	418	1.68

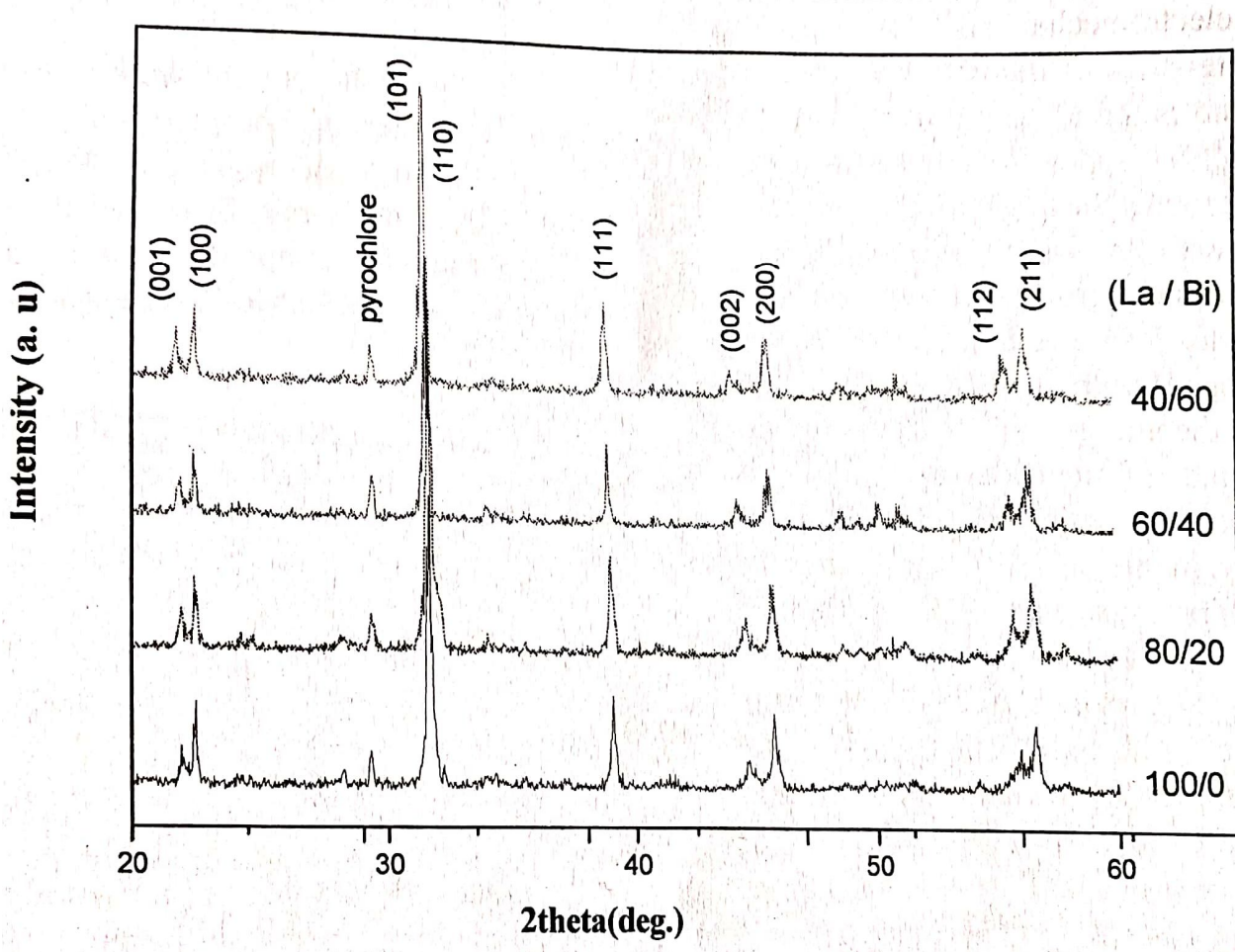

Figure 1. XRD patterns of PLBZMST sintered at 1180°C.

International Journal of Research in Science and Technology
Volume 6, Issue 1 : January - March, 2019
ISSN 2394 - 9954

SYNTHESIS, CRYSTALLOGRAPHIC AND MAGNETIC PROPERTIES OF NI DOPED MAGNESIUM FERRITE NANOPARTICLES

Mahesh B Shaha, Ravindra Kambale, Brijesh M Singh and Vaishal A Bambole
Department of Physics, University of Mumbai, Vidyanagari Campus Kalin, Mumbai

ABSTRACT
The present work focuses on the synthesis, structural, microstructural and magnetic studies of the nanocrystalline nickel doped magnesium ferrite ($Mg_{0.6}Ni_{0.4}Fe_2O_4$). The sample of $Mg_{0.6}Ni_{0.4}Fe_2O_4$ nanocrystalline spinel ferrite has been synthesized by sol-gel auto combustion method using citric acid ($C_6H_8O_7$) as a fuel, the prepared sample was sintered at 600 ˚C for 5 hrs. The structural properties were estimated from X-ray diffraction (XRD) studies. The microstructural studies were investigated through Field Emission Gun Scanning electron microscopy (FEG-SEM) technique. X-ray patterns confirmed the formation of single phase cubic structure. The magnetic properties were investigated by vibrating sample magnetometer. The crystallite size of synthesized ferrite nanoparticle is within the range of 10-35 nm. The saturation magnetization was27.43emu/g.

Keywords: Nanocrystalline, sol-gel, XRD, FEG- SEM.

INTRODUCTION
In recent years, spinel ferrites have been investigated for their useful magnetic properties and applications in information storage systems, sensors, actuators, magnetic fluids, microwave absorbers and medical diagnostics [1-5]. Thus much attention has been focused on the preparation and characterization of nanoparticles of spinel ferrites. For the applications of nanomaterials in various diverse fields [6, 7], it is necessary to be designed and exploited new materials of more predictable properties than what are currently available. Ni doped Magnesium ferrite ($Mg_{0.6}Ni_{0.4}Fe_2O_4$), owing to strong ferromagnetism and high Curie temperature, is used in electronic appliances since it stays magnetized even when the applied magnetic field is removed. This leads towards a useful way of information storage [8, 9].

Ni doped Mg-ferrite is an interesting material because of its high coercivity, moderate saturation magnetization, good chemical stability and mechanical hardness; therefore it can found applications in magnetic drug delivery and high density information storage [10-12].

The most widely used wet chemical method for the synthesis of spinel ferrites is the sol-gel auto combustion method. This method has several advantages over the other synthesis methods due to its low processing temperature, high chemical homogeneity, thermal stability of controlling the size and morphology of particles etc. [13-16].

The aim of the present work is to synthesize and study the structural, microstructural and magnetic properties of Ni doped magnesium ($Mg_{0.6}Ni_{0.4}Fe_2O_4$) ferrtie nanoparticles.

MATERIALS AND METHOD
The nanocrystalline samples of Ni doped magnesium ferrite ($Mg_{0.6}Ni_{0.4}Fe_2O_4$), were prepared using sol-gel auto combustion method. AR grade chemicals such magnesium nitrate ($Mg(NO_3)_2.6H_2O$), nickel nitrate($Ni(NO_3)_2 . 6H_2O$) ferric nitrate ($Fe(NO_3)_2 . 9H_2O$) and citric acid ($C_6H_8O_7$) were used for the synthesis. The metal nitrates to fuel (citric acid) ratio was taken as 1:3. Ammonia solution wasadded to maintain the pH 7. The temperature required for the synthesis of Ni doped Mg-ferrite nanoparticles was low that is around 110 ˚C. The as-synthesized powder is sintered at 600 ˚C for 5 hrs. and used for further investigations of structural properties. X-ray diffraction (XRD) technique was employed to characterize the prepared nanoparticles using REGAKU X-ray diffractometer. Morphology of the prepared samples was studied using Scanning electron microscope (SEM) JEOL-JSM 840 Model. Its morphology was studied with a field emission gun scanning electron microscope (FEG-SEM, model –JSM-7600F). The magnetic properties studied with vibrating sample magnetometer.

RESULTS AND DISCUSSION
The X-ray diffraction pattern of the $Mg_{0.6}Ni_{0.4}Fe_2O_4$ spinel ferrite nanoparticles is shown in Fig.1(a)The XRD pattern shows the reflections belonging to cubic spinel structure; no extra peaks have been observed in the XRD patterns. Rietveld refined powder X-ray diffraction patterns confirmed nanocrystalline single phase formation of all the ferrite samples in the face centered cubic spinel structure in the space group of Fd3m is shown in Fig. 1 (b).The intensity of (311) plane is more as compared to other planes like (220), (222), (400), (422), (511) and

ISSN 2394 - 9954

(440) and is chosen for the determination of crystallite size. The average crystallite size of the sample was calculated using Scherer's formula [9].

$$D = \frac{k\lambda}{\beta \cos\theta} \quad (1)$$

Where k is the grain shape factor (0.9) and λ, θ, and β are the X-ray wavelength, Bragg diffraction angle, and full-width at half-maximum of the diffraction peak respectively.

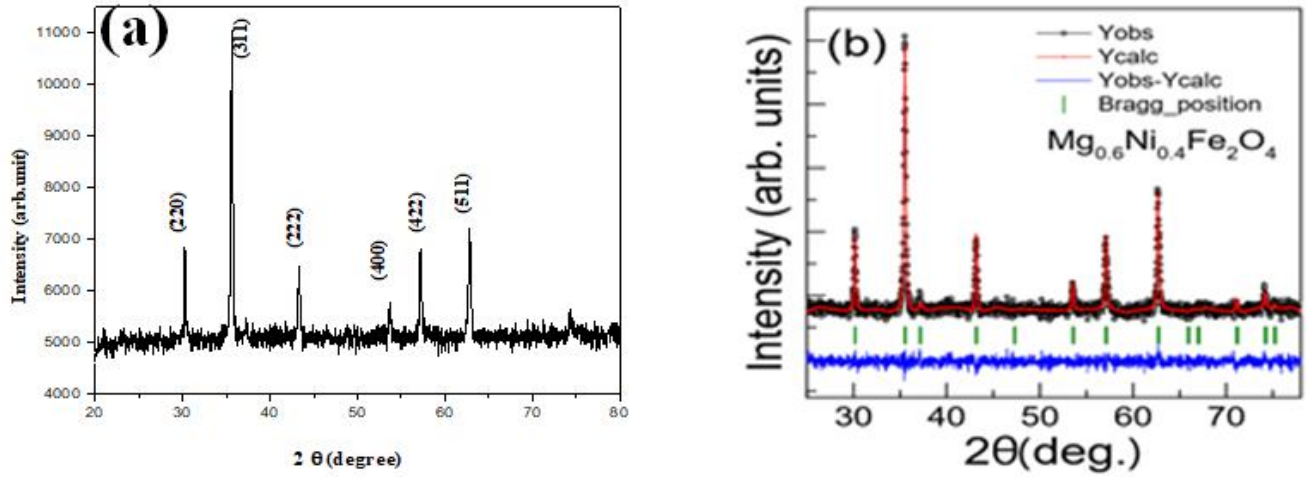

Fig-1(a) XRD pattern of $Mg_{0.6}Ni_{0.4}Fe_2O_4$(b) Rietveld refined powder X-ray diffraction patterns

The crystallite size of $Mg_{0.6}Ni_{0.4}Fe_2O_4$ ferrite nanoparticle s has been calculated using above equation and calculated average size to be 28 nm. The lattice constant, X-ray density, unit cell volume was calculated using XRD data and values are given in table 1.

Table-1: The Lattice constant, X-ray density, unit cell volume and Average particle size.

Sample	lattice constant (a)	X-ray density (d_x)	Unit cell volume (V)	Average particle size (t in nm)
$Mg_{0.6}Ni_{0.4}Fe_2O_4$	8.381	5.236	588.67	28

Fig.2 shows morphological pattern of the prepared Ni doped magnesium ferrite nanoparticles taken by Field emission gun scanning electron microscope (FEG-SEM). Evidently, from FEG-SEM image it was seen that the morphology of the particles were almost cubical in shape, but agglomerated to some extent due to the interaction between magnetic nanoparticles. The formation of nano size crystallites was confirmed through FEG-SEM image.

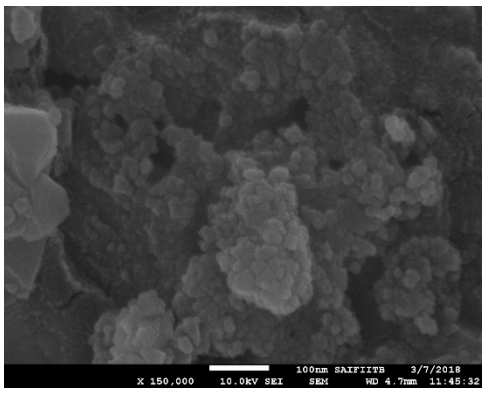

Fig-2: FEG- SEM image of $Mg_{0.6}Ni_{0.4}Fe_2O_4$ferrite nanoparticles

The magnetic properties of ferrites depend on the chemical composition and cation distributions in the octahedral and tetrahedral sites. Moreover, it was reported that coercivity of these materials depends on several factors such as size distribution, micro strain, anisotropy and temperature. The magnetic properties of the $Mg_{0.6}Ni_{0.4}Fe_2O_4$ferrite nanoparticles were analysed at room temperature by using a vibrating sample magnetometer (VSM) with an applied field -20 kOe ≤ H ≤ 20 kOe.

ISSN 2394 - 9954

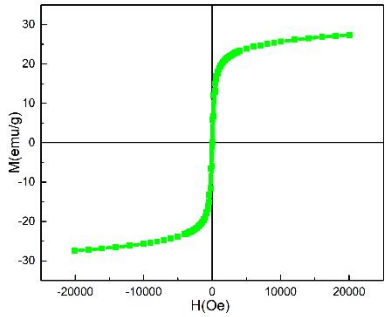

Fig-3: Magnetic hysteresis loops of $Mg_{0.6}Ni_{0.4}Fe_2O_4$nanoparticles

Fig.3 shows the magnetization (M) versus the applied magnetic field (H) for $Mg_{0.6}Ni_{0.4}Fe_2O_4$ferrite nanoparticles. The value of saturation magnetization (Ms), remnant magnetization (Mr) and coercivity (Hc) for $Mg_{0.6}Ni_{0.4}Fe_2O_4$ferrite nanoparticles were 27.43emu/g, 5.29emu/g and 91.28 Oe.

CONCLUSIONS

The nanocrystalline Ni doped magnesium ($Mg_{0.6}Ni_{0.4}Fe_2O_4$) ferrite successfully synthesized by sol-gel auto combustion technique. The XRD results showed the formation of single phase cubic spinel structure. The formation of nano size crystallites was confirmed through FEG-SEM image and the particle size of the sample was obtained to be 28 nm. The value of saturation magnetization (Ms) from vibrating sample magnetometer was obtained to be 27.43emu/g. This material is suitable for data storage device and microwave absorption.

REFERENCE

1. J.Roelofs, A.Van Dillen, Y. K. de Jong, Catal. Today 60 (2000) 297-303.
2. Jian Ming Gao, Zhi Kai Yan, Jing Liu, Mei Zhang, Min Guo, Material Letters, 141 (2015) 122- 124.
3. S.Murcia-Mascaros, R.Navarrao, L.Gomez-Sainero, U.Costantio, M. Nocchetti, J. L. G.Fierro., J. Catal. 198 (2001) 338-347.
4. J.F.Hochepied, M.P.Pileni, J. Appl. Phys. 87 (2000) 2472.
5. M.H.Khedr, A.A.Omar, M.I.Nasr, E.K.Sedeek, J. Anal. Appl. Pyroly. 76 (2006) 203.
6. S.G.Algude, S.M.Patange, S.E.Shirsath, D.R.Mane, K.M.Jadhav, J. Magn. Magn. Mater. 350 (2014) 39-41.
7. Nalla Somaiah, T.V.Jayaraman, P.A.Joy, Dibakar Das, J. Magn. Magn. Mater. 324:14 (2012) 2286-2291.
8. Elements of X-ray diffraction by B.D.Cullity, 1956 Addison-Wesley, publishing company, Inc.
9. H. Duan, F. Zhou, X. Cheng, G. Chen, Q. Li, J. Magn. Magn. Mater. 424 (2017) 467-471.
10. R. S. Alam, M. Moradi, M. Rostami, H. Nikmanesh, R. Moayedi, Y. Bai, J. Magn. Magn. Mater. 381 (2015) 1-9.
11. V.Rives, O.Prieto, A.Dubey, S.Kannan, J. Catal. 220 (2003) 161-167.
12. F.Prinetto, D.Tichit, R.Teissier, B.Coq, Catal. Today 55 (2000) 103-116.
13. Yu-jia Suna, Yi-fei Diaob, Hui-gang Wanga, Guangju Chena, Mei Zhanga, Min Guoa,Ceramic International, 43 (2017)16474-16481.
14. H. Moradmard, S. Farjam, Shayestel, P Tohidi, Z Abbas, M. Khaleghi , J alloys. Comp. 650 (2015) 116-122.
15. Pradeep chavan, L R Naik, Vacuum 152 (2018) 47- 49.
16. E Ateria, M A Ahmed, R M Ghouniem, Solid State Sci. 31 (2014) 99-106

International Journal of Research in Science and Technology
Volume 6, Issue 1 : January - March, 2019
ISSN 2394 - 9954

SYNTHESIS AND ACOUSTICAL CHARACTERISATION OF BINARY LIQUID SYSTEM AT TEMPERATURE 313.15 K

Sangita Shinde[1], Pallavi Nalle[2], B. R. Sharma[3] and K. M. Jadhav[4]
[1,3]Department of Physics, Pratishthan Mahavidyalay, Paithan, Aurangabad
[2]Department of Physics, Shivchhatrapati College, Aurangabad
[4]Department of Physics, Dr. Babasaheb Ambedkar Marathwada University, Aurangabad

ABSTRACT
The intermolecular interactions of urea and physical variants of solute-solvent have been studied by ultrasonic methods. At various concentrations the experimental values of Ultrasonic Velocity (u) and density (ρ) have been obtained for aqueous urea solution at a temperature 313.15 K and at 2MHz frequency. From experimental data the acoustical and temperature dependent parameters such as intermolecular free length (L_f), adiabatic compressibility (β) and specific acoustic impedance (Z) have been obtained. These thermodynamic parameters have been further utilized to predict the ion-ion and solute-solvent interaction in the binary mixtures. The results are interpreted in the light of structure making/breaking mechanisms of Urea- aqueous solution.

Keywords: Ultrasonic velocity, Density, Intermolecular free length, Adiabatic compressibility, Specific acoustic impedance.

INTRODUCTION
The ultrasonic techniques are widely employed and studied to determine Physico-chemical behavior of various liquid systems [1]. The main aim of several earlier researchers have been to study the molecular interactions between the components of pure, binary and ternary liquid solute and solvent using ultrasonic techniques and thermodynamic parameters [2]. Ultrasonic velocity studies in aqueous and nonaqueous electrolytic solutions led to new information in the salvation process. Depending on the charge density of electrolytes that evenly spread in water were classified as structure makers or breakers. Some researchers have reported that ions with low charge density are net dissociative structure breakers; ions with high charge density show net associative structure makers. In recent years, there are extensive study of thermodynamical properties of electrolytes in aqueous[3] or non-aqueous solutions but literature survey reveals that no work is done on aqueous urea as a temperature dependence[4] . The adiabatic compressibility, acoustic impedance and intermolecular free length of binary system of aqueous urea at various concentrations and at 313.15K temperature have been studied in the present paper.

MATERIALS AND METHODS
The purified AR grade sample of urea was used in fine solid powder as available. In the experimental part, all chemicals were utilized directly without any refinement/purification process. To prepare binary liquid mixture of (urea+water) system, the deionized and double glass distilled water was used. The specific conductivity of the deionized and glass distilled water was ~10^{-6} Siemens-$cm^{-1.}$ The binary mixture of (urea+water) having different concentrations (1%, 2%, 3%, 4%, 5%, 6%, 7%, 8%, 9% and 10% mole/lit) were prepared by using a Switzerland matter balance with a precision of 0.01 mg. The special air tight or sealed glassware were used for preparations and storage of solutions. These solutions were used within 12 hours to reduce bacterial adulterations.

ULTRASONIC VELOCITY MEASUREMENTS
The Ultrasonic velocity measurements were carried out using F-81 model for crystal interferometer operating at 2MHz frequency, supplied by Mittal Enterprises, Ltd. New Delhi. The ultrasonic interferometer was calibrated by using standard double glass-distilled water at 298.15K. The present crosschecked experimental value is 1497.08ms^{-1} which is in well agreement with reported literature value (1496.69 ms^{-1}) [5].

DENSITY MEASUREMENTS
The Density Measurements were performed with the help of a specific gravity bottles of 25 ml. Measurements of density were carried out by an accuracy of ±2x10^{-2} kg m^{-3}. To minimize error in measurements average of ten measurements are considered. Accuracy in experimental temperature was maintained at ±0.1K by means of thermostatic water bath.

THEORETICAL ASPECTS AND CALCULATIONS
From the experimental values of the ultrasonic velocity(u) and density(ρ) the various acoustical parameters such as the adiabatic compressibility(β), acoustic impedance(z) and intermolecular free length(Lf) were calculated by using the empirical Jacobson's relations[6,12] which are as follows:

ISSN 2394 - 9954

Ultrasonic velocity: $\mathbf{u = n \times \lambda}$ ---------- **(1)**

Adiabatic compressibility: $\mathbf{\beta = [1/u^2]x\rho}$ ---------- **(2)**

Specific Acoustic impedance: $\mathbf{Z = u \times \rho}$ ---------- **(3)**

Intermolecular free length: $\mathbf{L_f = [K/u] \times \rho^{1/2}}$ ----------**(4)**

Where K is temperature dependent constant called as Jacobson's constant. The values of K is taken as 306×10^{-8} at 313.15K. T is the absolute temperature, ρ and u are the density and ultrasonic velocity of binary solution.

RESULTS AND DISCUSSION

The experimental data of ultrasonic velocity (u) and density(ρ) of the binary solutions as well as calculated thermodynamical-acostical parameters specified as adiabatic compressibility (β), acoustic impedance (z) and intermolecular free length(L_f) are reported in Table.1 for the binary liquid mixture systems (water+urea).

1. Ultrasonic Velocity (u)

By using F-81 model of ultrasonic interferometer operating at 2 MHz Ultrasonic velocity of (water+urea) has been measured. The ultrasonic velocity variation study of urea at various concentrations and at 313.15K temperatures in solvent of water shows the variations to be non-linear. This indicates that there is strong interaction in the (water+urea) systems Adiabatic compressibility (β) is influenced by experimental data of ultrasonic velocity and the density (ρ). The changes in ultrasonic velocity of a urea in water as a function of concentration can be expressed in terms of adiabatic compressibility and density by eq. (5).

$du/dc = u/2 \times 1/d \times d\rho/dc + 1/\beta \times d\beta/dc$ ---------- (5)

The sign and magnitude of quantity dρ/dc and dβ/dc indicate that H-bonded structure of H_2O is disrupted by increasing concentration of urea in water. Consequently, a variation of ultrasonic velocity of system depends on the structural properties of the solutes of binary liquid [7]. The increasing variation in ultrasonic velocity of given solute in liquid system was structure maker . In (water+urea) binary system the behavior of ultrasonic velocity was directly proportional to concentration. This is due to maximum possible association in aqueous urea solution because of the presence of OH-groups. The urea occupies the interstitial space of water and tends to break the original ordered state of water due to its self-association. But at temperature 313.15K, there occurs structural rearrangement as a result of hydration [8] leading to a comparatively more ordered state as shown in Fig.1.

2. Density (ρ)

Density of (water+urea) binary system was determined at various concentrations at temperature 313.15K, is as shown in Fig.2. Density in general, depends upon ion-solvent and solvent-solvent interactions. As expected for given composition density increases as concentration of urea increases in binary mixture of (water+urea). Due to increase in concentration of urea, number of ion particles also increases that leads to increase in electrostriction, thereby decreasing effective volume of the mixture and effective density increases [9]. This shows that there is dipole-dipole interaction between binary liquid mixture systems.

3. Adiabatic Compressibility (β)

The adiabatic compressibility (β) is a measure of intermolecular bond enhancement or formation of bond fragments. In (water+urea) binary system adiabatic compressibility (β) decreases with increase in conc. of urea in water. Due to decrease in amount of water molecules which are replaced by urea molecules, thereby resulting in net decrease in compressibility. It is well known fact that enhanced electrostriction leads to net decrease in the compressibility of the solution, resulting in Hydrophilic [10] solutes having negative compressibility as well. Also due to ordering of the molecules of water-urea is induced by them in water structure. In the present study dβ/dc is negative which strongly indicates the presence of electrostriction effect of water molecules as shown in Fig.3.

4. Acoustic Impedance (z)

In (water+urea) binary liquid mixture system, it is noticed that the values of acoustic impedance (Z)varies with increase in solute concentration at 313.15K temperature. As shown in Fig.4, the curve exhibits exactly reverse variation compared to adiabatic compressibility (β). Because adiabatic compressibility and acoustic impedance are inversely related to each other [11]. That indicates strong presence of molecular interaction in the system. It also indicates the presence of bond enhancements between solute-solute, solute-solvent and vice-a-versa in the present binary system.

ISSN 2394 - 9954

5. Intermolecular free Length (L_f)

The change in ultrasonic velocity depends on the intermolecular free length (L_f) of a mixture. The intermolecular free length (L_f) is a predominant factor in finding the variants of ultrasonic velocity in the fluids and their solution. In (water+urea) binary system intermolecular free length decreases with conc. of solute at 313.15K temperature as shown in Fig.5. This behavior indicates significant interaction exist between the solute-solvent, solvent-solvent structures promoting behavior.

CONCLUSION

Ultrasonic velocity and density have been measured for (water+urea) binary system at temperature 313.15K as a dependent variable of concentration. The variation in ultrasonic velocity(u), density(ρ) and other related thermodynamic variables viz. adiabatic compressibility, acoustic impedance and intermolecular free length for (water+urea) binary system at temperature 313.15K and as a dependent variable of concentration shows the behavior to be non-linear. Consequently, ultrasonic velocity of system increases with the enhancement of structural modifications of solute properties. It is fairly considered that solutes causing electrostriction modifications that lead to decrease in the compressibility of the mixture solution. The water liking solutes (Hydrophilic) often show negative compressibility. Thereby leading to structural enhancement in solute that supports the hypothesis that ultrasonic velocity parameter is structure maker. The non-linearity behavior confirms presence of strong possibilities of formation of clusters of hetero-molecular interactions. This provides useful information about inter and intra molecular interactions of the mixture as existing in the liquid system.

Table-1: Ultrasonic velocity (U), density (ρ) ,adiabatic compressibility (β), intermolecular free length (L_f), specific acoustic impedance (Z), for (water+urea) BINARY LIQUID MIXTURE solution at 313.15K

Conc. % (mole/lit)	u (m/s)	ρ ($*10^3$kg/m^3)	β (10^{-10} m^2/s)	Z ($* 10^{-6}$ Kg/m^2 s)	L_f ($* 10^{-6}$ m)
1	1552	1.0231	4.058	1.5878	0.1293
2	1560.93	1.0308	3.982	1.609	0.1281
3	1561.33	1.0329	3.971	1.6127	0.1279
4	1562.66	1.0356	3.954	1.6182	0.1277
5	1565.2	1.0553	3.868	1.6517	0.1263
6	1570.66	1.0622	3.816	1.6683	0.1254
7	1583.33	1.075	3.711	1.702	0.1237
8	1596	1.0941	3.588	1.7461	0.1216
9	1658.13	1.0996	3.308	1.8232	0.1168
10	1635.06	1.1015	3.236	1.845	0.1155

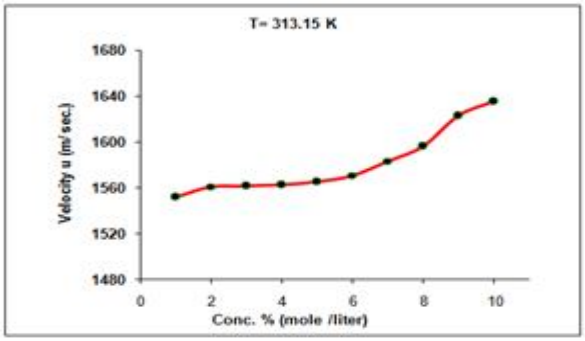

Fig-1: Plot of Variation of ultrasonic velocity (u)

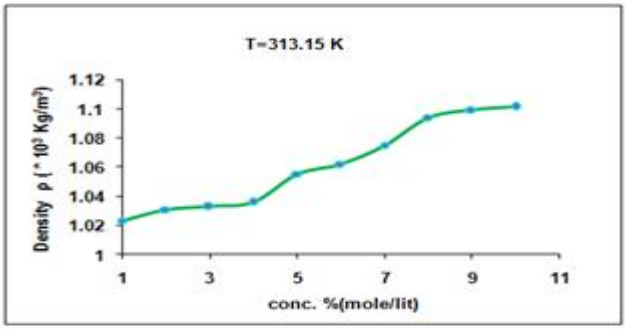

Fig-2: Plot of Variation of density with conc with conc..for urea + water system at 313.15K for (water+urea) system at 313.15K

ISSN 2394 - 9954

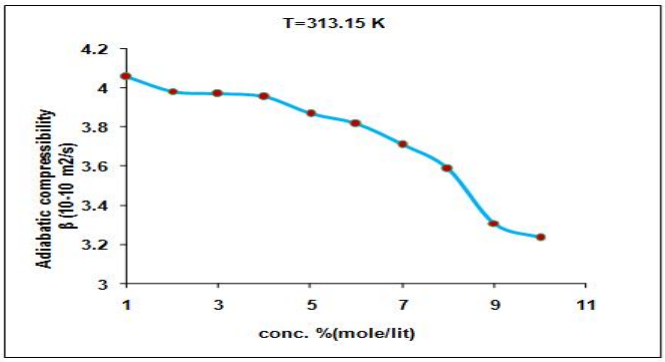

Fig-3: Plot of Variation of adiabatic comp (β)

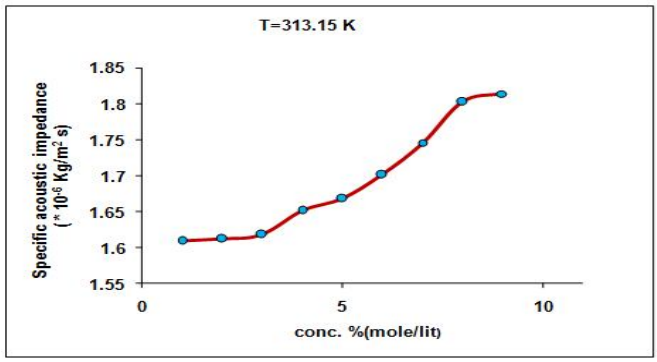

Fig-4: Plot of Variation of acoustic impedance with Conc .for(water+urea) system at 313.15K . with conc.for (water+urea) system at 313.15K

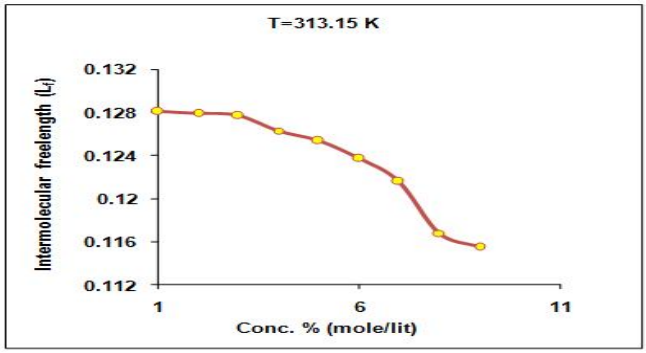

Fig-5: Plot of Variation of intermolecular free length with conc.for (water+urea) system at 313.15K.

REFERENCES

[1] Chiappe C. and Rajamani S. (2011),*Structural effects on the physico chemical and catalytic properties of acidic ionic liquids:* An Overview, Eur. J. Org. Chem. 5517-5539.

[2] Gracie K., Hawrylak B., and Palepu R(1998).,*Ultrasonic velocity and volumetric properties of isomeric butanediols plus water systems,* Can. J. Chem. 76pg 464-468..

[3] Schulick, P. (1994), *Ginger-common spice and wonder drug*. Edn 2. Herbal Free Press Ltd. Brattleboro Vermont USA.

[4] A. G. Shankarwer , B.H. Jahagirdar, B.R. Arbad, and Smt C. S. Patil (2000), Indian J Pure & Appl Phys, 38pp645.

[5] R.G. Charke, L. Hnedkovsky, P.R. Termaine & V. Majer, (2000) J Phys Chem, 104 B 11781..

[6] Ali, B. H., Blunden, G., Tanira, M. O., Nemmar, A. (2007). *Some phytochemical, pharmacological and toxicological properties of ginger Zingiber officinalis Roscoe: a review of recent research*: Food Chem Tox

[7] Jamankar, G., M,. and Deshpande, M., S., (2015):*Ultrasonic studies of molecular interaction of gallic acid with ethanol:* Pelagia Research Library Der Chemica Sinica.

ISSN 2394 - 9954

[8] Aswale, S., S., Aswale, S., R., Hajare, R., S: (2012). Adiabatic compressibility, intermolecular free length and acoustic relaxation time of aqueous antibiotic cefotaxime sodium: Journal of Chemical and Pharmaceutical Research.

[9] Baluja, Sh., Solanki, A., Kachhadia, N., (2007): *An Ultrasonic Study of Some Drugs in Solutions:* Russian Journal of Physical Chemistry A.

[10] Aswale S., S., Aswale S., R., Dhote A., B., , (2013). Adiabatic compressibility, free length and acoustic impedance of aqueous solution of paracetamol : Journal of Natural Sciences.

[11] Ramteke, S. P., Chimankar, O. P., Mandal, R. A., Tabhane, V. A., (2015). *Investigation of Acoustical Behavior of Dichlofenac sodium drug in Ethanol at Different Temperature*: International Journal of Science and Research.

[12] Sangita Shinde(2014).*International Jornal of Science and research , Volume 3 Issue 11, November*

International Journal of Research in Science and Technology
Volume 6, Issue 1 : January - March, 2019
ISSN 2394 - 9954

THE TREATMENT OF SKIN DISEASES WITH ULTRAVIOLET LIGHT

S. S. Arsad
M F M, Warud, Amravati

ABSTRACT
The phototherapy is being used for treatment of many skin diseases like psoriasis, hair removal, tattoo removal, skin resurfacing, vitiligo etc.The utility of UV radiation in the treatment of skin diseases is proven by various systematic studies on case to case basis. Phototherapy has undergone multifaceted improvements over few decades. While conventional phototherapy was based on body part exposure to UV radiation which included both affected and unaffected areas, targeted phototherapy using optic fiber cable and laser or nonlaser light with few mJ energy dose and spot size ranging from 1cm to 4 cm. In recent years, the research in the targeted phototherapy made availability of radiation with specific wavelength and intensity in portable models. Phototherapy is being used for effective treatment of about 20 dermatological problems[1]. It is found that Lasers with 337.1 nm are also useful for many of these diseases.

INTRODUCTION
Conventional phototherapy used Ultraviolet spectrum (200nm-400nm) for the treatment of dermatological problems. It included Broadband UVB Therapy, UVA therapy, Selective phototherapy (310-318 nm), Narrowband UVB (311 nm) therapy, Ultraviolet A1 (UVA1) and Ultraviolet A2 (UVA2) therapy. Conventional phototherapy is based on the use of tube light having radiation of desired wavelength.

In recent years, Targeted phototherapy in which Excimer laser were used are replaced by excimer lamps. , Intense pulse light therapy, Light-based targeted phototherapy, Photodynamic therapy Low-level laser and light-emitting diode therapy are the new terminology used in phototherapy. All these devices have the source of radiation designed with the aim of improved wavelength and energy standards. These are smaller in size and their spot size is reduced with Controlled energy dose.

METHOD
Coventinoal phototherapy have the main disadvantage of exposure of unaffected areas to UV light. In this method the treatment continues for long session with step by step increment in doses. The devices used are not handy so patient has to visit the clinic for long period. Certain body parts cannot be treated due to risk involved. Especially children patients do not cope with such type of treatment.

Targeted phototherapy is emerging as a more effective treatment tool for various dermatological problems but it has some drawbacks. Since the spot size is reduced to few cm the treatment of large affected areas become difficult. If the affected skin area is above 10% of the body then the targeted phototherapy is not recommended due to cost and time required for satisfactory results.

Along with these phototherapy modalities the use of topical or systemic agents was also tested which is refered as combination therapy.

COMBINATION THERAPY
Phototherapy may be combined with topical or systemic agents to achieve higher clearance rates, longer disease free intervals and a lower carcinogenic risk.8 Topical agents include anthralim,vitamin D analogues, retinoids, glucocorticoids, emollients, saltwater baths and tar. The combination of either broad band UVB or 311 nm UVB therapy with calcipotriol increases the therapeutic efficacy of phototherapy and reduces the irritation caused by calcipotriol.[9]

In psoriasis tazarotene gel applied topically along with narrowband or braodband UVB which promotes fast and effective cleaning of the disease.[10] This combination therapy can be initiated at lower doses than usual when used in combination with tazarotene.[11]

LASER THERAPY
The Excimer laser power and exposure time were so adjusted that the number of photons in both the cases were same. Final evaluation was done after every one month of the treatment. The patches exposed to UVB radiation i.e. Excimer laser radiation clearly showed pigmentation. No serious or adverse side effects were observed.

UVA radiation phototherapy and 337.1 nm pulsed nitrogen laser [12] were targeted to affected lesions only. The use of laser in the treatment limits the total skin exposure to UV radiation and hence the risk of skin cancer may also be reduced. It also brings faster therapeutic effect and the total treatment time also reduced after getting

ISSN 2394 - 9954

more experience. It limits the cumulative exposure to the UV radiation as compared to the conventional phototherapy. Thus we conclude that nitrogen laser can be used as a major pigmentary tool in all types of vitiligo treatment.[13] It is helpful in preventing further spread of vitiligo patches. Decrease of depigmentation versus time found to be exponential in behavior. These studies were carried out at the university lab.

CONCLUSION

The phototherapy is playing vital role in the treatment of dermatological disorders from ancient times. The modalities of treatment include variety of research. The use of small portion of light spectrum had been found of great importance for curing a number of diseases related to skin. In coming years new research in this field with analytical and statistical data of patients may come out with remarkable success against the fight with skin diseases.

Conventional Unit **Targeted Unit**

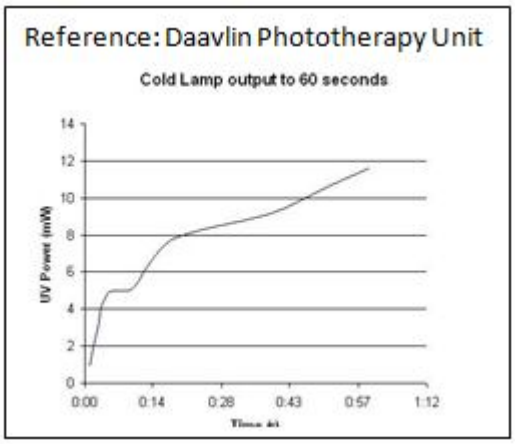

REFERENCES

1. Reena Rai, CR Shrinivas Phototherapy: An Indian Perceptive In J Dermatol 2007:52(4) 169-75
2. Mysore V. Targeted phototherapy Indian J Dermatol Venereol Leprol 2009; 75:119-25
3. Diffey BL. Ultraviolet phototherapy of skin diseases Physics and Engineering in medicine in the New Millenium IPEM:2000 p. 65-7.
4. Spencer JM, Hadi SM. The Excimer Laser. J Drugs Dermatol 2004: 3 : 522-5
5. Lapidoth M. Adatto M. David M. Targeted UVB Phototherapy for psoriasis A preliminary study. Clin Exp Dermatol 2007;23:32-4
6. Hadi S Tinio P Al-Ghaithi K et al Treatment of vitiligo using the 308 nm excimer laser. Photomed laser surg 2006:24:354-7
7. Balasaraswathi,P, Udaya Kumar, Shrinivas CR UVA and UVB radiations in sunlight Indian J Dermatol Venereol Leprol 2002 :68:198-201
8. Mentener MA, See JA, Amend WJ, Ellis CN et al Proceeding of the psoriasis combination and rotation therapy. J Am Acad Dermatol 1996; 34: 315-21.
9. Kerscher M, Volkanandt M, Plewig G, Lehmann P. Combination phototherapy of psoriasis with calcipotriol and narrow band UVB. Lancet 1993; 342:923
10. Koo JY, Lowe NJ, Lew-Kaya DA, Vasilopoulos AI, Luc JC, Sefton J, et al. Tazarotene plus UVB therpay in the treatment of psoriasis. J Am Acad Dermatol 2000;43:821-8
11. Hecker D, Worsley J, Yuch G, Kuroda K, Lebwohl M. Interactions between tazarotene and ultraviolet light. J Am Acad Dermatol 1999;41:927-30.
12. B.H. Pawar, S.S. Arsad *et al* Study of photo therapy with pulsed UV Nitrogen Laser for repigmentation in segmental type vitiligo, NLS-6, 2006, A-B, pp86.
13. B.H. Pawar, S.S. Arsad *et al* Comparitive study of photochemotherapy for repigmentation in vitiligo. NCOL 2007,Abstract, pp-71

International Journal of Research in Science and Technology
Volume 6, Issue 1 : January - March, 2019
ISSN 2394 - 9954

STUDY OF SEGMENTAL VITILIGO AND ITS TREATMENT WITH NBUVB FOR BETTER RESULTS

S. S. Arsad and U. R. Kathale
Department of Physics, M. F. M. Warud, Amravati

ABSTRACT
The vitiligo is a commonly found skin disorder in which the skin color is lost and white macules are visible.It is due to lack of melanin formation activity. The melanin decides color of the skin The vitiligo is classified by the appearance of patches, its pattern, areas affected by it and size.Oneof the sub types of vitiligo is segmental vitiligo. The purpose of treatment is to regain original skin color at the sites which are white. The vitiligo is treated by various methods like phototherapy, herbal medicine therapy, allopathic medicines and homeopathic treatment is also one of the options for patient .The present paper is based on study of segmental vitiligo and its treatment with NBUVB.

BACKGROUND
Segmental vitiligo is a small but unique subset of vitiligo requiring due importance due to its lack of response to medical treatment but excellent response to surgical treatment. Characterization of the pattern of segmental vitiligo will also help to understand the pathogenesis of the disease.[1].Its possible to treat it with phototherapy in better manner.

Aim: To study the role of NBUVB in the treatment of segmental vitiligo.

INTRODUCTION
Vitiligo is an acquired pigmentary disorder of the skin presenting as depigmented or hypopigmented macules. It affects 0.1-2% population worldwide, [2],[3] and its prevalence in India is about 0.5-2.5%. [4],[5] Vitiligo can be classified into segmental and non-segmental vitiligo. Segmental vitiligo has depigmented macules arranged in a dermatomal or quasi-dermatomal distribution, which does not cross the midline. It differs from non-segmental vitiligo in terms of clinical features, natural history, and also treatment response. [6] Segmental vitiligo usually has an early onset in childhood in contrast to non-segmental vitiligo, which predominantly affects adults. In segmental vitiligo, the lesions develop rapidly over short span of time in a localized area and then remain stable, whereas non-segmental vitiligo has a highly variable course with periods of progression, remission, and stability. [6] Segmental vitiligo responds poorly to medical treatment, [7],[8] and surgical methods are the treatment of choice. [7] The characteristic feature of segmental vitiligo is the distribution pattern of the lesions. In most cases, it is fairly easy to recognize segmental vitiligo due to its unilateral and patterned distribution.In a study on 450 patients of vitiligo at AIIMS, New Delhi, segmental vitiligo was seen in 6.7% cases. An additional 1.7% had lesions of segmental vitiligo along with other types of vitiligo (mixed vitiligo). [10] Previous reports have described certain clinical features of segmental vitiligo. It is a disease of childhood; the incidence of segmental vitiligo is significantly more in children (19%) as compared to adults (5%). [11] The mean age of onset reported previously was 15.6 years, [12]. The disease stabilizes by 6 months to 1 year irrespective of treatment and disease progression halts faster than non-segmental vitiligo. [12],[13] This 'self-limiting' nature of the disease reduces the requirement of aggressive systemic therapy at the onset of the disease. Koga and Tango have described type A and type B vitiligo as non-segmental and segmental, respectively, and they noted progression from type B (segmental) to type A (non-segmental) vitiligo in 2.2% (3/134 patients). [5] In a case series of 127 patients with segmental vitiligo, Ezzedine et al found that 26 (20.4%) progressed from segmental vitiligo to non-segmental vitiligo. [14] In this study, progression from segmental vitiligo to another type of vitiligo was seen in only 10% patients and most developed focal vitiligo. Hence, a patient can be counseled that it is less likely that his disease will spread to other parts of the body, thus reducing psychological burden.The pattern of the lesions is what characterizes segmental vitiligo, yet there is no consensus regarding it. Dermatomal pattern has been mentioned most commonly [6],[12],[15] and is given in the definition of segmental vitiligo in many reputed dermatology books.

METHODS
In this particular study, the NBUVB phototherapy unit from Daavlin company was used. It was found that lesser number of exposures were required to achieve 25-75% repigmentation. Similarly, the cumulative dose was also lesser to achieve the same repigmentation, whereas Njoo et al. [21] reported the same repigmentation with more number of exposures (76.3 ± 16.7). The same observations were reported in other western studies. [18],[20],[23],[26],[27] Our study and other Indian studies [19],[23],[24] showed that dark skin (Fitzpatrick type IV and V) requires lesser number of exposures and cumulative dose to achieve 25-75% repigmentation when compared with white skin (Fitzpatrick I and II). It has also been observed in our study that

ISSN 2394 - 9954

with good adherence to therapy and compliance, faster and good response can be achieved. It has been proved statistically that good response is directly associated with more number of exposures, cumulative dose and good compliance.The body surface area involvement varied from less than 1% to 8%. In 121 (64.3%) patients, it was 1% or less. The remaining 67 patients had more than 1% body surface area involvement, the maximum being 8%. Leucotrichia [Figure 6] was present in 162 (86.1%) patients. There was no leucotrichia in 12 and no hair in the affected area in 14 patients. All the hair in the lesion were white in 70 patients while there were both white and black hair in the lesion in 92 patients. Normally pigmented skin beyond the margin of segmental vitiligo also showed leucotrichia in 122 (64.8%) patients .The adverse effects in our study were minimal and none of the patients required discontinuation of therapy. The adverse effect profile observed in our study was similar to that reported in the literature. [16],[17],[18],[19],[20] , [23],[27] All these studies, including ours, clearly establish the safety profile of NBUVB therapy. During the follow-up period of 6 months, of the 150 patients, only three patients developed depigmentation of repigmented sites. However, long-term follow-up is needed to observe stability of repigmentation.

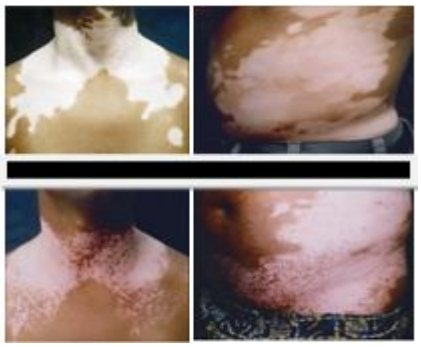

CONCLUSION

NBUVB is useful in the treatment of segmental vitiligo.Early recognition of segmental vitiligo can help to reassure the patient that it usually does not spread to other parts of the body, stabilizes early, and responds very well to phototherapy with probably a lower risk of recurrence.

REFERENCES

1. Khaitan BK, Kathuria S, Ramam M. A descriptive study to characterize segmental vitiligo. Indian J Dermatol Venereol Leprol 2012;78:715-21
2. Lerner AB. Vitiligo. J Invest Dermatol 1959;32:285-310.
3. Halder RM, Taliaferro SJ. Vitiligo. In: Wolff K, Goldsmith LA, Katz SI, Gilchrest BA, Paller AS, Lefell DJ, editors. Fitzpatrick's Dermatology in General Medicine, 7 th ed. New York: McGraw-Hill; 2008. p. 836-81.
4. Handa S, Dogra S. Epidemiology of childhood vitiligo: A study of 625 patients from North India. Pediatr Dermatol 2003;20:207-10.
5. Das SK, Majumdar PP, Chakraborty R, Majumdar TK, Haldar B, Rao CD. Studies on vitiligo I. Epidemiological profile in Calcutta, India. Genet Epid 1985;2:71-8.
6. Koga M, Tango T. Clinical features and course of type A and type B vitiligo. Br J Dermatol 1988;118:223-8.
7. Hann SK. Clinical features of segmental Vitiligo. In: Hann SK, Nordlund JJ, editors. Vitiligo, 1 st ed. UK: Blackwell Science; 2000. p. 49-60.
8. Kathuria S, Khaitan BK, Ramam M, Sharma VK. Segmental vitiligo: A randomized controlled trial to evaluate efficacy and safety of 0.1% tacrolimus ointment vs 0.05% fluticasone propionate cream. Indian J Dermatol Venereol Leprol 2012;78:68-73.
9. Handa S, Pandhi R, Kaur I. Vitiligo: A retrospective comparative analysis of treatment modalities in 500 patients. J Dermatol 2001;28:461-6.
10. Khaitan BK, Pasricha JS, Sood A. clinical profile of 450 Indian vitiligo patients. American Academy of Dermatology 61 st annual meeting 2003. San Francisco.
11. Halder RM, Grimes PE, Cowan CA, Enterline JA, Chakrabarti SG, Kenney JA. Childhood vitiligo. J Am Acad Dermatol 1987;16:948- 54.

ISSN 2394 - 9954

12. Hann SK, Lee HJ. Segmental vitiligo: Clinical findings in 208 patients. J Am Acad Dermatol 1996;35:671-4.
13. Mazereeuw-Hautier J, Bezio S, Mahe E, Bodemer C, Eschard C, Viseux V, et al. Segmental and nonsegmental childhood vitiligo has distinct clinical characteristics: A prospective observational study. J Am Acad Dermatol 2010;62:945-9.
14. Ezzedine K, Diallo A, Léauté-Labrèze C, Séneschal J, Prey S, Ballanger F, et al. Halo naevi and leukotrichia are strong predictors of the passage to mixed vitiligo in a subgroup of segmental vitiligo. Br J Dermatol 2012;166:39-44.
15. Taïeb A, Picardo M; VETF Members. The definition and assessment of vitiligo: A consensus report of the Vitiligo European Task Force. Pigment Cell Res 2007;20:27-35.
16. Scherschun L, Kim JJ, Lim HW. Narrow-band ultraviolet B is a useful and well-tolerated treatment for vitiligo. J Am Acad Dermatol 2001;44:999-1003.
17. Kanwar AJ, Dogra S, Prasad D, Kumar B. Narrow-band UVB for the treatment of vitiligo: An emerging effective and well-tolerated therapy. Int J Dermatol 2005;44:57-60.
18. Yones SS, Palmer RA, Garibaldinos TM, Hawk JLM. Randomized Double-blind trial of Treatment of Vitiligo: Efficacy of psoralen-UVA therapy vs narrowband-UV-B therapy. Arch Dermatol 2007;143:578-83.
19. El Mofty M, Mostafa W, Esmat S, Youssef R, Azzam O, Hunter N, et al . Narrow band Ultraviolet B 311nm in the treatment of vitiligo: Two right-left comparison studies. Photodermatol Photoimmunol Photomed 2006;22:6-11.
20. Westerhof W, Nieuweboer-Krobotova L. Treatment of vitiligo with UV-B radiation vs. psoralen plus UV-A. Arch Dermatol 1997;133:1525-8.
21. Njoo MD, Bos JD, Westerhof W. Treatment of generalized vitiligo in children with narrow-band (TL-01) UVB radiation therapy. J Am Acad Dermatol 2000;42:245-53.
22. Dogra S, Prasad D. Combination of narrow band UVB and topical calcipotriene in vitiligo. Arch Dermatol 2003;139:393.
23. Kanwar AJ, Dogra S. Narrow-band UVB for the treatment of generalized vitiligo in children. Clin Exp Dermatol 2005;30:332-6.
24. Anbar TS, Westerhof W, Rahman AT, Khayyat MA. Evaluation of the effects of NB-UVB in both segmental and non-segmental vitiligo affecting different body sites. Photodermatol Photoimmunol Photomed 2006;22:157.
25. Gambichler T, Breuckmann F, Boms S, Altmeyer P, Kreuter A. Narrowband UVB phototherapy in skin conditions beyond psoriasis. J Am Acad Dermatol 2005;52:660-70.
26. Hercogova J, Buggiani G, Prignano F, Lotti T. A rational approach to the treatment of vitiligo and other hypomelanoses: Pigmentary disorders. Dermatol Clin 2007;25:383-92.
27. Kist JM, Van Voorhees AS. Narrowband ultraviolet B therapy for psoriasis and other skin disorders. Adv Dermatol 2005;21:244-5.

International Journal of Research in Science and Technology
Volume 6, Issue 1 : January - March, 2019
ISSN 2394 - 9954

BOOLEAN LOGIC NETWORKS FOR BIOSENSING DEVICES

P. D. Gaikwad
Department of Physics, Sunderrao Solanke Mahavidyalaya Majalgaon, Beed

ABSTRACT
The PANI-HCl matrix is synthesized electrochemically by potentiostatic method on platinum plate. The synthesized matrix was characterized by using electrochemical technique. The enzyme glucose oxidase (GODx) was immobilized by cross-linking via glutaraldehyde on the PANI-HCl matrix. The characterization of resulting amperometric biosensor for the estimation of glucose has been determined. The stability and life time of the PANI-HCl -GODx electrode have been studied. In the present work biochemical signal through Boolean logic networks composed of bio molecular reactions can lead to high-fidelity biosensing single sensing devices.

Keywords: Polyaniline, glucose oxidase, cross-linking, Boolean logic Network.

INTRODUCTION
The synthesis and characterization of electro active polymers have become two of the most important areas of research in polymer and materials science [1].Amongst conducting polymers, polyaniline (PANI) receives greater attention as a conducting organic material due to its good environmental stability [2-3]. Polyaniline has many advantages, which include simplicity and rapidity of preparation by electrochemical methods and the ability to be formed in aqueous electrolytic solutions [4]. PANI is recognized to be an air-stable organic conducting polymer with interesting electrochemical properties which make it suitable for number of practical applications, such as in biosensors] and electronic devices . [5-8], The determination of glucose is one of the most popular and well-known biosensor applications. In particular, glucose is of special importance because of its involvement in human metabolic process [9].Amperometric biosensor measures the current on an indicator electrode due to direct oxidation of the products of the biochemical reaction. The amperometric biosensors are reliable, relatively cheap and highly sensitive for clinical, industrial and environment purposes [10-11].

Enzymatic logic gates allowed information processing mimicking various Boolean logic operations: AND, OR, XOR, NAND, NOR, etc. [12-13], the system consisted of AND/OR logic gates based on the concerted operation of, glucose oxidase, [14]. AND/OR, as progress in networking these gates and coupling of the resulting system to responsive electrode for output readout, have opened new biosensing opportunities.

Synthesis of PANI-HCl Matrix: The electro polymerization of aniline was carried out by potentiostatic technique, in one compartment electrochemical cell. The PANI-HCl Matrix was synthesized from an aqueous solution of distilled water containing 0.2 M aniline and 1 M of Hydrochloric acid (HCl) . After synthesis, polymer coated electrodes were rinsed thoroughly in distilled water and dried in cold air and then used for subsequent characterization.

Immobilization of GODx on PANI- HCl matr ix: The stock solution of GODx (1 mg/ml) prepared in 0.1 M phosphate buffer was adsorbed onto the surface of PANI-HCl matrix. The enzyme GOD (SISCO) was immobilized by cross-linking via glutaraldehyde (Loba Chemie) on PANI-HCl matrix. This kind of immobilization results in greater physical and chemical stability of the catalytic material due to the cross-linking of enzyme. In this case, the active site of the enzyme could be more accessible for the enzyme reaction.

RESULT AND DISCUSSION
Amperometric studies of PANI-HCl Matrix: The chronoamperogram of synthesized PANI-HCl matrix is shown in Fig. 1.

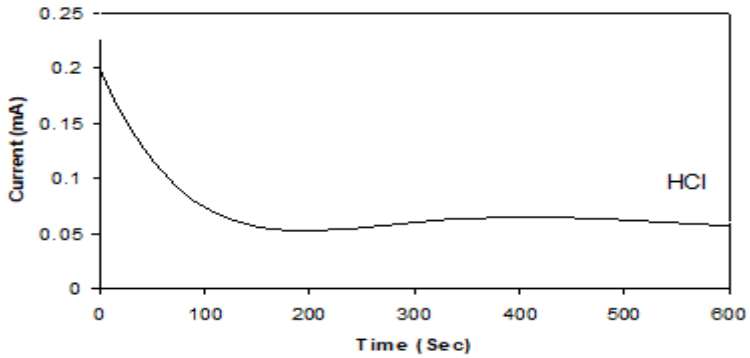

Fig-1: Chronoamperogram of PANI-HCl Matrix .

ISSN 2394 - 9954

Figure.1 has resulted in conducting PANI-HCl matrix with uniform and porous surface morphology. The behavior of the amperometric synthesis overshoot during first few second probably indicates difficult formation of dimmers and oligomers. After this, current remain constant suggesting that building up of the matrix proceeds according to the same reaction along the full thickness of the polymer.

Current response of PANI-HCl-GODx electrodes: The GODx was immobilized on electrochemically synthesized PANI-HCl matrix by cross-linking via glutaraldehyde. The current -time relationship of PANI-HCl-GODx electrode when the applied current set at 0.6 mV in phosphate as shown in Fig.2 .

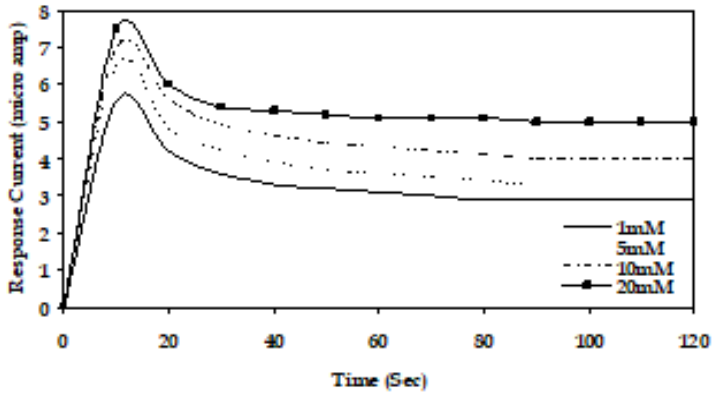

Fig-2: Current-time curves for the PANI-HCl-GODx electrode for various glucose concentrations in 0.1M phosphate buffer with pH 5.

The apparent Michaelis-Menten constant *(K_m)* was calculated for the immobilized enzyme by amperometric method . The values of response current (I_{max}) and K_m for phosphate buffer are 7.5μA and 5.3 mM respectively. Table 1. The value of the K_m depends on the immobilization of enzyme lesser K_m gives faster response to glucose .

Table-1: The analytical performance of PANI-HCl-GODx electrode for sphate at pH 5.

arameters	Phosphate Buffer
*I*max (μA)	7.5
Km (mM)	5.3
Linearity (mM)	0-2
Sensitivity(μA/mM)	1.1
Lifetime(days)	25

Stability of the PANI-HCl-GODx electrodes: It was found that the PANI-HCl-GODx electrode exhibited excellent stability for 25 days in phosphate buffer. The amount of glucose can be determined by measuring the Current of oxidation of hydrogen peroxide, produced in the reaction given below

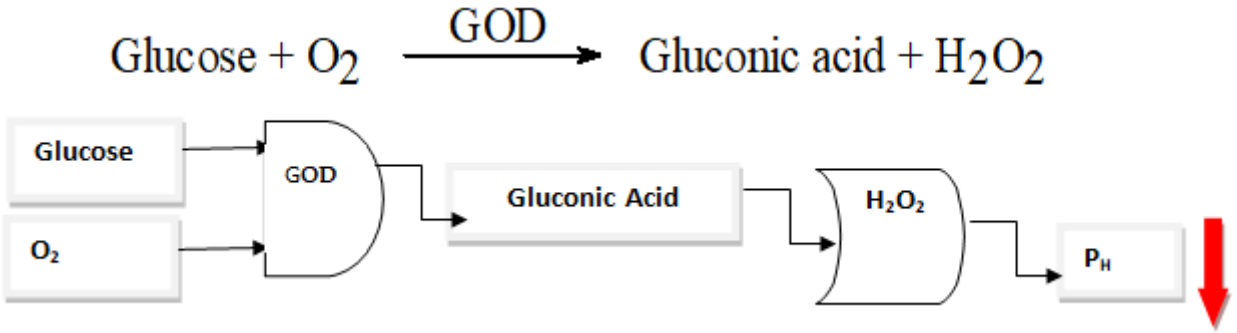

Fig-3: Enzymatic Boolean AND/OR logic gate

CONCLUSIONS

The PANI-HCl-GODx Matrix have been successfully synthesized and by crosslinking via glutaraldehyde has been successfully carried out. The sensitivity of PANI-HCl-GODx electrode was found to be higher excellent response in phosphate buffer (5.0 pH) and also excellent stability for 25 days. Biochemical signal applied in Combination of logic process for Biosensing devices.

ACKNOWLEDGEMENTS

Author is thankful to the UGC Pune for the project.

ISSN 2394 - 9954

REFERENCES

1. Kang E T, Neoha K G and Tanh K L, 1998 Prog. Polym. Sci 23 211
2. Lacroin J C and Diaz A F 1988 *J. Electrochem. Soc.* E135 1457
3. Camalet C,J Lacroix C, Aciyach S, Chaneching K, Lacaze P C, 1998 *Synth. Met.* 93 133
4. Roth S and Graupher W 1993 *Synth. Met.* 57 3623
5. Gaikwad P D, Shirale D J, Gade V K, Savale P A, Kakde K P, Kharat H J and Shirsat M D, Bulletin of Material Science Vol 29, No 4, August 2006, 417-420.
6. Gaikwad P D, Shirale D J, Gade V K, Savale P A, Kakde K P, Kharat H J and Shirsat M D Transaction of The SAEST 41 (2006) 52-56.
7. Bartlett P N and Birkin P R 1993 *Anal. Chem.* 65 1118
8. Yuh-Ming Uang , Tse-Chuan Chou 2003 Biosensors and Bioelectronics 19 141
9. Diaz A F and Logan J A, *J Electroanal. Chem.* 111 (1980) 111.
10. Akundy G S, Rajagopalan R and Iroh J O, *J Applied Polymer Science* 83 (2002) 1970.
11. Fabiano S, Tran-Minch C, Piro B, Dang L A, Pharm M C and Vittori O. *Mat. Sci. Eng.* 21 (2002) 61.
12. Strack, G.; Pita, M.; Ornatska, M.; Katz, E. Boolean logic gates using enzymes as input signals, *ChemBioChem* 2008, *9*, 1260-1266.
13. Baron, R.; Lioubashevski, O.; Katz, E.; Niazov, T.; Willner, I. Logic gates and elementary computing by enzymes, *J. Phys. Chem. A* 2006, *110*, 8548-8553.
14. Pita, M.; Zhou, J.; Manesh, K.M.; Halámek, J.; Katz, E.; Wang, J. Enzyme logic gates for assessing physiological conditions during an injury: Towards digital sensors and actuators, *Sens. Actuat. B* 2009, *139*, 631-636

MANUSCRIPT SUBMISSION

GUIDELINES FOR CONTRIBUTORS

1. Manuscripts should be submitted preferably through email and the research article / paper should preferably not exceed 8 – 10 pages in all.
2. Book review must contain the name of the author and the book reviewed, the place of publication and publisher, date of publication, number of pages and price.
3. Manuscripts should be typed in 12 font-size, Times New Roman, single spaced with 1" margin on a standard A4 size paper. Manuscripts should be organized in the following order: title, name(s) of author(s) and his/her (their) complete affiliation(s) including zip code(s), Abstract (not exceeding 350 words), Introduction, Main body of paper, Conclusion and References.
4. The title of the paper should be in capital letters, bold, size 16" and centered at the top of the first page. The author(s) and affiliations(s) should be centered, bold, size 14" and single-spaced, beginning from the second line below the title.

First Author Name1, Second Author Name2, Third Author Name3

1Author Designation, Department, Organization, City, email id

2Author Designation, Department, Organization, City, email id

3Author Designation, Department, Organization, City, email id

5. The abstract should summarize the context, content and conclusions of the paper in less than 350 words in 12 points italic Times New Roman. The abstract should have about five key words in alphabetical order separated by comma of 12 points italic Times New Roman.
6. Figures and tables should be centered, separately numbered, self explained. Please note that table titles must be above the table and sources of data should be mentioned below the table. The authors should ensure that tables and figures are referred to from the main text.

EXAMPLES OF REFERENCES

All references must be arranged first alphabetically and then it may be further sorted chronologically also.

- **Single author journal article:**

Fox, S. (1984). Empowerment as a catalyst for change: an example for the food industry. *Supply Chain Management*, *2*(3), 29–33.

Bateson, C. D.,(2006), 'Doing Business after the Fall: The Virtue of Moral Hypocrisy', Journal of Business Ethics, 66: 321 – 335

- **Multiple author journal article:**

Khan, M. R., Islam, A. F. M. M., & Das, D. (1886). A Factor Analytic Study on the Validity of a Union Commitment Scale. *Journal of Applied Psychology*, *12*(1), 129-136.

Liu, W.B, Wongcha A, & Peng, K.C. (2012), "Adopting Super-Efficiency And Tobit Model On Analyzing the Efficiency of Teacher's Colleges In Thailand", International Journal on New Trends In Education and Their Implications, Vol.3.3, 108 – 114.

- **Text Book:**

Simchi-Levi, D., Kaminsky, P., & Simchi-Levi, E. (2007). *Designing and Managing the Supply Chain: Concepts, Strategies and Case Studies* (3rd ed.). New York: McGraw-Hill.

S. Neelamegham," Marketing in India, Cases and Reading, Vikas Publishing House Pvt. Ltd, III Edition, 2000.

- **Edited book having one editor:**

Raine, A. (Ed.). (2006). *Crime and schizophrenia: Causes and cures.* New York: Nova Science.

- **Edited book having more than one editor:**

Greenspan, E. L., & Rosenberg, M. (Eds.). (2009). *Martin's annual criminal code:Student edition 2010.* Aurora, ON: Canada Law Book.

- **Chapter in edited book having one editor:**

Bessley, M., & Wilson, P. (1984). Public policy and small firms in Britain. In Levicki, C. (Ed.), *Small Business Theory and Policy* (pp. 111–126). London: Croom Helm.

- **Chapter in edited book having more than one editor:**

Young, M. E., & Wasserman, E. A. (2005). Theories of learning. In K. Lamberts, & R. L. Goldstone (Eds.), *Handbook of cognition* (pp. 161-182). Thousand Oaks, CA: Sage.

- **Electronic sources should include the URL of the website at which they may be found, as shown:**

Sillick, T. J., & Schutte, N. S. (2006). Emotional intelligence and self-esteem mediate between perceived early parental love and adult happiness. *E-Journal of Applied Psychology, 2*(2), 38-48. Retrieved from http://ojs.lib.swin.edu.au/index.php/ejap

- **Unpublished dissertation/ paper:**

Uddin, K. (2000). A Study of Corporate Governance in a Developing Country: A Case of Bangladesh (Unpublished Dissertation). Lingnan University, Hong Kong.

- **Article in newspaper:**

Yunus, M. (2005, March 23). Micro Credit and Poverty Alleviation in Bangladesh. *The Bangladesh Observer*, p. 9.

- **Article in magazine:**

Holloway, M. (2005, August 6). When extinct isn't. *Scientific American, 293*, 22-23.

- **Website of any institution:**

Central Bank of India (2005). *Income Recognition Norms Definition of NPA.* Retrieved August 10, 2005, from http://www.centralbankofindia.co.in/ home/index1.htm, viewed on

7. The submission implies that the work has not been published earlier elsewhere and is not under consideration to be published anywhere else if selected for publication in the journal of Indian Academicians and Researchers Association.

8. Decision of the Editorial Board regarding selection/rejection of the articles will be final.